Towards effective emission regulations:

A numerical and experimental study on flow measurement uncertainty in stacks

Alouette van Hove

Towards effective emission regulations:

A numerical and experimental study on flow measurement uncertainty in stacks

by

Alouette van Hove

to obtain the degree of Master of Science
at the Delft University of Technology,
to be defended publicly on Thursday July 12, 2018 at 10:00 AM.

Student number:	4429265	
Project duration:	September 1, 2017 – July 12, 2018	
Thesis committee:	Dr. R. P. Dwight,	TU Delft, supervisor
	G. J. P. Kok,	VSL, supervisor
	Dr. S. J. Hulshoff,	TU Delft
	Dr. D. Ragni,	TU Delft

TU Delft

Acknowledgements

Foremost, I want to express my gratitude to my thesis supervisors Richard Dwight and Gertjan Kok for their guidance during this research. Their support, ideas and feedback helped me enormously. Furthermore, I want to thank all other partners in the IMPRESS 2 project for their interest and input in my study. It was a pleasure to meet you!

It was a great experience to work on my thesis at VSL. I want to thank all colleagues for the good company and support, coffee breaks, and lunch-time walks. Special mention to Menne Schakel, Peter Lucas, Tim Paans, Silvester Wulffers, Sanne Hagendoorn, Oscar Brandt, and Gerard Nieuwenkamp. I very much enjoyed working with you and I want to thank you for your help with my research.

Next, I want to express my gratitude to the many LES experts who I turned to for advise and who have helped me immensely: Bendiks Jan Boersma, Mathieu Pourquie, Niels Gjøl Jacobsen, and Stefan Hickel. Then there are a number of people who have helped me with things ranging from ideas on mesh generation to providing experimental data: Zeno Belligoli, John Dreese, Stanislav Knotek, Mark Hindle, and Jaap den Toonder. Thank you!

I want to express my gratitude to my parents and brother for their support during my studies in Delft. I am also thankful to my friends for their encouragement, and even more so to Eddy for his feedback. Last, but definitely not least, I want to thank Michał for his support throughout my studies, especially during the final year.

Alouette van Hove
Delft, June 27, 2018

Abstract

Accurate measurement of emissions (i.e. volume flow rate multiplied by concentration) is vital to the control and reduction of air pollution. We quantify the uncertainty of flow measurements by S-type pitot tubes in narrow exhaust stacks (diameter $\leq 0.5\,\mathrm{m}$) in support of recent European Union (EU) regulations for emissions from medium-size combustion plants. The contribution of blockage and wall effects to the uncertainty budget is evaluated. The aim of this thesis is to characterize flow uncertainty and to aid the development of more accurate measurement methods for volume flow rates in narrow exhaust stacks. This thesis will provide the scientific basis for implementation of EU regulations concerning emissions from medium-size combustion plants.

Characterization of flow fields in narrow exhaust stacks is key to accurate volume flow rate measurements. We use numerical simulations to study the mean velocity profile and turbulence statistics of fully developed turbulent flow. To investigate the impact of wall effects on measurement uncertainty, we simulate the flow field around an S-type pitot tube in close proximity to the stack wall. In addition, we conduct S-type pitot tube measurements at various wall-distances and bulk velocities. Throughout this thesis, we use several uncertainty quantification techniques to evaluate the uncertainty of numerical simulations and experiments.

Studying spatial variation in measurement uncertainty gives insight in the most suitable locations for S-type pitot tube measurements in narrow exhaust stacks. The results of this thesis suggest that wall effects dominate over other sources of measurement uncertainty in the near wall region. Throughout the measurement plane, the combined uncertainty of measurement error sources exceed the impact of blockage. We recommend to determine volume flow rates in narrow exhaust stacks by S-type pitot tube measurements in the stack center. A correction factor can be determined to compute the volume flow rate in a narrow exhaust stack from the maximum flow rate in the stack center.

Contents

List of Figures

List of Tables

Glossary

code verification process of determining that the code accurately solves the mathematical model incorporated in the code

combined standard uncertainty ($\mathbb{u}_\mathrm{c}$) standard uncertainty of the result of a measurement or simulation when that result is obtained from the values of a number of other quantities

comparison error (E) difference between a simulated parameter and measured parameter

coverage factor (k) numerical factor used as a multiplier of the (combined) standard uncertainty to obtain an expanded uncertainty

data (D) Experimental parameter

error (δ) difference between a measured quantity or simulated quantity and its true value

measurand parameter to be measured

solution (S) Simulation parameter

solution verification process of estimating the numerical uncertainty of a particular calculation

standard uncertainty ($\mathbb{u}$) uncertainty of the result of a measurement or simulation expressed as a standard deviation

uncertainty parameter, associated with the result of a measurement or simulation, that characterizes the dispersion of the values that could reasonably be attributed to the measurand or simulation quantity. See standard uncertainty and expanded uncertainty

validation process of determining the degree to which a which a model is an accurate representation of the real world from the perspective of the intended uses of the simulation

verification see code verification and solution verification

Nomenclature

Acronyms

AIAA	American Institute of Aeronautics and Astronautics
ASCE	American Society of Civil Engineers
ASME	American Society of Mechanical Engineers
CEN	European Committee for Standardization
CFD	Computational Fluid Dynamics
CFL	Courant-Friedrichs-Lewy number
DNS	Direct Numerical Simulation
EN	European Standard
ERCOFTAC	European Research Community on Flow, Turbulence and Combustion
EU	European Union
GCI	Grid Convergence Index
GUM	Guide to the Expression of Uncertainty in Measurement
ISO	International Organization of Standardization
ITTC	International Towing Tank Conference
LES	Large Eddy Simulation
MWth	MegaWatt thermal
PDF	Probability Density Function
RANS	Reynolds-Averaged Navier Stokes
SRM	Standard Reference Method
UQ	Uncertainty Quantification
US EPA	United States Environmental Protection Agency
VSL	Van Swinden Laboratory
V&V	Verification and Validation
WAF	Wall Adjustment Factor
WALE	Wall Adaptive Local Eddy viscosity
WHO	World Health Organization

Subscripts/supercripts

$(\ )_{\mathrm{atm}}$	atmospheric
$(\ )_{\mathrm{cyl}}$	cylinder
$(\ )_{\mathrm{D}}$	experimental data
$(\ )_{\mathrm{discr}}$	discretization
$(\ )_{\mathrm{input}}$	input parameter
$(\ )_{\mathrm{iter}}$	iterative
$(\ )_{\mathrm{max}}$	maximum
$(\ )_{\mathrm{min}}$	minimum
$(\ )_{\mathrm{model}}$	simulation model
$(\ )_{\mathrm{num}}$	numerical
$(\ )_{\mathrm{pitot}}$	S-type pitot tube
$(\ )_{\mathrm{RE}}$	Richardson Extrapolation
$(\ )_{\mathrm{ref}}$	reference
$(\ )_{\mathrm{r.m.s.}}$	root mean square
$(\ )_{\mathrm{round-off}}$	round-off
$(\ )_{\mathrm{S}}$	solution of simulation
$(\ )_{\mathrm{sgs}}$	subgrid-scale
$(\ )_{\mathrm{total}}$	total
$(\ )_{\mathrm{val}}$	validation
$(\ )^{\mathrm{w}}$	weighted version
$(\ )^{*}$	under standard laboratory conditions
$(\ )^{+}$	non-dimensional

Latin symbols

A	Area	[m^2]
a	Spectral mode strength of input parameter	[$-$]
b	Spectral mode strength of output parameter	[$-$]
C_s	Smagorinsky constant	[$-$]
C_w	WALE constant	[$-$]
c	Concentration	[$\mathrm{kg\,m^{-3}}$]
c_i	Sensitivity coefficient	[case dependent]
D	Experimental parameter (data)	[case dependent]
D	Inner diameter	[m]
D_{h}	Hydraulic diameter	[m]
d	Experimental output estimate	[case dependent]

d_p	Outer diameter of pitot tube orifices	[m]
$E(\kappa)$	Energy spectrum of turbulent kinetic energy (per unit mass)	$[\mathrm{m}^3\,\mathrm{s}^{-2}]$
e	Turbulent kinetic energy (per unit mass)	$[\mathrm{m}^\mathrm{s}\,\mathrm{s}^{-2}]$
$\mathcal{F}$	Model	[–]
F	Correction factor	[–]
F_s	Safety factor	[–]
f	Friction factor	[–]
$G(\boldsymbol{\gamma} - \boldsymbol{x})$	Filter function	[–]
g	Gravitational acceleration	$[\mathrm{m}\,\mathrm{s}^{-2}]$
$[g_{ij}]$	Velocity gradient	$[\mathrm{s}^{-1}]$
h	Representative cell size	[m]
K	Calibration coefficient	[–]
k	Coverage factor	[–]
$\mathcal{L}$	Mixing length	[m]
L	Length	[m]
M	Molar mass	$[\mathrm{kg}\,\mathrm{mol}^{-1}]$
$\dot{m}$	Mass flow rate	$[\mathrm{kg}\,\mathrm{s}^{-1}]$
P	Order of multi-dimensional polynomial basis	[–]
P	Perimeter	[m]
p	Observed order of convergence	[–]
p	Order of one-dimensional polynomial basis	[–]
p	Pressure	[Pa]
$\mathcal{Q}$	Q-criterion: second invariant of the velocity gradient tensor	$[\mathrm{s}^{-2}]$
Q	Volume flow rate	$[\mathrm{m}^3\,\mathrm{s}^{-1}]$
R	Radius	[m]
R	Universal gas constant	$[\mathrm{kg}\,\mathrm{m}^2\,\mathrm{s}^{-2}\,\mathrm{K}^{-1}\,\mathrm{mol}^{-1}]$
R_{ij}	Correlation tensor	$[\mathrm{m}^2\,\mathrm{s}^{-2}]$
Re_D	Reynolds number based on diameter	[–]
Re_τ	Reynolds number based on wall friction velocity	[–]
$\mathcal{S}_{ij}^d$	Traceless symmetric part of the square of the velocity gradient tensor	$[\mathrm{s}^{-2}]$
$[\mathbf{S}_{ij}]$	Filtered strain rate tensor	$[\mathrm{s}^{-1}]$
S	Simulation parameter (solution)	[case dependent]
s	Simulation output estimate	[case dependent]
T	Period	[s]
T	Temperature	[K]
T	True value	[case dependent]

t	Time	[s]
$\mathbb{U}$	Expanded uncertainty	[case dependent]
$\mathbb{u}$	Standard uncertainty	[case dependent]
$\mathbb{u}_{\mathrm{c}}$	Combined standard uncertainty	[case dependent]
u	Velocity	[$\mathrm{m\,s^{-1}}$]
$\overline{u}_{\mathrm{bulk}}$	Bulk velocity	[$\mathrm{m\,s^{-1}}$]
u_{τ}	Wall friction velocity	[$\mathrm{m\,s^{-1}}$]
V	Volume	[$\mathrm{m^3}$]
WAF	Wall Adjustment Factor	[$-$]
w	Weight factor	[$-$]
$\boldsymbol{X}$	Vector of uncertain input parameters	[case dependent]
X_i	Uncertain input parameter	[case dependent]
x_i	Input estimate	[case dependent]
Y	Uncertain output parameter	[case dependent]
y	Distance from stack wall	[m]
y	Output estimate	[case dependent]

Greek symbols

α	Swirl angle	[°]
β	Yaw angle	[°]
γ	Non-dimensional velocity gradient	[$-$]
Δ	Characteristic grid size	[m]
Δ_f	Filter length	[m]
Δp	Differential pressure	[Pa]
δ	Error	[case dependent]
δ_{ij}	Kronecker delta	[$-$]
ϵ	MacMillan constant	[$-$]
κ	Von Kármán constant	[$-$]
κ	Wavenumber	[$\mathrm{m^{-1}}$]
μ	Dynamic viscosity	[$\mathrm{kg\,m^{-1}\,s^{-1}}$]
ν	Kinematic viscosity	[$\mathrm{m^2\,s^{-1}}$]
$\boldsymbol{\xi}$	Multi-dimensional vector of random parameters	[case dependent]
ξ	One-dimensional random parameter	[case dependent]
ρ	Density	[$\mathrm{kg\,m^{-3}}$]
σ	Standard deviation	[case dependent]
τ	Shear stress	[Pa]

τ_{ij}	Subgrid stress	[Pa]
τ_{wall}	Wall shear stress	[Pa]
φ	Key variable of interest	[case dependent]
Ψ	Multi-dimensional orthogonal polynomial function	$[-]$
Ω	One-dimensional orthogonal polynomial function	$[-]$

Chapter 1

Introduction

Poor air quality has detrimental effects on ecosystems [41], and human health [9, 53]. Since the 1970s, the European Commission has implemented legislation to reduce emissions of harmful gases in Europe. While significant progress has been made in reducing air pollution in Europe [90, 92], the current concentrations still exceed the World Health Organization (WHO) guideline values [37], and air quality problems persist. Over 400,000 premature deaths and health costs of 330 to 940 billion Euro are attributed to air pollution in the European Union (EU) each year [37]. Moreover, pollution continues to damage vegetation and ecosystems [40].

Further reduction in the emission of pollutants is required to reach the EU long-term objective of "achieving levels of air quality that do not give rise to significant negative impacts on, and risks to human health and the environment" [31]. In 2013, the European Commission established the Clean Air Policy Package for Europe [35]. This package aims at achieving full compliance with existing air quality legislation by 2020 at the latest, and further improving air quality in Europe by 2030 and beyond. To this end, the package sets forth to strengthen the implementation of existing legislation, introduce stricter national emission reduction commitments, and reduce emissions from medium-size combustion plants ($\geq$ 1 MWth and $<$ 50 MWth).

The novel Medium Combustion Plant Directive [38] fills the gap in legislation between the Industrial Emissions Directive [34] covering emission from large-size combustion plants ($\geq$ 50 MWth), and the Ecodesign Directive [33] concerning smaller appliances (heaters and boilers $<$ 1 MWth). Medium-size combustion plants are used for a variety of applications such as electricity generation, residential heating and cooling, and providing steam for industrial processes [36]. The emission limit values set in the directive will have to be applied by 2018 for new plants and by 2025 or 2030 for existing plants, depending on their size. Enforcement of this directive is estimated to deliver 10 to 20 percent of the necessary reduction of emissions to reach the WHO concentration guideline values of pollutants in the atmosphere [36].

Industry and regulators require robust methods to measure mass emissions (i.e. volume flow rate multiplied by concentration). Nonetheless, volume flow in narrow exhaust stacks of medium-size combustion plants has not been characterized and the magnitude of measurement error sources remains unclear. As a result, the uncertainties reported in annual mass emission reports are not reliable and this makes it difficult to enforce legislation. Further research to the impact of error sources in narrow exhaust stacks is required to develop standardized measurement methods to report, and therefore control, mass emissions for medium-size combustion plants.

This thesis provides one of the first flow studies in support of the Medium Combustion Plant Directive [38] in terms of flow uncertainty sources in narrow stacks. We evaluate the contribution of blockage and wall effects to the uncertainty budget of mass emissions. Blockage is the phenomenon of increased volume flow between the measurement device and the walls of the exhaust stack. The smaller the cross-sectional area of the exhaust stack is, compared to the measurement device, the larger the effect of blockage. Whereas blockage is insignificant to measurement uncertainty in exhaust stacks of large-size combustion plants, its contribution to measurement uncertainty may be considerable in narrow stacks of medium-size combustion plants.

Wall effect in flow measurement is the rapid decrease of velocity near the wall of the exhaust stack. This phenomenon has two consequences. First, the volume flow rate in an exhaust stack is determined from a grid of local velocity measurements. The local velocity measurements across a grid may not be dense enough to capture the near wall region properly, resulting in an overestimation of the measured volume flow rate. Second, shear and effects of wall proximity to the measurement device may be sources of error in local velocity measurements. The significance of wall effects is expected to increase in narrow stacks.

Though the influence of blockage and wall effects are relatively small, the impact on annual mass emissions becomes significant. Mass emission values are directly related to financial profits and losses for the plant operator when emissions are traded, for example under the EU Emissions Trading System scheme [32]. Furthermore, plant operators require standardized methods with valid uncertainties to reduce, and preferably remove, the risk of incorrectly reporting exceeding emission limit values. The results of this thesis will aid the development of accurate standardized measurement methods for mass emissions from medium-size combustion plants.

1.1 Standardization

Standardization provides a common method to measure and evaluate mass emissions. Without standardization of measurement methods and associated uncertainties, regulators and policy makers are left making decisions based on data that may not be comparable and where uncertainties are poorly estimated or unknown. International and European documentary standards are produced by the International Organization for Standardization (ISO) and the European Committee for Standardization (CEN), respectively. Standards are passed into, or referred to, in member state legislation and provide mandatory measurement methods for industry. As a consequence, combustion plant operators are required to demonstrate compliance with emission limit values at required uncertainties.

Currently, standard for stationary source emissions EN ISO 16911-1 [49] is used to measure volume flow rates within exhaust stacks. The standard describes measurement methods to determine volume flow rates within an exhaust stack based on local velocity measurements made across a measurement plane. The local velocity measurements should be made from a suitable measurement plane, selected according to the requirements in standard EN 15259 [39]. Standardized flow measurement techniques include differential pressure (pitot tubes), vane anemometers, tracer gas dilution and transit time methods.

In support of the release of standard EN ISO 16911-1 [49] in 2013, European working group CEN/TC 264/WG 23 conducted a number of laboratory and field based measurement campaigns to assess the performance of different measurement methods for flow. A summary report with validation data of vane anemometers, L-type, S-type, and 3D pitot tubes was published in 2011 [13]. Dimopolous et al. [18] discuss the improvements in EN ISO 16911-1 [49] compared to standard for stationary source emissions ISO 10780 [48] released in 1994. Standard ISO 10780 [48] had not been validated and lacked the ability to provide measurements within the required uncertainty bounds.

Typical sources of uncertainty for measurement of volume flow rate include determination of the cross-sectional area of the stack, uncertainty of the measurement device and variation in the flow profile over the cross-section of the exhaust stack [18]. With the establishment of the Medium Combustion Plant Directive [38], the need has arisen to evaluate typical sources of uncertainty of volume flow rate measurements within narrow stacks. Stacks of medium-size combustion plants usually have a diameter of $\leq 0.5\,\mathrm{m}$, and bulk velocity of the gas flow is normally between $2\,\mathrm{m/s}$ and $10\,\mathrm{m/s}$. We investigate typical sources of measurement uncertainty within narrow exhaust stacks such as blockage and wall effects.

This thesis is part of the European project "Metrology for Air Pollutant Emissions" (IMPRESS 2). Several national metrology institutes, universities, and research institutes in Europe collaborate in this project to provide metrology for effective emission regulations. Technical University Delft, as well as Dutch metrology institute Van Swinden Laboratory (VSL), are partners in this project. Project activities include the development of validated methods for the measurement of concentration of pollutants, establish the impact of blockage and wall effects in narrow stacks, investigate the use of multiple measurement devices in stacks, among others. CEN and ISO standards will be produced as direct results of IMPRESS 2.

1.2 Previous research

The emission measurement industry generally uses S-type pitot tubes for velocity measurements within exhaust stacks of combustion plants [102, 65]. Since the 1970s, measurement uncertainty of S-type pitot tubes has been investigated by a number of researchers. Leland et al. [65], as well as Williams and DeJarnette [102], quantified measurement errors due to misalignment, aerodynamic interference, turbulence, and Reynolds number. More recently, Norfleet et al. [75] tested S-type pitot tubes in an experimental setup that allowed non-axial flow, and reported measurement errors up to 26 % in the most extreme swirl conditions. Moreover, Shinder et al. [82] described a new facility for testing pitot tubes at a wide range of orientations and turbulence intensities.

The capabilities of Computational Fluid Dynamics (CFD) to reproduce turbulent flows have increased considerably over the last thirty years. This has given researchers the possibility to examine flow phenomena around pitot tubes numerically. Despite various numerical studies on L-type and averaging pitot tubes [8, 52, 99, 96], only few researchers investigated flow patterns around S-type pitot tubes. Trang et al. [91] and Kang et al. [54] used Detached Eddy Simulation to study the effects of misalignment and Reynolds number on S-type pitot tube measurements.

In addition, CFD has been used in several studies to evaluate the accuracy of local flow measurements to obtain volume flow rates within exhaust stacks. Bryant et al. [10] reported uncertainties of ±1 % to ±9 % in volume flow measurements depending on the number of samples and their method of integration. Kateusz [56] obtained comparable uncertainties of approximately ±2 % to more than ±9 % for volume flow measurements in a rectangular duct. The study concluded that the uncertainty is dependent on the number of samples, as well as the non-uniformity of the flow profile. Geršl et al. [43] showed that in case of a bend prior to the stack, the error of the volume flow rate is dependent on the height of the measurement plane, and reported a maximum uncertainty of ±3 %.

1.3 Outline of thesis

All work on flow measurement and uncertainty to date has been focused on stacks of large-size combustion plants. This thesis is one of the first studies to investigate sources of uncertainty of S-type pitot tube measurements in narrow exhaust stacks. We use numerical modeling and experimental research to investigate flow field characteristics in narrow stacks and the impact of blockage and wall effects on the uncertainty of S-type pitot tube measurements. This thesis will provide a scientific basis for EU regulations concerning mass emissions from medium-size combustion plants.

Research Objective

Quantify the impact of blockage and wall effects on measurement uncertainty of volume flow rates within narrow stacks to aid the development of standard measurement methods for mass emissions from medium-size combustion plants.

We use several methods to quantify the uncertainty of numerical and experimental results in this thesis. Chapter 2 gives a literature review of uncertainty quantification. We define the concepts of error and uncertainty. Furthermore, we explain three approaches for uncertainty propagation: sensitivity methods, Monte Carlo methods, and polynomial chaos methods. Moreover, we discuss validation and verification of numerical models. A detailed literature review of standard measurement practice for determining mass emissions from combustion plants is given in Chapter 3. We focus on sources of measurement error by S-type pitot tubes, and discuss corrections for blockage and wall effects.

In Chapters 4 and 5, we use numerical simulations to study the characteristics of flow fields in narrow stacks. Numerical modelling can give insight into phenomena which describe the magnitude of sources of error. We study the mean velocity profile and turbulence statistics of fully developed turbulent gas flow in narrow stacks in Chapter 4. In addition, we determine numerical uncertainty of the simulation results. In Chapter 5, we simulate the flow field around an S-type pitot tube. Hereby, we focus on flow patterns in the near wall region to investigate the impact of shear and wall proximity effects.

An experimental study of S-type pitot tube measurements in discussed in Chapter 6. The study is conducted in the flow laboratory of VSL. We measure flow velocities at several wall-distances with an S-type pitot tube. We estimate the measurement error, and evaluate corrections for blockage and wall effects. Furthermore, we discuss calibration and experimental uncertainty of the measurement results. Finally, a conclusion to this research and recommendations for the development of new standards for volume flow rate measurement in narrow exhaust stacks are given in Chapter 7.

Chapter 2

Uncertainty Quantification

Uncertainty quantification (UQ) is the science of quantitative characterization of uncertainties in both computational applications and measurements. The main objective of this thesis is quantification of emission measurement uncertainty in narrow stacks of medium-size combustion plants. For this purpose, we perform experiments, and characterize the flow field in narrow stacks by numerical simulations. In this chapter, we discuss methods for uncertainty quantification of numerical simulations and experiments used in our study.

The relevant concepts to uncertainty quantification in this thesis are consistent with the definitions used in the *Standard for Verification and Validation in Computational Fluid Dynamics and Heat Transfer* [4] (ASME V&V 20-2009) of the American Society of Mechanical Engineers (ASME). The metrological terms used for experimental uncertainty analysis in the well-known *ISO Guide to the Expression of Uncertainty in Measurement* [50] (GUM) are thereby extended to apply to simulation uncertainty. The definitions of a number of metrological concepts used in this thesis are given in the Glossary.

2.1 Error and uncertainty

Pertinent definitions to the discussion on uncertainty quantification are the concepts of error and uncertainty:

- *error*: the result of a measurement or simulation minus its true value,
- *uncertainty*: a parameter, associated with the result of a measurement or simulation, that characterizes the dispersion of the values that could reasonably be attributed to the measurand or simulation result [50].

In this context, error δ requires the knowledge of true value T and has a particular magnitude and sign. The error in simulation parameter S is denoted by δ_{S}, and is expressed by

$$\delta_{\mathrm{S}} := S - T. \tag{2.1}$$

Similarly, the error in experimental parameter (data) D is denoted by δ_{D}, and is expressed by

$$\delta_{\mathrm{D}} := D - T. \tag{2.2}$$

In general, a simulation result or experimental result is corrected if the magnitude and sign of its error are known. For an error of unknown magnitude and sign, an uncertainty $\mathbb{u}$ is estimated with the idea that $\pm\mathbb{u}$ characterizes the range containing error δ. The uncertainties corresponding to unknown simulation error δ_{S} and unknown experimental error δ_{D} are denoted by $\mathbb{u}_{\mathrm{S}}$ and $\mathbb{u}_{\mathrm{D}}$, respectively. In experimental uncertainty analysis [50], standard uncertainty $\mathbb{u}_\text{D}$ corresponds to an estimate of the standard deviation σ of the population of experimental data. Error δ_D is a single realization from the distribution. Assuming a Gaussian distribution, the range $\pm\mathbb{u}_\text{D}$ contains error δ_D with a confidence level of 68 %.

The result of a simulation or measurement is an estimate of the output quantity of interest. Expanded uncertainty $\mathbb{U}$ is used to define an interval about simulation output estimate s or experimental output estimate d within which the true value falls with a certain degree of confidence. Coverage factor k is used to convert standard uncertainty $\mathbb{u}$ to expanded uncertainty $\mathbb{U}$ by

$$\mathbb{U} = k\,\mathbb{u}. \tag{2.3}$$

To estimate an interval, an assumption about the probability distribution of the unknown error must be made. Assuming a Gaussian distribution, expanded uncertainty $\mathbb{U}$ with a confidence level of 95 % is computed by $k = 2$, and $k = 3$ defines an expanded uncertainty $\mathbb{U}$ with a confidence level greater than 99 %. As a result, simulation parameter S and experiment parameter D are given by

$$S \in [s \pm \mathbb{U}_\text{S}] \quad \text{and} \quad D \in [d \pm \mathbb{U}_\text{D}]\,. \tag{2.4}$$

Expanded uncertainty $\mathbb{U}$ can be expressed as absolute value or relative value. Relative expanded uncertainties, $\mathbb{U}_\text{S}/s$ and $\mathbb{U}_\text{D}/d$, are usually written as a percentage. Similarly, relative errors, δ_S/s and δ_D/d, can be expressed as a percentage.

2.2 Uncertainty propagation

Uncertainty propagation is the process of analyzing the propagation of uncertainty from model inputs to outputs. We consider the general framework

$$Y = \mathcal{F}\left(\boldsymbol{X}\right), \tag{2.5}$$

where $\mathcal{F}$ represents the model, $\boldsymbol{X} = (X_1, X_2, \ldots, X_n)$ is a vector of n uncertain input parameters, and Y is an uncertain output parameter of interest. An estimate of the quantity of interest, denoted by y, is determined from a vector of n input estimates $\boldsymbol{x} = (x_1, x_2, \ldots, x_n)$, such that

$$y = \mathcal{F}\left(\boldsymbol{x}\right). \tag{2.6}$$

Numerous methods have been developed to determine the uncertainty of output estimate y. In this section, three popular approaches are discussed: sensitivity methods, Monte Carlo methods, and polynomial chaos methods.

2.2.1 Sensitivity methods

We will summarize sensitivity methods in this section, a detailed discussion can be found in the GUM [50]. The standard uncertainty of output estimate y is obtained by combining the standard uncertainties of input estimates $x_1, x_2, \ldots, x_n$. This combined standard uncertainty of output estimate y is denoted by $\mathbb{u}_\text{c}(y)$. The combined standard uncertainty $\mathbb{u}_\text{c}(y)$ is the positive square root of the combined variance

$$\mathbb{u}_\text{c}^2(y) = \sum_{i=1}^{n} \left[c_i \mathbb{u}(x_i)\right]^2, \tag{2.7}$$

where c_i denotes the sensitivity coefficients

$$c_i = \frac{\partial \mathcal{F}}{\partial x_i}. \tag{2.8}$$

The partial derivatives $\partial\mathcal{F}/\partial x_i$ describe how output estimate y varies with changes in the values of input estimates $x_1, x_2, \ldots, x_n$. Likewise, a change in standard uncertainty of input estimate x_i corresponds to a variation in y of $(\partial\mathcal{F}/\partial x_i)\,\mathbb{u}(x_i)$. Combined variance $\mathbb{u}_\mathrm{c}^2(y)$ can therefore be viewed as a sum of terms, each representing the estimated variance of output estimate y generated by the estimated variance of each input estimate x_i. This suggests writing

$$\mathbb{u}_\mathrm{c}^2(y) = \sum_{i=1}^{n} \mathbb{u}_i^2(y), \tag{2.9}$$

where $\mathbb{u}_i(y) \equiv |c_i|\mathbb{u}(x_i)$. The combined variance by (2.7) and (2.9) assumes that all uncertain input parameters are independent. Correlations must be taken into account for cases where two or more uncertain input parameters are related, see the GUM [50] for appropriate expressions of combined variance of correlated uncertain input parameters.

Given model $\mathcal{F}$ is algebraic, sensitivity coefficients $\partial\mathcal{F}/\partial x_i$ may be computed analytically. However, if model $\mathcal{F}$ is numerical, finite difference differentiation is the most practical approach. The procedure is to evaluate the model with input parameters $x_1, x_2, \ldots, x_n$, and to evaluate the model with perturbed values of each of the input parameters. As a result, sensitivity coefficients c_i are estimated by

$$c_i \approx \frac{\mathcal{F}(x_1, \ldots, x_i + \Delta x_i, \ldots, x_n) - \mathcal{F}(x_1, \ldots, x_i, \ldots, x_n)}{\Delta x_i}. \tag{2.10}$$

Approximation (2.10) is first-order, and requires $n+1$ model evaluations.

Choosing an appropriate perturbation size Δx_i is challenging [4]. If the perturbation size is too large, the truncation error of (2.10) will consequently be too large, and if the perturbation size is too small, round-off errors become significant. By using model evaluations in the proximity of output estimate y, sensitivity methods do not capture highly nonlinear behaviour in the parameter space. In contrast, Monte Carlo methods and polynomial chaos methods sample the entire parameter space and are considered more reliable for uncertainty propagation of numerical models.

2.2.2 Monte Carlo methods

Monte Carlo methods typically involve the analysis of a large number of model evaluations with various combinations of model parameters. Monte Carlo methods require probability density functions (PDFs) to represent the uncertain input parameters $X_1, X_2, \ldots, X_n$. A sample set of size k is randomly generated from the distribution of each uncertain input parameter X, such that

$$X = \{X^1, X^2, \ldots, X^k\}, \tag{2.11}$$

where X^k denotes the k^th sample of uncertain input parameter X. To ensure representation of the entire parameter range, large sample sets must be generated. Model (2.5) is evaluated for each sample, such that

$$Y^j = \mathcal{F}(\boldsymbol{X}^j), \tag{2.12}$$

where sample $\boldsymbol{X}^j$ is a vector of model inputs formed by combination of elements from each sample set.

An estimate of the uncertain output parameter of interest, denoted by y, is the arithmetic mean of the population of model outputs

$$y \approx \overline{Y} = \frac{1}{N}\sum_{j=1}^{N} \mathcal{F}\left(\boldsymbol{X}^j\right), \tag{2.13}$$

where N is the total number of model evaluations. The standard uncertainty of output parameter of interest Y is equal to the positive square root of the variance of the population of model outputs

$$\mathbb{u}(y) \approx \sqrt{\sigma^2(y)}, \tag{2.14}$$

where

$$\sigma^2(y) \approx \frac{1}{N-1} \sum_{j=1}^{N} \left(\mathcal{F}\left(\boldsymbol{X}^j\right) - \overline{Y} \right)^2. \tag{2.15}$$

The disadvantage of Monte Carlo methods is the large number of model evaluations required to construct a reasonable estimate of quantity of interest Y. Monte Carlo methods typically exhibit a slow convergence rate of $\mathcal{O}(1/\sqrt{N})$ [85], hence the number of model evaluations must be increased by a factor 100 to gain an additional order of accuracy. Generally, structured sampling techniques exhibit higher convergence rate. An effective structured method is Latin Hypercube sampling, see, for example, Helton and Davis [47]. The range of the PDF of each uncertain input parameter is divided into m disjoint intervals of equal probability, such that each interval has a probability of $100/m$ percent. Sample sets for each uncertainty input parameter X are generated by random element selection from each interval. Using either random or structured sampling, the adequate number of samples $\mathbf{X}^j$ for statistical convergence and sufficiently accurate representations of the distribution of uncertain output parameters remains debatable [4].

2.2.3 Polynomial chaos methods

In this section, we summarize non-intrusive polynomial chaos methods. Polynomial chaos methods are described in detail by Le Maître and Knio [63], and Xiu and Karniadakis [105]. The concept of polynomial chaos methods is to approximate the PDFs of uncertain model parameters with a series expansion of orthogonal polynomials. Each uncertain input parameter of (2.5) can be approximated by

$$X \approx \sum_{i=0}^{p} a_i \Omega_i(\xi), \tag{2.16}$$

where Ω_i are orthogonal polynomial functions of the one-dimensional random parameter ξ, a_i are known spectral mode strengths of the input parameter, i denotes the mode of the polynomial function and p the order of the one-dimensional basis. We choose the type of polynomials according to the PDF of the uncertain input parameters (Table 2.1). For example, for X sampled from a Gaussian PDF, Ω_i are one-dimensional Hermite polynomials

$$\Omega_i(\xi) = \begin{cases} 1 & \text{for } i = 0, \\ \xi & \text{for } i = 1, \\ -1 + \xi^2 & \text{for } i = 2, \\ \dots \end{cases} \tag{2.17}$$

where ξ is a standardized Gaussian random parameter with zero mean and unit variance, i.e. normal distribution: $\mathcal{N}[0,1]$. An expansion of a Gaussian PDF with Hermite polynomials up to order $p = 1$ is exact [55], such that

$$X = a_0 + a_1 \xi, \tag{2.18}$$

where a_0 is the mean, and a_1 is the standard deviation of the PDF.

Table 2.1: Correspondence of the type of orthogonal polynomials and PDF distribution of the uncertain input parameters.

PDF of X	Polynomials $\{\Omega_i(\xi)\}$
Gaussian	Hermite
Uniform	Legendre
Gamma	Laguerre
Beta	Jacobi

Analogous to (2.16), each uncertain output parameter of the model (2.5) can be approximated by an expansion. In general, the uncertain output parameter depends on all uncertain input parameters, yielding the expansion

$$Y \approx \sum_{i=0}^{P} b_i \Psi_i(\boldsymbol{\xi}), \tag{2.19}$$

where b_i are the unknown spectral mode strengths of the output quantity, P is the order of the n-dimensional polynomial basis, and Ψ_i are orthogonal polynomial functions of the n-dimensional vector of random input parameters

$$\boldsymbol{\xi} = (\xi_1, \xi_2, \ldots, \xi_n) \,. \tag{2.20}$$

In general, the type of output distribution is unknown. Hence, a high enough order of polynomials is required to provide reasonable approximations. The number of expansion terms of (2.19) is determined by

$$P + 1 = \frac{(p+n)!}{p! \; n!}. \tag{2.21}$$

Note that the model output is expanded on an n-dimensional basis and will generally depend on all uncertain input parameters. The unknown spectral mode strengths b_i of (2.19) are numerically evaluated by evaluating the model output at a set of collocation points. $P + 1$ samples of the random input parameter $\boldsymbol{\xi}$ are generated according to the sampling strategy of choice. For each sample $\boldsymbol{\xi}^j$, the model output is evaluated, such that

$$Y^j = \mathcal{F}\left(\boldsymbol{X}^j\right). \tag{2.22}$$

Rearranging (2.19) yields a linear system

$$\begin{pmatrix} \Omega_0(\boldsymbol{\xi}^0) & \Omega_1(\boldsymbol{\xi}^0) & \cdots & \Omega_P(\boldsymbol{\xi}^0) \\ \Omega_0(\boldsymbol{\xi}^1) & \Omega_1(\boldsymbol{\xi}^1) & \cdots & \Omega_P(\boldsymbol{\xi}^1) \\ \vdots & \vdots & & \vdots \\ \Omega_0(\boldsymbol{\xi}^P) & \Omega_1(\boldsymbol{\xi}^P) & \cdots & \Omega_P(\boldsymbol{\xi}^P) \end{pmatrix} \begin{pmatrix} b_0 \\ b_1 \\ \vdots \\ b_P \end{pmatrix} = \begin{pmatrix} Y^0 \\ Y^1 \\ \vdots \\ Y^P \end{pmatrix}, \tag{2.23}$$

with $P + 1$ unknown spectral mode strengths $b_0, \ldots, b_P$. The right-hand side vector contains the model outputs from (2.22). After solving (2.23) for the spectral mode strengths, output estimate y and variance $\mathbb{u}^2(y)$ are computed by [57]

$$y = b_0, \tag{2.24}$$

$$\mathbb{u}^2(y) = \sum_{i=1}^{P} b_i^2. \tag{2.25}$$

2.3 Verification and validation

Numerical simulations are simplifications of reality that are based on many different types of approximation. Computational fluid dynamics (CFD) models reduce the complexity of reality through its governing equations which are solved by a finite number of elements, time steps, iterations, digits precision, and so on. Consequently, simulation parameter S may have a high accuracy, or its estimate may be far from true value T. Quality assessment of numerical model $\mathcal{F}$ is commonly denoted as verification and validation.

Roache [78] defines the two concepts as: "*verification* is a purely mathematical exercise that intends to show that we are *solving the equations right*, whereas *validation* is a science/engineering activity that intends to show that we are *solving the right equations*". Verification is concerned with numerical error/uncertainties whereas validation deals with modelling error/uncertainties. Verification is composed of two different activities [4]: code verification and solution verification. Code verification

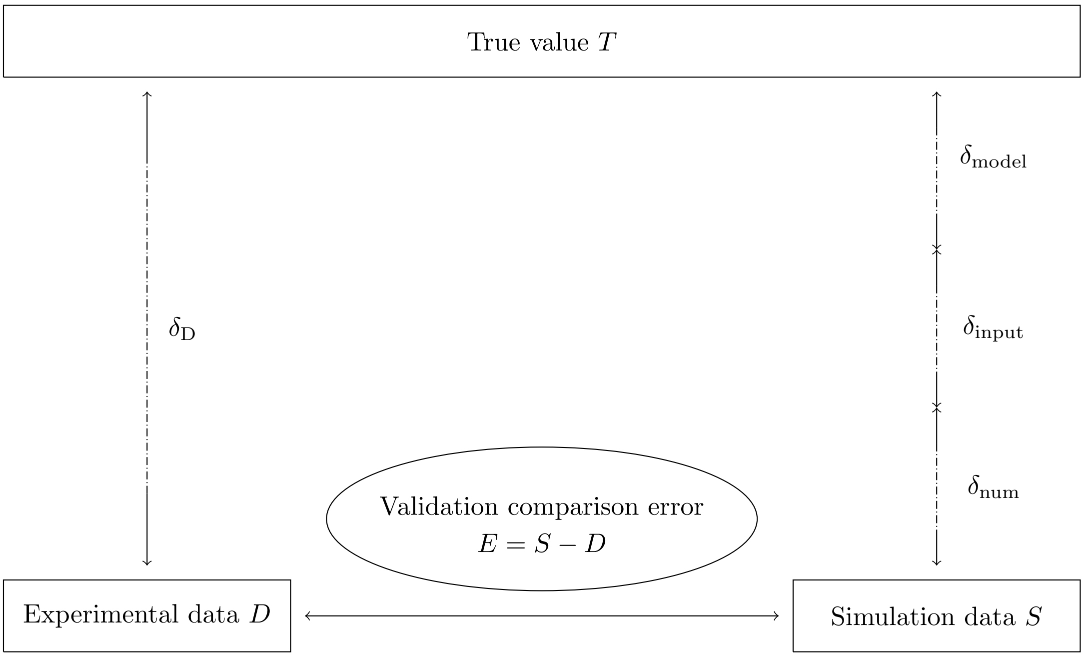

Figure 2.1: Verification and validation process of CFD models. Adapted from ASME V&V 20-2009 [4].

is the process of determining that the CFD code is mathematically correct and involves error evaluation from a known solution. By contrast, solution verification is the process of estimating numerical uncertainty while the exact solution is unknown.

The discussion on how to approach verification and validation of CFD models is ongoing and discussed in several forums, for example, the American Institute of Aeronautics and Astronautics (AIAA) [1], the American Society of Mechanical Engineers (ASME) [4], the European Research Community on Flow, Turbulence and Combustion (ERCOFTAC) [29], the American Society of Civil Engineers (ASCE) [98], and the International Towing Tank Conference (ITTC) [51]. In this thesis, we follow the verification and validation procedures set out in the ASME V&V 20-2009 [4] guide.

In the validation process, simulation parameter S is compared with experimental parameter D for specified variables at a specified set of conditions. *Validation comparison error* E is defined as

$$E \coloneqq S - D. \tag{2.26}$$

Using (2.1) and (2.2), validation comparison error E is equal to the difference between simulation error δ_{S} and experimental error δ_{D}

$$E = (\delta_{\mathrm{S}} + T) - (\delta_{\mathrm{D}} + T) = \delta_S - \delta_D. \tag{2.27}$$

All errors in simulation parameter S can be classified into three categories:

- *model error* (δ_{model}): the simulation error due to modeling assumptions and approximations,
- *numerical error* (δ_{num}): the simulation error due to the numerical solution of the equations,
- *input parameter error* (δ_{input}): the simulation error due to errors in the simulation input parameters.

Therefore, simulation error δ_{S} is equal to the sum of the three contributions, such that

$$\delta_{\mathrm{S}} \coloneqq \delta_{\mathrm{model}} + \delta_{\mathrm{num}} + \delta_{\mathrm{input}}. \tag{2.28}$$

A schematic overview of the sources of error and validation process is shown in Figure 2.1. By combining (2.27) and (2.28), model error δ_{model} can be written as

$$\delta_{\mathrm{model}} = E - (\delta_{\mathrm{num}} + \delta_{\mathrm{input}} - \delta_{\mathrm{D}}). \tag{2.29}$$

After obtaining simulation parameter S and experimental parameter D, the sign and magnitude of validation comparison error E are known. However, the signs and magnitudes of numerical error δ_{num}, input parameter error δ_{input}, and experimental error δ_{D} are unknown. The standard uncertainties corresponding to these errors are denoted by $\mathbb{u}_{\text{num}}$, $\mathbb{u}_{\text{input}}$, and $\mathbb{u}_{\text{D}}$, respectively. Following Coleman and Stern [15], validation standard uncertainty $\mathbb{u}_{\text{val}}$ is defined as an estimate of the standard deviation of the population of the combination of errors $(\delta_{\text{num}} + \delta_{\text{input}} - \delta_{\text{D}})$. Assuming the errors to be independent, validation standard uncertainty $\mathbb{u}_{\text{val}}$ may be obtained from

$$\mathbb{u}_{\text{val}} = \sqrt{\mathbb{u}^2_{\text{num}} + \mathbb{u}^2_{\text{input}} + \mathbb{u}^2_{\text{D}}}. \tag{2.30}$$

Considering (2.29), $[E \pm \mathbb{u}_{\text{val}}]$ characterizes a range containing model error δ_{model}. Assuming a Gaussian distribution, model error δ_{model} falls within the interval

$$\delta_{\text{model}} \in [E \pm \mathbb{U}_{\text{val}}], \tag{2.31}$$

where $\mathbb{U}_{\text{val}} = 2\,\mathbb{u}_{\text{val}}$ at the 95 % confidence level.

2.3.1 Numerical uncertainty

Numerical error δ_{num} of a CFD model has several components. Following Roache [78], and Eça and Hoekstra [20, 22], we distinguish: round-off error $\delta_{\text{round-off}}$, iterative error δ_{iter}, and discretization error δ_{discr}[a]. As a result, numerical error δ_{num} is defined as the sum of the components

$$\delta_{\text{num}} = \delta_{\text{round-off}} + \delta_{\text{iter}} + \delta_{\text{discr}}. \tag{2.32}$$

Numerical error δ_{num} is unknown, hence numerical uncertainty $\mathbb{u}_{\text{num}}$ is estimated.

Round-off error

Round-off error $\delta_{\text{round-off}}$ is the difference between the mathematical exact value and the numerical value stored in the memory of the machine limited by a finite precision. Though this error is normally very small, it can be significantly magnified through successive operations. Generally, the importance of the round-off error increases with grid refinement. Eça and Hoekstra [22] state that for smooth solutions, the round-off error can be kept at negligible levels using 15 digits precision. Furthermore, the use of double-precision is generally sufficient to ensure negligible round-off errors according to the same researchers [23], so that

$$\delta_{\text{num}} \approx \delta_{\text{iter}} + \delta_{\text{discr}}. \tag{2.33}$$

Iterative error

Iterative error δ_{iter} is originated by the non-linearity of the system of partial differential equations solved in CFD. The iteration process seeks to find a series of approximate solutions to the Navier-Stokes equations by starting with an initial guess. The difference between the solution converged to a given convergence criterion and the solution converged to machine precision [97]. Convergence to machine precision, though possible in principle, is usually not achieved in industrial CFD applications due to the complexity of the simulated flow or limited CPU time.

A commonly used rule of thumb is to require at least three orders of magnitude decrease in normalized residuals for each equation solved over the entire computational domain. The ASME V&V 20-2009 [4] framework warns that this insufficient, even for basic accuracy. The suggested approach is to chose convergence criterion such that iterative error δ_{iter} is negligible in comparison to discretization error

---

[a] Other researchers, for example Stern et al. [87] and Wilson et al. [103], also identify an error contribution due to adjustable input parameters to the CFD model. This error is treated separately in this thesis, as well as in the ASME V&V 20-2009 [4] framework, by δ_{input}.

δ_{discr}. This does not necessarily require iteration to converge at machine precision. Assuming a negligible round-off error $\delta_{\text{round-off}}$, the numerical error is estimated by

$$\delta_{\text{num}} \approx \delta_{\text{discr}}. \tag{2.34}$$

Eça and Hoekstra [22] developed and justified an approach for estimation of iterative error δ_{iter} using the Method of Manufactured Solution as exact solution to the simulated problem. The study shows that in case of non-negligible iterative errors, discretization error δ_{discr} increases. Eça and Hoekstra [22] conclude that iteration error δ_{iter} needs to be two to three orders of magnitude smaller than discretization error δ_{discr} to guarantee a negligible influence.

If iterative error δ_{iter} cannot be neglected, its standard uncertainty $\mathbb{u}_{\text{iter}}$ should be added to discretization standard uncertainty $\mathbb{u}_{\text{discr}}$ to compute numerical uncertainty $\mathbb{u}_{\text{num}}$. Stern et al. [87] propose the following expression for the numerical uncertainty

$$\mathbb{u}_{\text{num},\,a} = \sqrt{\mathbb{u}^2_{\text{discr}} + \mathbb{u}^2_{\text{iter}}}, \tag{2.35}$$

which assumes that the two sources of uncertainty are uncorrelated. In contrast, Eça and Hoekstra [22] claim that the two sources of uncertainty are correlated and it is not conservative to use root mean square addition. Rather, the two terms should be added arithmetically

$$\mathbb{u}_{\text{num},\,b} = \mathbb{u}_{\text{discr}} + \mathbb{u}_{\text{iter}}, \tag{2.36}$$

to obtain a reliable estimate of numerical uncertainty $\mathbb{u}_{\text{num}}$. The views of Eça and Hoekstra have been adopted by the ASME V&V 20-2009 [4] framework, and shall be used in this thesis. Furthermore, the guide states that for time-dependent simulations, iterative convergence should be checked at every time-step, and convergence trends should be documented for key variables.

Discretization error

Discretization error δ_{discr} is a consequence of the approximations embodied (finite difference, finite volume, finite element, et cetera) in the transformation of partial differential equations into a system of algebraic equations. Therefore, varying the grid resolution leads to different results, and the magnitude of discretization error δ_{discr} is expected to decrease with grid refinement. Discretization error δ_{discr} is estimated by simulating values of key variables φ with grids of different resolution.

In case the range of grid resolutions is low, grid refinement does not lead to a converging solution but rather to unpredictable jumps in the solution. This range of grid resolutions is called the stochastic range. If the resolution is high enough to capture most of the flow features that affect the solution, further grid refinement leads to an asymptotically converging solution. This range of grid resolutions is called the asymptotic range. Figure 2.2 demonstrates the stochastic and asymptotic range for key variable φ. The tendency of the grid convergence can be either monotonic or oscillatory, and distinguishing the asymptotic range from the stochastic range may be virtually impossible in complex CFD applications [23]. Eça and Hoekstra [21] identify the lack of geometrical similarity of grids as the main contributor to scatter in the data. Other sources are the use of flux limiters, commonly used in the discretization of convective terms, as well as damping functions and switches between turbulence models.

Discretization error δ_{discr} of the solution of an integral or local flow quantity is commonly estimated by Richardson extrapolation (RE). The assumed one-term expansion of discretization error δ_{discr} is

$$\delta_{\text{discr}} \simeq \delta_{\text{RE}} = \varphi_i - \varphi_0 = \alpha h_i^p, \tag{2.37}$$

where φ_0 is an estimate of the exact solution, α is a constant, h_i is the representative cell size, and p is the observed order of convergence. Estimated error δ_{discr} is usually extended by a safety factor F_{s} to obtain the discretization expanded uncertainty $\mathbb{U}_{\text{discr}}$ at the 95 % confidence level

$$\mathbb{U}_{\text{discr}} = F_{\text{s}}\,|\delta_{\text{discr}}|. \tag{2.38}$$

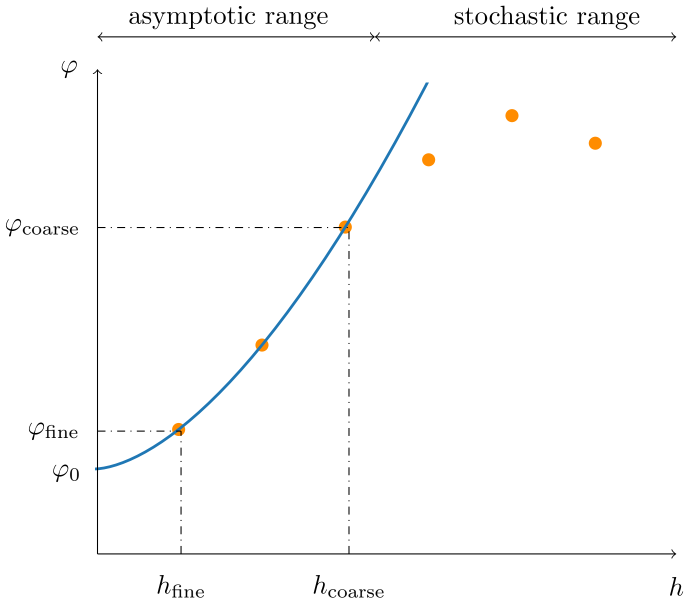

Figure 2.2: Impression of the stochastic range and asymptotic range. Key variable φ as function of representative cell size h. Solid line: fit of the solution in the asymptotic range. Adapted from Viola et al. [97].

The estimated interval containing exact solution φ_0 with 95 % coverage is

$$\varphi_0 \in [\varphi_i \pm \mathbb{U}_{\text{discr}}] \,. \tag{2.39}$$

The following assumptions are inherent to the application of (2.37) [23]:

- The grids must be in the asymptotic range to guarantee that the leading term of the power series expansion is sufficient to estimate the error.
- The grids are geometrically similar so that grid properties like skewness and orthogonality remain unaffected.

These requirements are easy to satisfy for simple problems and a reliable error estimation is feasible. However, for complex problems it is an exception rather than a rule that the conditions for the reliable use of (2.37) are met. The requirement for data in the asymptotic range often means levels of grid refinement beyond those normally used in practical applications [24, 25, 26].

The ASME V&V 20-2009 [4] framework proposes a five-step procedure for estimation of discretization expanded uncertainty $\mathbb{U}_{\text{discr}}$. The Grid Convergence Index (GCI) method is based on research by Roache [78] and assumes a one-term expansion of discretization error δ_{discr} (2.37). The approach requires sets of three grids to obtain order of convergence p. The resulting GCI corresponds to discretization expanded uncertainty $\mathbb{U}_{\text{discr}}$ at 95 % confidence level. The ASME framework stresses that the application of the GCI is often difficult in practical problems because the estimated GCI values are very sensitive to scatter and oscillations in the data. Local values of key variables φ may not exhibit smooth, monotonic dependence on grid resolution, and integral quantities are usually more likely to converge monotonically.

The Least Squares version of the GCI method was pioneered by Eça and Hoekstra [19, 20] and aims to provide a more robust method to use in complex problems. Likewise the original approach, the Least Squares version assumes a one-term expansion of discretization error δ_{discr} (2.37). The method requires a minimum of four grids to predict discretization expanded uncertainty $\mathbb{U}_{\text{discr}}$. The ASME V&V 20-2009 [4] framework states that the Least Squares version of the GCI is currently the most robust and tested method available for the prediction of discretization uncertainty. In the most recent publication [23] on the Least Squares method by Eça and Hoekstra, three other estimators of discretization error δ_{discr} are evaluated when (2.37) fails to provide a reliable estimate.

A step-by-step guide for the application of the original GCI method and the Least Squares version is included in Appendix A.

2.3.2 Input parameter uncertainty

In CFD simulations, output parameter of interest S is determined from n input quantities $X_1, X_2, \ldots, X_n$ through a computational model $\mathcal{F}$

$$S = \mathcal{F}(X_1, X_2, \ldots, X_n). \tag{2.40}$$

Model $\mathcal{F}$ is deterministic, which means that simulation result s is computed precisely from the values of input parameters $x_1, x_2, \ldots, x_n$ without random variations

$$s = \mathcal{F}(x_1, x_2, \ldots, x_n). \tag{2.41}$$

Nevertheless, input parameters $x_1, x_2, \ldots, x_n$ to CFD model $\mathcal{F}$ are usually determined experimentally and have uncertainty associated with them. The uncertainty of the input parameters propagate through model $\mathcal{F}$ to the uncertainty of the output parameter of interest.

Input parameter uncertainty $\mathbb{u}_{\text{input}}$ is the standard uncertainty of simulation parameter S due to uncertainty in simulation input parameters $X_1, X_2, \ldots, X_n$. This is a case of uncertainty propagation. Popular methods to estimate $\mathbb{u}_{\text{input}}$ are discussed in Section 2.2. Sensitivity methods are normally avoided for uncertainty propagation through CFD models since they do not capture nonlinear behaviour of the system. Generally, CFD simulations are computationally expensive, hence a low number of model evaluations is preferred. On one hand, Monte Carlo methods typically require more simulations to reach convergence in comparison to Polynomial Chaos methods. On the other hand, Monte Carlo methods are easier to implement.

When using a coarse grid for input uncertainty analysis, $\mathbb{u}_{\text{input}}$ can be dependent on $\mathbb{u}_{\text{num}}$. If both $\mathbb{u}_{\text{input}}$ and $\mathbb{u}_{\text{num}}$ are comparable in size, the ASME V&V 20-2009 [4] framework recommends to determine $\mathbb{u}_{\text{input}}$ on the finest grid used to estimate $\mathbb{u}_{\text{num}}$. In case $\mathbb{u}_{\text{num}} << \mathbb{u}_{\text{input}}$, the simulations for $\mathbb{u}_{\text{input}}$ may be performed on a coarser grid.

2.3.3 Uncertainty of experimental data

In most experiments, a measurand D is not measured directly, but is determined from n other parameters $X_1, X_2, \ldots, X_n$ through a mathematical model $\mathcal{F}$

$$D = \mathcal{F}(X_1, X_2, \ldots, X_n). \tag{2.42}$$

For example, the emission rate of a combustion plant is determined from measurements of concentration of pollutants, and volume flow rate within the exhaust stack. The latter is again determined from a number of local velocity measurements. In case a pitot tube is used, these measurements are again dependent on calibration, measurements of differential pressure, and density. An estimate of the measurand, denoted by d, is determined from input estimates $x_1, x_2, \ldots, x_n$, such that

$$d = \mathcal{F}(x_1, x_2, \ldots, x_n). \tag{2.43}$$

The uncertainties of input parameters $X_1, X_2, \ldots, X_n$ are propagated through model $\mathcal{F}$ to uncertainty of measurand D. Experimental uncertainty analysis is discussed in several guides, for example, the GUM [50], the European standard *Evaluation of the Uncertainty of Measurement in Calibration* (EA-4/02) [30], and the ASME standard *Test Uncertainty* (PTC 19.1-2005) [3]. In this thesis, we follow the approach of the GUM [50], and common practice at VSL.

The difficulty in evaluation of experimental uncertainty is formulation of mathematical model $\mathcal{F}$. The set of input parameters $X_1, X_2, \ldots, X_n$ may be obtained from

- Single or repeated observations,
- Corrections to instrument readings and corrections for influence quantities,
- Judgment based on experience of the metrologist,
- External sources, such as calibrated measurements standards, certified reference materials, reference data from handbooks, among others.

Furthermore, the input quantities $X_1, X_2, \ldots, X_n$ upon which output parameter D depends may themselves be viewed as measurands and may themselves depend on other quantities, including corrections and correction factors for systematic effects. Altogether, this may lead to a complicated mathematical model $\mathcal{F}$.

In most cases, the best available estimate of an input parameter X is the arithmetic mean of N independent observations

$$x = \overline{X} = \frac{1}{N}\sum_{k=1}^{N} X^k, \tag{2.44}$$

where X^k denotes the k^{th} observed value of input parameter X. For input estimate x, its standard uncertainty $\mathbb{u}(x)$ can be classified into Type A or Type B according to its method of evaluation. Standard uncertainties that are calculated by statistical analysis of a series of observations are classified as Type A. The individual observations of an input parameter X differ in value because of random variations in influence quantities. Standard uncertainty $\mathbb{u}(x)$ is equal to the experimental standard deviation of the mean. In a Type A evaluation, standard uncertainty $\mathbb{u}(x)$ is the positive square root of the variance of the mean

$$\mathbb{u}^2(x) = \sigma^2(\overline{X}) = \frac{\sigma^2(X^k)}{N}, \tag{2.45}$$

where

$$\sigma^2(X^k) = \frac{1}{N-1}\sum_{k=1}^{N}(X^k - \overline{X})^2. \tag{2.46}$$

In a Type B evaluation, standard uncertainty $\mathbb{u}(x)$ is evaluated by scientific judgment based on the available information on the possible dispersion of x. This may include, for example, data provided in calibration certificates, previous measurement data, the metrologist's experience of the behaviour of the instrument, and manufacturer's specifications.

Generally, sensitivity methods, see Section 2.2.1, are used to determine the uncertainty of measurand D. Mathematical model $\mathcal{F}$ is an algebraic model, and sensitivity coefficients c_i can be determined analytically. Combined standard uncertainty $\mathbb{u}_{\mathrm{c}}(d)$ is used to express the uncertainty of an experimental result, such that

$$\mathbb{u}_{\mathrm{D}} = \mathbb{u}_{\mathrm{c}}(d). \tag{2.47}$$

2.4 Final remarks

In this chapter, we defined several concepts in uncertainty quantification, such as error, uncertainty, verification, and validation, among others. Furthermore, we discussed different methods for the propagation of uncertainty through a mathematical model. In this thesis, we use sensitivity methods to estimate the uncertainty of our experimental results. Besides an experimental study, we perform CFD simulations to analyze flow characteristics in narrow stacks. We validate the simulations results against experimental data. Moreover, we determine the numerical uncertainty of our simulation results by applying the Least Squares version of the GCI method. Although first we discuss standardized methods for estimating mass emissions from combustion plants. In the next chapter, we focus on sources of error in mass emission measurement.

Chapter 3

Measurement of Mass Emissions from Combustion Plants

Flue gases are produced when coal, oil, natural gas, wood or any other fuel is combusted in a industrial furnace, power plant's steam-generating boiler, or other combustion device. Flue gases contain a concentration of pollutants such as particulate matter, carbon monoxide, nitrogen oxides and sulfur oxides. A stack is a type of chimney through which flue gases are emitted to the environment. The mass emission rate $\dot{m}$ of pollutants from combustion plants is calculated by multiplying the average concentration of harmful gases c by the volume flow rate Q in the exhaust stack

$$\dot{m} = c\,Q. \tag{3.1}$$

We focus on measurement accuracy of volume flow rate Q in narrow exhaust stacks. Whereas measurement methods for emissions from large-size combustion plants have been developed and standardized, this has not been done for emissions from medium-size combustion plants to date. In Section 3.1, the standard practice for measurement of mass emission from large-size combustion plants is reviewed and its applicability to narrow stacks (diameter $D \leq 0.5\,\mathrm{m}$) of medium-size combustion plants is investigated.

Volume flow rate Q in exhaust stacks is computed by multiplying the bulk velocity $\overline{u}_{\mathrm{bulk}}$ by the cross-sectional area A of the exhaust stack

$$Q = \overline{u}_{\mathrm{bulk}}\,A, \tag{3.2}$$

where bulk velocity $\overline{u}_{\mathrm{bulk}}$ is defined as the mean flow velocity. The most common device used to determine flow velocity in exhaust stacks is the S-type pitot tube [102, 65] shown in Figure 3.1. The large orifices resist plugging in high particle-laden environments of exhaust stacks. Furthermore, the compact design makes the pressure probe suitable for fitting in small diameter sampling ports. The working principle of the S-type pitot tube and its measurement accuracy are discussed in Section 3.2.

3.1 Standard measurement practice

Volume flow rate Q in exhaust stacks of large-size combustion plants is determined according to the Standard Reference Method (SRM) for stationary source emissions EN ISO 16911-1 [49]. This document is written by the International Organization of Standardization (ISO), and provides guidelines and requirements for measurements. By EN ISO 16911-1 [49], the cross-sectional area A of an exhaust stack is divided into a grid of N sections with equal area. Axial velocity $\overline{u}_z$ is measured using a pitot tube or vane anemometer in the center of each section. Subsequently, bulk velocity $\overline{u}_{\mathrm{bulk}}$ is

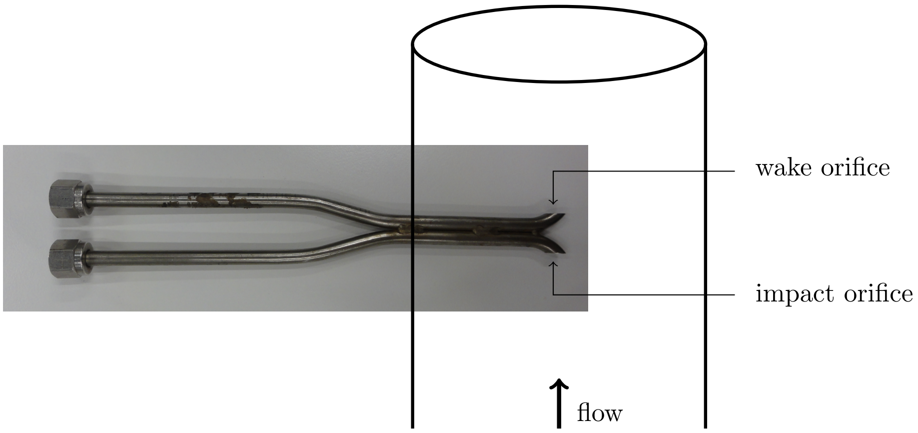

Figure 3.1: S-type pitot tube in an exhaust stack. The impact orifice faces the direction of the flow.

approximated by

$$\overline{u}_{\text{bulk}} \approx \frac{1}{N}\sum_{i=1}^{N} \overline{u}_{\text{z},i}, \tag{3.3}$$

where $\overline{u}_{z,i}$ is the time-averaged local axial velocity obtained by point measurement i.

Sufficient point measurements are necessary to characterize non-uniformities in the flow profile. The minimum number and spacing of measurement points is dependent on the stack size. The procedures in standard EN 15259 [39] are used to determine the number and location of measurement points in rectangular and circular exhaust stacks. We limit our study to circular stacks since they are more common than rectangular stacks. Standard EN 15259 [39] specifies two methods for determining the position of measurement points in circular stacks: the general method and the tangential method, of which the latter is illustrated in Figure 3.2. The sampling points, one at the center of each section, are located on two or more sampling lines. The general method includes a sample point at the center of the sampling plane whereas the tangential method does not. EN ISO 16911-1 [49] favours the tangential method since the central point in the general method does not provide a measure of the average flow, but rather a maximum value assuming a fully developed flow field. The required minimum number of sampling lines and measurement points depending on the diameter and area of the sampling plane (cross-sectional area of the stack) are summarized in Table 3.1.

To illustrate the tangential method, the location of the measurement points for a sampling plane divided into $N = 16$ sections is shown in Figure 3.2. The sampling plane has two sampling lines with each $n = 8$ measurement points. Distance y_i of the sampling points from the stack wall is determined

Table 3.1: Minimum number of sampling lines and points for volume flow rate measurements in circular stacks from standard EN 15259 [39].

Area of sampling plane $A\,[\text{m}^2]$	Diameter of stack $D\,[\text{m}]$	Minimum number sampling lines	Minimum number sampling points per plane
< 0.1	< 0.35	-	1[a]
0.1 to 1.0	0.35 to 1.1	2	4
1.1 to 2.0	$>$ 1.1 to 1.6	2	8
> 2.0	> 1.6	2	$\geq$ 12 and 4 per m^2[b]

---

[a] Using only one sampling point can give rise to errors greater than those specified in standard EN 15259 [39].

[b] For large stacks, 20 sampling points are generally sufficient.

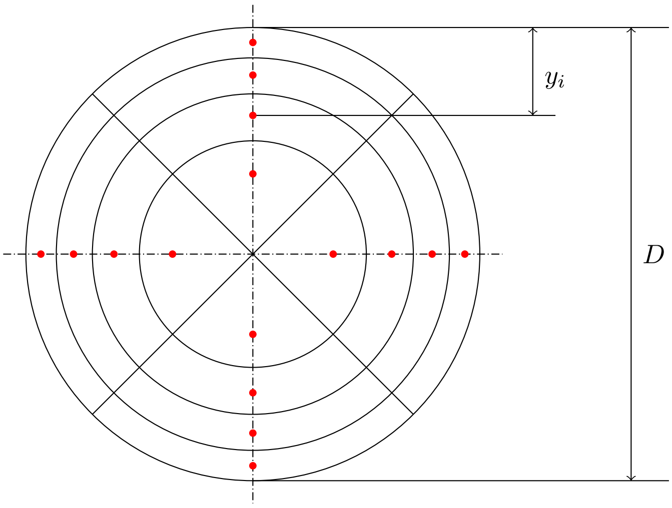

Figure 3.2: Measurement point positions in a sampling plane divided by the tangential method into $N = 16$ sections. The sampling plane has two sampling lines with each $n = 8$ sampling points.

by the tangential equations

$$\begin{aligned} y_i &= \frac{D}{2}\left(1 - \sqrt{1 - \frac{2i-1}{n}}\right) \qquad \text{for } i \leq \frac{n}{2}, \\ y_i &= \frac{D}{2}\left(1 + \sqrt{1 - \frac{2i-1}{n}}\right) \qquad \text{for } i > \frac{n}{2}. \end{aligned} \tag{3.4}$$

Installation effects often found in pipe configurations upstream from the exhaust stack, such as bends, junctions, and fans, cause disturbances in the flow field. Anwar et al. [2] showed that flow disturbances can persist for more than twenty diameters downstream from a bend. Non-homogeneous flow conditions in exhaust stacks may increase the uncertainty of volume flow rate Q as insufficient point measurements of local velocity $\overline{u}_z$ are taken for an accurate representation of the flow field [10, 56, 43]. Standard EN 15259 [39] gives a set of requirements for point measurements to minimize measurement uncertainty:

- Angle of flow is less than 15° with regard to the stack axis. In case this requirement is not met, the measured axial velocity $\overline{u}_z$ should be corrected for swirl following EN ISO 16911-1 [49]. The correction modifies (3.3), such that bulk velocity $\overline{u}_{\text{bulk}}$ is approximated by

  $$\overline{u}_{\text{bulk}} \approx \frac{1}{N}\sum_{i=1}^{N} \cos(\alpha_i)\overline{u}_{z,i}, \tag{3.5}$$

  where α_i denotes the angle of the flow with regard to the stack axis.
- No negative flow.
- A differential pressure larger than 5 Pa for pitot tube measurements. This requirement limits the measurement of velocities below 2 m/s to 3 m/s.
- Ratio of the highest to lowest measured local velocities is less than 3:1.

Furthermore, following standard EN 15259 [39], the sampling plane has to be situated in a section of the exhaust stack where homogeneous flow conditions and concentrations can be expected. These requirements are generally fulfilled when:

- The sampling plane is as far upstream and downstream from any disturbance that could cause a change in flow direction.

- The *hydraulic diameter* D_h of a stack is defined as

$$D_\mathrm{h} \coloneqq \frac{4\,A}{P}, \tag{3.6}$$

  where P is the perimeter of the sampling plane. Hydraulic diameter D_h provides a method for non-circular stacks to be treated as circular for purpose of pressure drop and flow rate calculations. In circular stacks, hydraulic diameter D_h is equal to diameter D. The sampling plane is located in a straight section of the stack with a minimum length of five hydraulic diameters upstream and two hydraulic diameters downstream from the sampling plane. Furthermore, the sampling plane is situated five hydraulic diameters from the top of the stack.

- The sampling plane is in a section of the exhaust stack with constant shape and cross-sectional area.

3.1.1 Blockage and wall effects

This thesis investigates the impact of blockage and wall effects on measurement uncertainty of volume flow rate Q. Both sources of error are considered in the SRM for measuring mass emission from large-size combustion plants. A limitation is set in the form of a maximum percentage of blockage of the measurement plane by the measurement device, and a correction factor is included in the calculation of volume flow rate Q to compensate for wall effects.

As a consequence of continuity, blockage of the flow within an exhaust stack by the measurement device increases the bulk velocity at the sampling plane. Following standard EN ISO 16911-1 [49], the measurement device should obstruct less than 5 % of the sampling plane. Note that this is a relatively large area. For a circular stack of $D = 10\,\mathrm{cm}$, the measurement device may obstruct approximately $15\,\mathrm{cm}^2$. This means that a pitot tube measuring velocity at the stack center may have a frontal width of 3 cm and still comply with requirements.

Wall effects may be cause of error as point velocity measurements across a sampling plane are not dense enough to cover the near wall area properly, resulting in an overestimation of bulk velocity. EN ISO 16911-1 [49] refers to the United States Environmental Protection Agency (US EPA) methods to determine a *Wall Adjustment Factor* (WAF) for volume flow rate Q. The WAF modifies (3.2), such that

$$Q = \mathrm{WAF}\,\overline{u}_\mathrm{bulk}\,A. \tag{3.7}$$

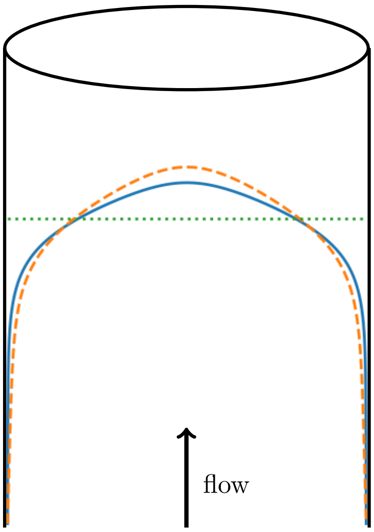

Figure 3.3: Sketch of the mean velocity profile within an exhaust stack. Solid line: smooth stack; dashed line: rough stack; dotted line: bulk velocity $\overline{u}_\mathrm{bulk}$.

A default factor of WAF = 0.990 for brick and mortar stacks and WAF = 0.995 for all other types of stacks is used.

The values of the default factors are based upon results of a study by US EPA [93] whereby an overestimation of bulk velocity of 1.50 % for smooth stacks (steel) and 1.86 % for rough stacks (brick and mortar) was found. Wall roughness influences the velocity profile of the flow field, see Figure 3.3. By sampling at a limited number of points, the computed bulk velocity was larger for rough stacks than for smooth stacks. The researchers computed the percent difference between the average of point velocity measurements following standard measurement practice, and the average velocity based on measurements taken at 2.54 cm increments across a sampling line. The measurement location closest to the wall was at $y = 2.54\,\mathrm{cm}$, and the diameter of the studied stacks ranged from $D = 4.4\,\mathrm{m}$ to $D = 10.4\,\mathrm{m}$.

The WAF may also be determined by performing additional measurements near the wall according to US EPA Method 2H [94]. By this method, the WAF is computed by the quotient of the average velocity of the additional measurements in the near wall region, and the average velocity of the measurements in the near wall region following standard measurement practice. This calculation approach is however only applicable for circular stacks of diameter $D > 1\,\mathrm{m}$.

In addition, shear and proximity of the measurement device to the stack wall may be cause of measurement error. Standard EN 15259 [39] requires that the sampling points are located either more than 3 % of the sampling line length, or more than 5 cm, whichever is the greater value, from the wall of an exhaust stack. Note that this restricts the region of sampling in a narrow stack considerably. For a circular stack of $D = 10\,\mathrm{cm}$, the sampling grid may not include points within 5 cm from the exhaust stack wall, and consequently low velocities in the near wall region are not included in the computation of bulk velocity (3.3).

3.2 Uncertainty of S-type pitot tube measurements

This thesis investigates the uncertainty of measurements of mass emission from combustion plants with the most common used measurement device: the S-type pitot tube shown in Figure 3.1. The working principle of an S-type pitot tube is based on Bernoulli's equation along a streamline in steady, incompressible, inviscid flow

$$p + \frac{1}{2}\rho \overline{u}_z^2 + \rho g z = \text{constant}, \tag{3.8}$$

where ρ is the gas density, p is the pressure, g is the acceleration due to gravity, and z is the elevation of a point above a reference plane in the direction opposite to the gravitational acceleration. Each term in (3.8) has the dimension Pa and can be regarded as a pressure term:

- p is static pressure,
- $\frac{1}{2}\rho \overline{u}_z^2$ is dynamic pressure,
- $\rho g z$ is hydrostatic pressure.

At the sampling point, the hydrostatic pressure is considered to be constant, so that (3.8) is modified to

$$p + \frac{1}{2}\rho \overline{u}_z^2 = p_{\text{total}}, \tag{3.9}$$

where p_{total} is the constant total pressure along a streamline. At the impact orifice of the S-type pitot tube, the flow is brought to rest and total pressure p_{total} is measured. The working principle of the S-type pitot tube relies on the assumption that velocity $\overline{u}_z$ is zero at the wake orifice. Consequently, it is assumed that static pressure p is measured at the wake orifice. The velocity of the flow is computed by

$$\overline{u}_z = K\sqrt{\frac{2\Delta p}{\rho}}, \tag{3.10}$$

where Δp is the differential pressure across the S-type pitot tube, and K is a calibration coefficient. Typical values of calibration coefficient K are 0.85 ± 0.05 [65]. Calibration coefficient K corrects for the differential pressure Δp across the S-type pitot tube not being equal to the difference between total pressure and static pressure: $p_{\text{total}} - p$.

S-type pitot tubes are normally calibrated in the wind tunnel of a national measurement institute or an accredited calibration laboratory. The velocity profile of the wind tunnel is ascertained over a wide range of volume flow rates Q. By applying (3.10), calibration coefficient K is calculated at a known axial velocity $\overline{u}_z$ by measurement of differential pressure Δp across the S-type pitot tube, and gas density ρ.

Gas density ρ is determined by

$$\rho = \frac{p_{\text{atm}} M}{RT}, \tag{3.11}$$

where p_{atm} is the atmospheric pressure, M is the molar mass of the gas or mixture, R is the universal gas constant, and T is the temperature. The temperature is measured using a thermocouple mounted in close proximity to the S-type pitot tube.

The S-type pitot tube is usually installed in exhaust stacks where conditions such as temperature and velocity are different from calibration conditions. Furthermore, the precise positioning of the S-type pitot tube and alignment with flow direction are difficult to observe inside an exhaust stack. These aspects may disturb velocity measurements using calibrated S-type pitot tube coefficients. Since the 1970s, a number of studies have focused on aspects that influence the flow field and pressure distribution around the S-type pitot tube. A variety of factors have been identified by Leland et al. [65] that affect the accuracy of gas velocity measurements by calibrated S-type pitot tubes (referred to as pitot tube in this section):

- **Aerodynamic interference**

  The pitot tube is usually part of a combination probe with a thermocouple and sampling nozzle to determine the concentration of particulate matter in the flow. The proximity of the thermocouple and sampling nozzle may affect the flow field around the pitot tube. Leland et al. [65] found errors of approximately −4 % for measurements with a sampling nozzle attached when the pitot tube was calibrated without nozzle. Williams and DeJarnette [102] reported effects of −3 % to −4 % depending on the distance between the sampling nozzle and the pitot tube.

- **Misalignment**

  An error may occur when the orifices of the pitot tube are not aligned perpendicular to the flow direction. The pitot tube has a *yaw angle* when the instrument is perpendicular to the wall but turned around its axis (Figure 3.4a). The effect of yaw angle misalignment is symmetrical when no sampling nozzle or thermocouple is attached. Williams and DeJarnette [102] found errors up to −12 % for yaw angles of ±20°, whereas some pitot tubes were able to stay within −5 %. A more recent study by Kang et al. [54] observed errors of −2 % for yaw angles of ±10°.

  A pitot tube has a positive *pitch angle* when the impact orifice is turned towards the wall and conversely negative pitch angle when the impact orifice is turned away from the wall (Figure 3.4b). Williams and DeJarnette [102] reported errors up to −12 % at pitch angles of −20° and errors up to 5 % at pitch angles of 10°. The observed error at pitch angles of 15° and 20° was less than 5 %. Kang et al. [54] corroborated the observed results by reporting errors of −2 % at −10° pitch angle misalignment and errors up 4 % at pitch angles of 10°.

- **Reynolds number**

  Reynolds number is a dimensionless quantity used to characterize fluid flow. Reynolds number based on diameter is defined as

$$\mathrm{Re_D} := \frac{\rho \overline{u}_{\text{bulk}} D}{\mu} = \frac{\overline{u}_{\text{bulk}} D}{\nu}, \tag{3.12}$$

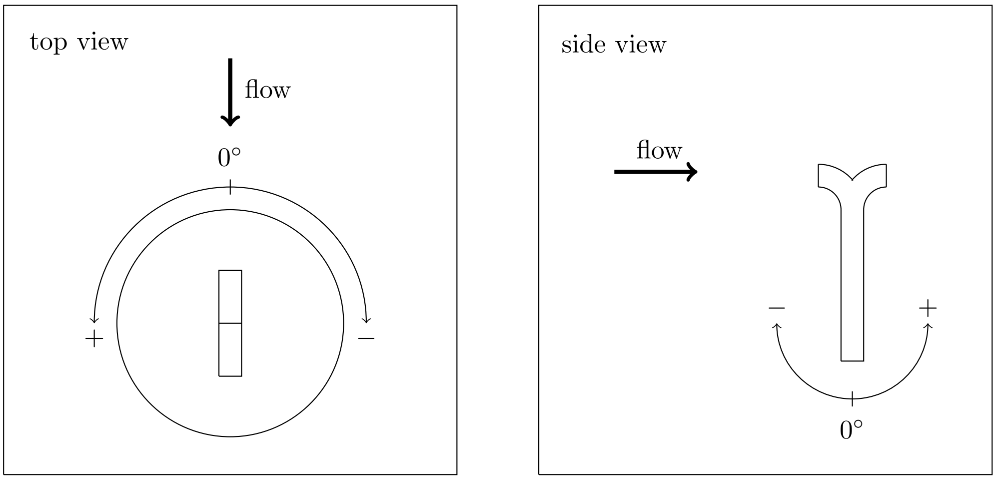

(a) Yaw (b) Pitch

Figure 3.4: Misalignment of an S-type pitot tube: (a) yaw angle and (b) pitch angle. Adapted from Williams and DeJarnette [102].

where D is the diameter of a stack or pipe, μ is the dynamic viscosity, and ν is the kinematic viscosity. At constant kinematic viscosity ν and diameter D, Leland et al. [65] performed measurements for varying Reynolds numbers $\mathrm{Re_D}$ by changing bulk velocity $\overline{u}_{\mathrm{bulk}}$. The researchers reported negative as well as positive errors with increasing Reynolds number $\mathrm{Re_D}$.

Normally, density ρ and dynamic viscosity μ of gases in an exhaust stack are very different from gases in a calibration facility due to, for example, high altitude and high temperature. This means that at the similar bulk velocities $\overline{u}_{\mathrm{bulk}}$, the Reynolds number $\mathrm{Re_D}$ of the flow in the exhaust stack may be different than the Reynolds number $\mathrm{Re_D}$ during calibration. It is important to calibrate the pitot tube over a range of velocities and corresponding Reynolds numbers $\mathrm{Re_D}$. If calibration coefficient K is approximately constant with Reynolds number $\mathrm{Re_D}$, the error for measuring gases in an exhaust stack will be small or negligible. If not, calibration coefficient K must be determined for Reynolds number $\mathrm{Re_D}$ of the flow in the exhaust stack [65].

- **Blockage**

  As discussed in Section 3.1, the pitot tube reduces the cross-sectional area of the flow slightly. Following the continuity equation, the reduction in the flow area results in an increased measured velocity. Leland et al. [65] added a correction for blockage to (3.10), such that

$$\overline{u}_z = K\frac{(A - A_{\mathrm{pitot}})}{A}\sqrt{\frac{2\Delta p}{\rho}}, \tag{3.13}$$

  where $(A - A_{\mathrm{pitot}})$ is the reduced cross-sectional area of the exhaust stack when the pitot tube is in place. Note that this correction in not included in the Standard Reference Method (SRM) for measurements of emissions from large-size combustion stacks.

3.2.1 Effects of shear and wall proximity

Whereas the impact of blockage and wall effects on measurement uncertainty is discussed, though briefly, in the Standard Reference Method (SRM), the effects of shear and wall proximity are not considered. To date, no research has been done on the influence of shear and proximity of the wall on the uncertainty of S-type pitot tube measurements. Literature is limited to studies performed with L-type (standard) pitot tubes shown in Figure 3.5. This section gives a short overview of developed

Figure 3.5: L-type (standard) pitot tube [81].

corrections for shear and wall proximity based on experiments with L-type pitot tubes. The fitness of the corrections for S-type pitot tube measurements is studied in Section 6.3.

The streamline pattern of the flow is deflected when a pitot tube is positioned in close proximity to the wall. Two mechanisms for streamline displacement are identified. In shear flow, such as the boundary layer, the presence of the pitot tube deflects the streamlines towards a region of lower velocity. As a result, the pitot tube registers a velocity that is higher than the velocity at the geometric center of the pitot tube (Figure 3.6a). This interference effect can be accounted for by a displacement correction Δy for the location of the pitot tube

$$\frac{\Delta y}{d_\mathrm{p}} = \epsilon, \tag{3.14}$$

where d_p is the outer diameter of the orifices of the pitot tube. MacMillan [68] proposed the most widely used constant value of $\epsilon = 0.15$, while other researchers suggested $0.08 < \epsilon < 0.16$ (see for example Livesey [66], and Tavoularis and Szymczak [89]). More recently, McKeon et al. [71] introduced a value for ϵ dependent on the local velocity gradient

$$\epsilon = 0.15 \tanh\left(4\sqrt{\gamma}\right), \tag{3.15}$$

where γ is a non-dimensional velocity gradient

$$\gamma = \frac{d_\mathrm{p}}{2\overline{u}_z}\frac{\mathrm{d}\overline{u}_z}{\mathrm{d}y}. \tag{3.16}$$

This correction asymptotes to the MacMillan value of $\epsilon = 0.15$ in strong velocity gradients, and has the advantage that it gives $\epsilon = 0$ in uniform flow.

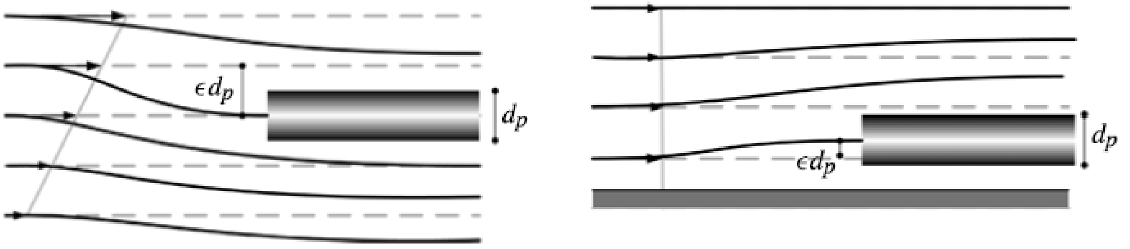

(a)

(b)

Figure 3.6: Streamline displacement due to (a) shear and (b) wall proximity. From Bailey et al. [5].

An additional mechanism for streamline displacement is present close to the wall. Considering a pitot tube touching the wall in uniform flow, it may be expected that the streamlines are displaced away from the wall (Figure 3.6b). This is a deflection towards the region of higher velocity. McMillan [68] suggested that pitot tube measurements can be corrected for the proximity of the wall by application of the following adjustment to the velocity

$$\frac{\Delta\overline{u}_z}{\overline{u}_z} = 0.015 \exp\left[-3.5\left(\frac{y}{d_p} - 0.5\right)\right]. \tag{3.17}$$

This adjustment should be used in addition to the displacement correction (3.14) for $y/d_\mathrm{p} < 2$. Note that this correction is Reynolds number $\mathrm{Re_D}$ independent.

McKeon et al. [71] state that the effects of both shear and wall proximity for $y/d_\mathrm{p} < 2$ are best corrected by

$$\epsilon = \begin{cases} 0.150 & \text{for } d^+ < 8, \\ 0.120 & \text{for } 8 < d^+ < 110, \\ 0.085 & \text{for } 110 < d^+ < 1600, \end{cases} \tag{3.18}$$

where $d^+ = d_\mathrm{p} u_\tau / \nu$. And that further from the wall, the free shear displacement correction (3.15) should be used.

3.3 Final remarks

In this chapter, we discussed standardized methods for measuring mass emissions from combustion plants. Volume flow rate Q is determined from a number of local velocity measurements in the exhaust stack. We identified sources of error in S-type pitot tube measurements of local velocity $\overline{u}_z$, such as misalignment, blockage, shear, and wall proximity. Furthermore, we identified sources of error in computation of volume flow rate Q. A limited number of point measurements may not be sufficient to characterize the flow profile properly. Furthermore, the measurement locations of local velocity may be source of error. By taking no samples in the near wall region, volume flow rate Q may be overestimated (wall effect).

The current standard measurement practice is developed for exhaust stacks of large-size combustion plants. Applying standardized methods in narrow stacks (diameter $D < 0.5\,\mathrm{m}$) of medium-size combustion plants raises a number of concerns. Following standard EN 15259 [39], one sampling point is sufficient to determine volume flow rate Q in narrow stacks of $D < 0.35\,\mathrm{m}$, and four sampling points are sufficient otherwise (Table 3.1). The contribution by the limited number of sampling points to the uncertainty of volume flow rate Q is unknown.

Furthermore, the impact of blockage on measurement uncertainty is expected to be larger in narrow stacks since a relative larger area of the sampling plane is obstructed by the measuring device. Moreover, measurements in narrow stacks are more likely to be affected by shear and wall proximity effects. In this thesis, we use numerical simulations to investigate the flow field in narrow stacks. In addition, we perform S-type pitot tube measurements in a narrow stack to study various sources of error and measurement uncertainty.

Chapter 4

Large Eddy Simulation of Gas Flow in Narrow Stacks

Characterization of the flow field in exhaust stacks is key to accurate measurement of mass emissions from combustion plants. We use Large Eddy Simulation (LES) to study the mean velocity profile and turbulence statistics of gas flow in narrow stacks. Numerical modelling gives insight into phenomena that can describe the magnitude of sources of measurement error. Our test case is gas flow in a narrow exhaust stack (i.e. pipe) of diameter $D = 0.2\,\mathrm{m}$. The studied gas flow has a kinematic viscosity of $\nu = 1.515 \cdot 10^{-5}\,\mathrm{m}^2/\mathrm{s}$ and bulk velocity of $\overline{u}_{\mathrm{bulk}} = 3.333\,\mathrm{m/s}$, corresponding to a Reynolds number of $\mathrm{Re}_{\mathrm{D}} = 44,000$.

A brief review of the characteristic mean velocity profile and turbulence statistics of fully developed turbulent pipe flow is given in Section 4.1. We introduce the parameters that we investigate with LES. Next, we discuss turbulence modelling and numerical methods in Section 4.2. We focus on LES with the open-source CFD solver OpenFOAM. Furthermore, we explain the setup of our numerical simulation, including spatial and time discretization, boundary and inlet conditions. The numerical uncertainty of our LES is estimated by the Least Squares version of the GCI method in Section 4.3. Moreover, we present the results of our simulations in Section 4.4.

4.1 Flow characteristics

Pipe flow is used in a wide range of engineering applications, for example, heating and cooling systems, water supply networks, oil transport, and combustion processes. Due to its common technical application, pipe flow has been studied extensively. Table 4.1 gives an overview of high-quality experimental research on fully developed turbulent pipe flow.

Table 4.1: Overview of experimental research on turbulent pipe flow.

Reference	Reynolds number Re_{D}
Nikuradse (1932) [74]	4,000 6,100 9,200 16,700 23,300 43,400 105,000 205,000 396,000 725,000 1,536,000 1,959,000 2,350,000 2,790,000 3,240,000
Laufer (1954) [62]	50,000 500,000
den Toonder & Nieuwstadt (1997) [17]	5,000 10,000 17,500 25,000
McKeon et al. (2004) [70]	74,345 144,580 309,630 536,930 753,590 1,346,200 3,105,000 6,112,700 10,314,000 18,308,000 35,724,000

The motion of viscous fluids, like gas, is described by the Navier-Stokes equations [77]. For incompressible flow:

$$\frac{1}{r}\frac{\partial r u_r}{\partial r} + \frac{1}{r}\frac{\partial u_\theta}{\partial \theta} + \frac{\partial u_z}{\partial z} = 0, \tag{4.1}$$

$$\begin{aligned}\frac{\partial u_r}{\partial t} + u_r\frac{\partial u_r}{\partial r} + \frac{u_\theta}{r}\frac{\partial u_r}{\partial \theta} + u_z\frac{\partial u_r}{\partial z} - \frac{u_\theta^2}{r} \\ = -\frac{1}{\rho}\frac{\partial p}{\partial r} + \nu\left(\frac{\partial^2 u_r}{\partial r^2} + \frac{1}{r^2}\frac{\partial^2 u_r}{\partial \theta^2} + \frac{\partial^2 u_r}{\partial z^2} + \frac{1}{r}\frac{\partial u_r}{\partial r} - \frac{2}{r^2}\frac{\partial u_\theta}{\partial \theta} - \frac{u_r}{r^2}\right),\end{aligned} \tag{4.2}$$

$$\begin{aligned}\frac{\partial u_\theta}{\partial t} + u_r\frac{\partial u_\theta}{\partial r} + \frac{u_\theta}{r}\frac{\partial u_\theta}{\partial \theta} + u_z\frac{\partial u_\theta}{\partial z} + \frac{u_r u_\theta}{r} \\ = -\frac{1}{\rho r}\frac{\partial p}{\partial \theta} + \nu\left(\frac{\partial^2 u_\theta}{\partial r^2} + \frac{1}{r^2}\frac{\partial^2 u_\theta}{\partial \theta^2} + \frac{\partial^2 u_\theta}{\partial z^2} + \frac{1}{r}\frac{\partial u_\theta}{\partial r} + \frac{2}{r^2}\frac{\partial u_r}{\partial \theta} - \frac{u_\theta}{r^2}\right),\end{aligned} \tag{4.3}$$

$$\begin{aligned}\frac{\partial u_z}{\partial t} + u_r\frac{\partial u_z}{\partial r} + \frac{u_\theta}{r}\frac{\partial u_z}{\partial \theta} + u_z\frac{\partial u_z}{\partial z} \\ = -\frac{1}{\rho}\frac{\partial p}{\partial z} + \nu\left(\frac{\partial^2 u_z}{\partial r^2} + \frac{1}{r^2}\frac{\partial^2 u_z}{\partial \theta^2} + \frac{\partial^2 u_z}{\partial z^2} + \frac{1}{r}\frac{\partial u_z}{\partial r}\right).\end{aligned} \tag{4.4}$$

where r is the radial, ϕ is the circumferential, and z is the axial coordinate.

The behaviour of pipe flow depends mainly on the ratio of inertial to viscous forces in the fluid. The Reynolds number $\mathrm{Re_D}$ for internal flow in pipes, previously introduced in Section 3.2, is

$$\mathrm{Re_D} = \frac{\text{inertial forces}}{\text{viscous forces}} = \frac{\overline{u}_{\text{bulk}} D}{\nu}. \tag{4.5}$$

In most practical applications, pipe flow is laminar for $\mathrm{Re_D} \lesssim 2,300$, turbulent for $\mathrm{Re_D} \gtrsim 4,000$, and transitional in between [11].

Most flows in engineering, including gas flows in exhaust stacks, are turbulent. Turbulent flow is characterized by random fluctuations of swirls, called eddies, throughout the flow. The fluctuations provide a mechanism for momentum and energy transfer. In turbulent flow, an instantaneous quantity can be decomposed into a mean and a fluctuation [101]. The velocity component u_i can be expressed as

$$u_i = \overline{u}_i + u_i', \tag{4.6}$$

where $\overline{u}_i$ is the time-averaged velocity component and u_i' is the fluctuation. The components i represent the radial r, circumferential ϕ, and axial z directions. This operation (4.6) is called Reynolds decomposition. Turbulent pipe flow is considered to be fully developed when the velocity statistics no longer vary in the axial direction [77].

Turbulence in pipe flow is generated by shear. The total shear stress τ_{total} of a flow equals [101]

$$\frac{\tau_{\text{total}}}{\rho} = \underbrace{-\overline{u_r' u_z'}}_{\text{turbulent stress}} + \underbrace{\nu\frac{\partial \overline{u}_z}{\partial (R-r)}}_{\text{viscous stress}}, \tag{4.7}$$

where $R - r$ is the distance from the wall. The first term of (4.7) denotes the turbulent stress, also known as the Reynolds stress, and the second term of (4.7) is the viscous stress.

4.1.1 Mean velocity profile

The mean velocity profile of fully developed turbulent pipe flow is shown in Figure 4.1a. Turbulent flow in pipes is considered to consist of three regions, characterized by their distance from the wall: the viscous sublayer, the wall region, and the core region [101].

- *Viscous sublayer:* This is the thin layer next to the wall where viscous effects are dominant. The velocity gradient in this layer is nearly constant and turbulent stresses are negligible. Fluctuations do occur in this region, but they are induced by the turbulence above the viscous sublayer. Wall shear stress τ_{wall} equals

  $$\tau_{\text{wall}} = \rho\nu \frac{\partial \overline{u}_z}{\partial(R-r)}\Big|_{r=R}, \tag{4.8}$$

  and wall friction velocity u_τ is defined as

  $$u_\tau = \sqrt{\frac{\tau_{\text{wall}}}{\rho}}. \tag{4.9}$$

  By substituting (4.9) in (4.8), the velocity profile in the viscous sublayer can be expressed by the law of the wall:

  $$\frac{\overline{u}_z}{u_\tau} = \frac{(R-r)u_\tau}{\nu}. \tag{4.10}$$

  This expression satisfies the no-slip boundary condition: $\overline{u}_z = 0$ for $r = R$.

- *Wall region:* The total shear stress is approximately constant in this layer. Experiments show that the velocity is proportional to the logarithm of the wall distance in this region. The logarithmic velocity profile is

  $$\frac{\overline{u}_z}{u_\tau} = \frac{1}{\kappa}\ln\frac{(R-r)u_\tau}{\nu} + B, \tag{4.11}$$

  where $\kappa \approx 0.41$ is the Von Kármán constant, and B is an integration constant with value $B \approx 5$.

- *Core region:* This is the region in the pipe center. The flow is completely turbulent in this region, and viscous stresses are negligible compared to turbulent stresses.

For clarification, the non-dimensional units for velocity

$$\overline{u}_z^+ = \frac{\overline{u}_z}{u_\tau}, \tag{4.12}$$

and wall distance

$$(R-r)^+ = \frac{(R-r)u_\tau}{\nu}, \tag{4.13}$$

are introduced. The viscous sublayer profile (4.10) is valid for $(R-r)^+ < 5$, and the logarithmic profile (4.11) is valid for $(R-r)^+ > 30$. As a result, the mean velocity profile of turbulent pipe flow is given by

$$\overline{u}_z^+ = \begin{cases} (R-r)^+, & 0 \leq (R-r)^+ \leq 5, \\ \frac{1}{\kappa}\ln\Big((R-r)^+\Big) + B & (R-r)^+ > 30. \end{cases} \tag{4.14}$$

The intermediate region $5 < (R-r)^+ < 30$ is referred to as the buffer layer, where both turbulent stresses and viscous stresses are important. Figure 4.1b shows the non-dimensional mean velocity profile of turbulent pipe flow as function of the non-dimensional wall distance.

The theory of fully developed turbulent pipe flow leads to analytic expressions such as (4.14) for the mean velocity profile. The expressions contain free constants, for example the Von Kármán constant κ, that can be determined from the best available experimental data. By combining analytic expressions and studying experimental results, Gersten [44] derived formulae for the mean velocity profile of fully developed turbulent flow in smooth pipes. We use the so-called Gersten and Herwig profile (Figure 4.1a) as reference for our numerical and experimental results.

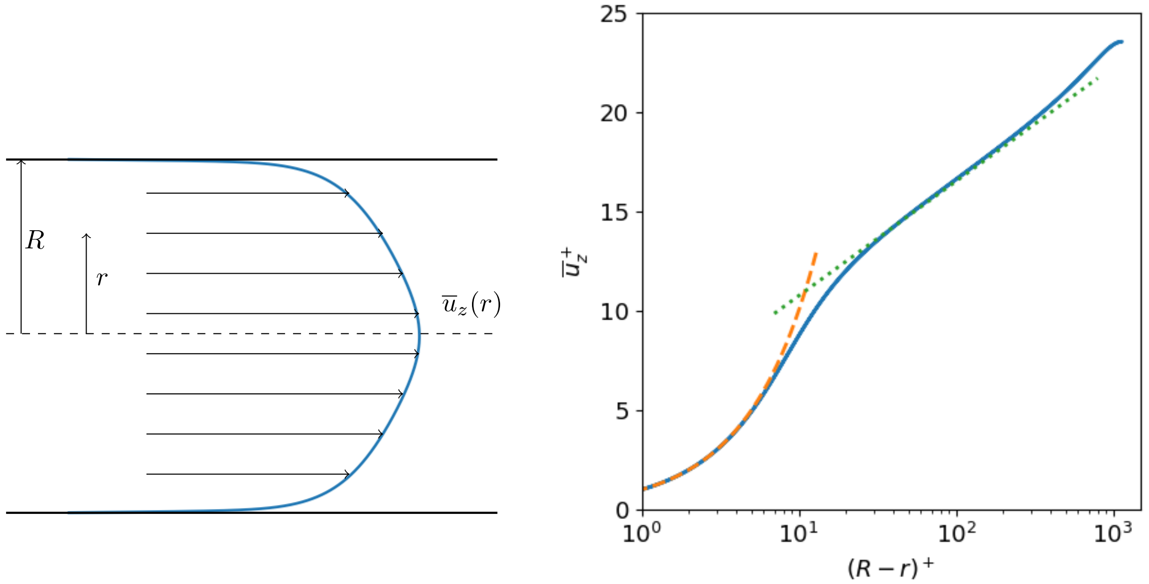

(a) (b)

Figure 4.1: Mean velocity profile of fully developed turbulent pipe flow. (a) Mean velocity $\overline{u}_z$ as function of r. Solid line: Gersten and Herwig profile [44]. (b) Mean velocity $\overline{u}_z^+$ as function of $(R-r)^+$. Solid line: Gersten and Herwig profile [44]; dashed line: $\overline{u}_z^+ = (R-r)^+$; dotted line: $\overline{u}_z^+ = 2.5\ln\Big((R-r)^+\Big) + 5$.

4.1.2 Friction

Pipe flow is considered to be fully developed when the pressure forces and viscous forces balance one another. Simplifying the balance of forces leads to the expression

$$-\frac{1}{\rho}\frac{\mathrm{d}\overline{p}}{\mathrm{d}z} = \frac{4u_\tau^2}{D}, \tag{4.15}$$

where pressure gradient $d\overline{p}/dz$ is constant in fully developed pipe flow. From (4.15), the pressure loss $\Delta\overline{p}$ in a pipe of length L can be expressed by

$$\Delta\overline{p} = f\frac{L}{D}\frac{\rho\overline{u}_{\mathrm{bulk}}^2}{2}, \tag{4.16}$$

where $\rho\overline{u}_{\mathrm{bulk}}^2/2$ denotes the dynamic pressure, and f is the Darcy-Weisbach friction factor

$$f = 8\left(\frac{u_\tau}{\overline{u}_{\mathrm{bulk}}}\right)^2. \tag{4.17}$$

Friction factor f in fully developed turbulent pipe flow depends on Reynolds number Re_D and roughness of the pipe. The Colebrook equation and Moody chart can be used to determine friction factor f of turbulent flow [11]. An estimate of friction factor f for a smooth pipe can be obtained by using Blasius correlation [77]

$$f = 0.3164\,{\mathrm{Re}_\mathrm{D}}^{-1/4}. \tag{4.18}$$

4.1.3 Turbulence statistics

Two-point correlation tensor R_{ij} characterizes the distance over which components of the fluctuating velocity field are correlated [77]. For homogeneous turbulence, the two-point correlation is a function of the difference between two vectors: $\underline{r}_2 - \underline{r}_1$. The two-point correlation for homogeneous flow is defined as

$$R_{ij}(\underline{r}_2 - \underline{r}_1) = \overline{u'_i(\underline{r}_1)u'_j(\underline{r}_2)}, \tag{4.19}$$

where $\underline{r}_i$ is the vector (r_i, ϕ_i, z_i). The two-point correlation gives insight in the spatial structure of turbulence, and has the following properties [101]:

1. $R_{ij}(0) = \overline{u'_i u'_j}$,
2. $R_{ij}(\underline{r}_2 - \underline{r}_1) = R_{ji}(\underline{r}_1 - \underline{r}_2)$,
3. $R_{ij}(\underline{r}_2 - \underline{r}_1) \to 0 \quad \text{for: } |\underline{r}_2 - \underline{r}_1| \to \infty$,

where the last property relates to the finite spatial dimensions of a turbulent eddy. The correlation tensor can be used to study the length scale of turbulence. The first property indicates that the two-point correlation reduces to the turbulent stress tensor for $\underline{r}_2 - \underline{r}_1 = 0$. The profiles of the normal stresses $R_{ii}(0) = \overline{u'_i u'_i}$ are characteristic for turbulent pipe flow.

The kinetic energy (per unit mass) e of the turbulent velocity fluctuations is defined as [101]

$$e = \frac{1}{2}\overline{u'_i u'_i} = \frac{1}{2}R_{ii}(0), \tag{4.20}$$

summed over the three coordinate directions. The energy cascade provides a relation between the turbulent kinetic energy e and the wave numbers κ of eddies, such that

$$e = \int_0^\infty E(\kappa)\,\mathrm{d}\kappa. \tag{4.21}$$

where $E(\kappa)$ is the turbulent kinetic energy spectrum. Figure 4.2 shows the energy cascade. Turbulent kinetic energy e is produced in the macro-structure of the flow by instability mechanisms. Due to interaction between eddies of various scales, energy is passed from large-scale eddies (low κ) to small-scale eddies (high κ). The universal pattern is a $k^{-5/3}$ decay in $E(\kappa)$ through a wide range of wave

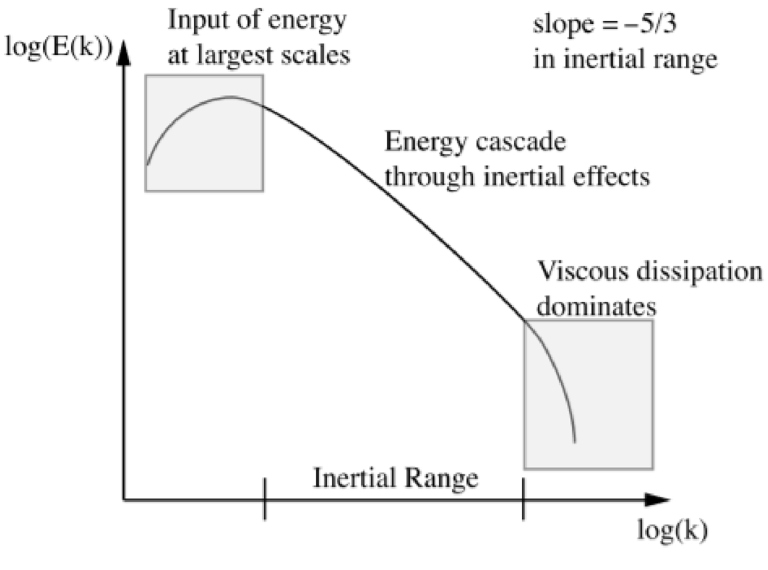

Figure 4.2: Sketch of the energy cascade by Berselli et al. [7].

numbers known as the inertial range. Via this cascade process, the energy eventually ends up at the micro-structure where the energy is dissipated into heat by viscosity. In case the turbulent pipe flow is fully developed, the rate of energy transfer is steady and e is independent of time.

4.2 Large Eddy Simulation

Computational Fluid Dynamics (CFD) codes have been successfully applied to a wide range of flow problems over the last two decades. With increasing computational power, more complex problems can be simulated with higher refinement. In this thesis, we use numerical modeling to study gas flow in narrow exhaust stacks. This section gives an overview of LES turbulence modeling with the open-source CFD solver OpenFOAM. We discuss spatial filtering, and introduce two subgrid-scale models: the Smagorinsky model and the WALE model. Furthermore, we discuss the setup of our numerical simulations. This includes spatial and temporal discretization, boundary conditions, and initial conditions.

All scales of turbulent motion are resolved in a Direct Numerical Simulation (DNS). However, this requires a spatial and temporal resolution that often exceeds the computational resources available. In Large Eddy Simulation (LES), the large scales of turbulent motion are resolved whereas the smaller subgrid-scale motions are modeled. This system is computationally intensive but requires less computational cost than DNS. Instead of solving the full unsteady Navier-Stokes equations, a Reynolds-Averaged Navier-Stokes (RANS) formulation can be used whereby the unsteady velocity and pressure field are averaged in time. RANS simulations solve for the mean flow, and introduce models for the Reynolds stresses. The simulations are computationally cheaper than DNS, as well as LES.

We use the CFD solver OpenFOAM to perform Large Eddy Simulation (LES). The OpenFOAM code uses a Cartesian reference frame. The Navier-Stokes equations of incompressible flow in Cartesian coordinates are given by:

$$\begin{cases} \dfrac{\partial u_i}{\partial x_i} = 0, \\ \dfrac{\partial u_i}{\partial t} + u_j \dfrac{\partial u_i}{\partial x_j} = -\dfrac{1}{\rho}\dfrac{\partial p}{\partial x_i} + \nu \dfrac{\partial^2 u_i}{\partial x_j^2}, \end{cases} \tag{4.22}$$

where i denotes the velocity components in the x, y, and z direction.

4.2.1 Spatial filtering

The working principle of LES is to resolve the large scales in the flow and to model the small scales. The turbulent field is filtered to separate the large scale fluctuations from the small scale fluctuations. This filter operation of a variable f is formally written as

$$[f(\boldsymbol{x})] = \iiint_V G(\boldsymbol{\gamma} - \boldsymbol{x}) f(\boldsymbol{x}) \mathrm{d}^3\boldsymbol{\gamma}, \tag{4.23}$$

where $G(\boldsymbol{\gamma} - \boldsymbol{x})$ represents the filter function. A filtered variable is denoted by $[\ldots]$, and is referred to as the resolved scale.

A large variety of filters with different properties is available, see for a detailed discussion on different filters, for example, Sagaut [79]. A commonly used filter by finite volume methods, including OpenFOAM, is the 'box' or 'top-hat' filter [101]. This filter has a value of $1/V_f$ inside the volume $V_f = \Delta_f^3$, while its value is zero outside this volume, such that

$$G(\boldsymbol{\gamma} - \boldsymbol{x}) = \begin{cases} \dfrac{1}{V_f}, & \text{for: } \boldsymbol{\gamma} - \boldsymbol{x} \in V_f, \\ 0, & \text{elsewhere,} \end{cases} \tag{4.24}$$

where the integration volume V_f is centered around the point (x_1, x_2, x_3). By this filter operation, all fluctuations with a scale smaller than the filter length Δ_f are removed. When Δ_f is adjusted to the characteristic size of the numerical grid Δ, it follows that the filtered velocity field represents the macro-structure that is represented with the numerical grid.

Applying filter operation (4.23) to the Navier-Stokes equations (4.22), gives a formulation of the equations for the filtered variables that are solved numerically. Before performing the filter operation, the convective and viscous terms of the Navier-Stokes equations (4.22) are rewritten as

$$u_j \frac{\partial u_i}{\partial x_j} = \frac{\partial u_i u_j}{\partial x_j}, \tag{4.25}$$

$$\nu \frac{\partial^2 u_i}{\partial x_j^2} = \frac{\partial}{\partial x_j} \nu \left(\frac{\partial u_i}{\partial x_j} + \frac{\partial u_j}{\partial x_i} \right). \tag{4.26}$$

The filtered Navier-Stokes equations are

$$\begin{cases} \dfrac{\partial [u_i]}{\partial x_i} = 0, \\ \dfrac{\partial [u_i]}{\partial t} + \dfrac{\partial [u_i u_j]}{\partial x_j} = -\dfrac{1}{\rho} \dfrac{\partial [p]}{\partial x_i} + \dfrac{\partial}{\partial x_j} \nu \left(\dfrac{\partial [u_i]}{\partial x_j} + \dfrac{\partial [u_j]}{\partial x_i} \right). \end{cases} \tag{4.27}$$

The filtered product $[u_i u_j]$ is different from the product of the filtered velocities $[u_i] [u_j]$. The difference is the subgrid stress τ_{ij}:

$$\tau_{ij} = -\rho \left([u_i u_j] - [u_i] [u_j] \right). \tag{4.28}$$

Inserting (4.28) into the filtered Navier-Stokes equations (4.27) gives

$$\begin{cases} \dfrac{\partial [u_i]}{\partial x_i} = 0, \\ \dfrac{\partial [u_i]}{\partial t} + \dfrac{\partial ([u_i] [u_j])}{\partial x_j} = -\dfrac{1}{\rho} \dfrac{\partial [p]}{\partial x_i} + \dfrac{1}{\rho} \dfrac{\partial \tau_{ij}}{\partial x_j} + \dfrac{\partial}{\partial x_j} \nu \left(\dfrac{\partial [u_i]}{\partial x_j} + \dfrac{\partial [u_j]}{\partial x_i} \right). \end{cases} \tag{4.29}$$

Subgrid stress τ_{ij} (4.28) expresses how the filtered micro-structure exerts a stress on the large eddies resulting in the energy transfer from the resolved scales to the subgrid scales. Subgrid stress τ_{ij} (4.28) can be compared to turbulent stress $-\overline{u_i' u_j'}$. However, τ_{ij} only describes the stress of the micro-structure, whereas $-\overline{u_i' u_j'}$ is the stress on the mean flow due to all turbulence scales.

4.2.2 Subgrid-scale models

A closure hypothesis is required to solve the filtered Navier-Stokes equations (4.29). A subgrid-scale model is used to specify closure for the effects of the micro-structure. One of the first SGS models in literature is the Smagorinsky model [83]. In recent years, many other SGS models have been developed, most of them based on the original Smagorinsky model. See, for example, Sagaut [79] for an overview of available models. In this thesis, the Smagorinsky model and the Wall Adaptive Local Eddy viscosity (WALE) model are compared and assessed.

Smagorinsky model

The Smagorinsky model for subgrid stress τ_{ij} is based on an eddy-viscosity assumption

$$\tau_{ij} - \frac{1}{3} \delta_{ij} \tau_{kk} = 2 \rho \nu_{\text{sgs}} [\mathbf{S}_{ij}], \tag{4.30}$$

where δ_{ij} is the Kronecker symbol, and ν_{sgs} is the subgrid eddy viscosity. Model (4.30) relates the subgrid stress τ_{ij} to the filtered strain rate tensor $[\mathbf{S}_{ij}]$

$$[\mathbf{S}_{ij}] = \frac{1}{2}\left(\frac{\partial [u_i]}{\partial x_j} + \frac{\partial [u_j]}{\partial x_i}\right). \tag{4.31}$$

The isotropic part of the subgrid stress τ_{kk} is absorbed into the filtered pressure $[p]$, such that inserting (4.30) into the filtered Navier-Stokes equations (4.29) gives

$$\begin{cases} \dfrac{\partial [u_i]}{\partial x_i} = 0, \\ \dfrac{\partial [u_i]}{\partial t} + \dfrac{\partial([u_i]\,[u_j])}{\partial x_j} = -\dfrac{1}{\rho}\dfrac{\partial [p']}{\partial x_i} + \dfrac{\partial}{\partial x_j}\left(\nu + \nu_{\mathrm{sgs}}\right)\left(\dfrac{\partial [u_i]}{\partial x_j} + \dfrac{\partial [u_j]}{\partial x_i}\right), \end{cases} \tag{4.32}$$

where $[p']$ is the modified filtered pressure.

The subgrid eddy viscosity ν_{sgs} is modelled as

$$\begin{aligned} \nu_{\mathrm{sgs}} &= \mathcal{L}^2\sqrt{2\,[\mathbf{S}_{ij}]\,[\mathbf{S}_{ij}]} \\ &= \mathcal{L}^2||\mathbf{S}_{ij}||, \end{aligned} \tag{4.33}$$

where $||\mathbf{S}_{ij}||$ is the characteristic rate of strain. Mixing length $\mathcal{L}$ is proportional to the filter length Δ_f. The Smagorinsky constant C_s is defined as

$$C_s = \frac{\mathcal{L}}{\Delta}, \tag{4.34}$$

where Δ is the characteristic grid size. The effective resolution of LES can be controlled by C_s. When $\mathcal{L}$ is small compared to the numerical grid, the grid is too coarse to solve all fluctuations resulting in numerical truncation errors. On one hand, when $\mathcal{L}$ is large compared to the numerical grid, the grid is sufficient to represent all large eddies. On the other hand, too many fluctuations may be filtered away when $\mathcal{L}$ is chosen too large. The optimal state is found when $\Delta_f \sim \Delta$. Based on theoretical considerations on the energy equation for the subgrid energy, it follows that $C_s \sim 0.1 - 0.2$ [101].

By construction, ν_{sgs} (4.33) is nonzero in case of a velocity gradient. As a result of the no-slip boundary condition, the velocity gradient is large near a wall. However, turbulent fluctuations are damped, and ν_{sgs} should be zero. To this end, $\mathcal{L}$ is commonly modified by Van Driest damping [77]

$$\mathcal{L} = C_s\Delta\left[1 - \exp\left(\frac{-y^+}{A^+}\right)\right], \tag{4.35}$$

with the constant $A^+ = 26$. This is a modification based on non-dimensional distance from the wall y^+

$$y^+ = \frac{\Delta y\, u_\tau}{\nu}. \tag{4.36}$$

The use of Van Driest damping function requires small values of the Smagorinsky constant for wall-bounded flows. Values of $C_s = 0.065$ have been used for channel simulations, and values of $C_s = 0.1$ for pipe simulations [27].

In a preliminary study, we compare simulation results with various Smagorinsky constants C_s to find an adequate value for our pipe flow simulations. Figure 4.3 shows the one-dimensional (z-direction) energy spectrum for Smagorinsky constants $C_s = 0.17$ (OpenFOAM's default value), $C_s = 0.13$, $C_s = 0.10$, and $C_s = 0.07$. Note that the simulation results are obtained on a coarse grid of approximately 0.3 million cells. For each of the Smagorinsky constants, we observe the characteristic slope of $-5/3$. This indicates that the cut-off wave number that filters the energy spectrum in a resolved part and a modeled part lies within the inertial range. In this thesis, we use the smallest Smagorinsky constant of $C_s = 0.07$.

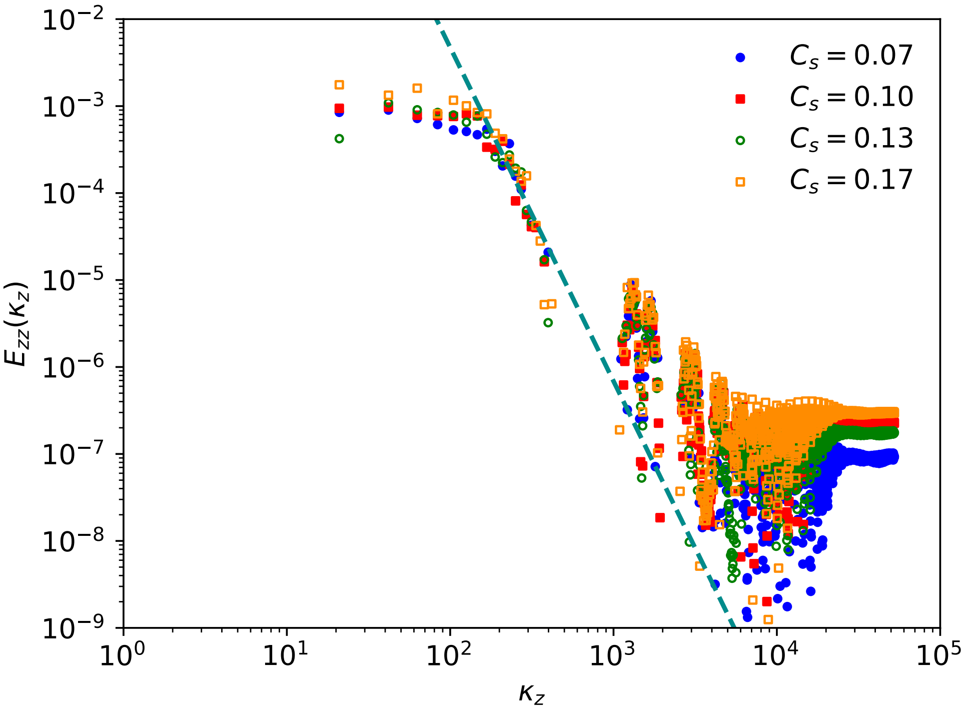

Figure 4.3: One-dimensional energy spectrum for different Smagorinsky constants C_s. Dashed line: slope $-5/3$; full circle: $C_s = 0.07$; full square: $C_s = 0.10$; open circle: $C_s = 0.13$; open square: $C_s = 0.17$.

WALE model

Nicoud and Ducros [73] developed the WALE subgrid-scale model which does not need a damping function to reproduce the effect of the no-slip condition. The WALE subgrid-scale model uses only local information to build ν_{sgs} as follows

$$\nu_{\text{sgs}} = \mathcal{L}^2 \frac{\left(\mathcal{S}^d_{ij}\mathcal{S}^d_{ij}\right)^{3/2}}{\left([\mathbf{S}_{ij}]\,[\mathbf{S}_{ij}]\right)^{5/2} + \left(\mathcal{S}^d_{ij}\mathcal{S}^d_{ij}\right)^{5/4}}, \tag{4.37}$$

where $\mathcal{S}^d_{ij}$ is the traceless symmetric part of the square of the velocity gradient tensor

$$\mathcal{S}^d_{ij} = \frac{1}{2}\left([g_{ij}]^2\,[g_{ji}]^2\right) - \frac{1}{3}\delta_{ij}\,[g_{kk}]^2, \tag{4.38}$$

where $[g_{ij}]$ denotes the velocity gradient

$$[g_{ij}] = \frac{\partial\,[u_i]}{\partial x_j}. \tag{4.39}$$

Likewise (4.35), filter length $\mathcal{L} = C_w\Delta$, where C_w is a (true) constant of $C_w = 0.325$.

4.2.3 Spatial discretization

OpenFOAM is based on the finite volume method for discretization of partial differential equations. The computational domain is divided into control volumes: the cells of the mesh. In OpenFOAM,

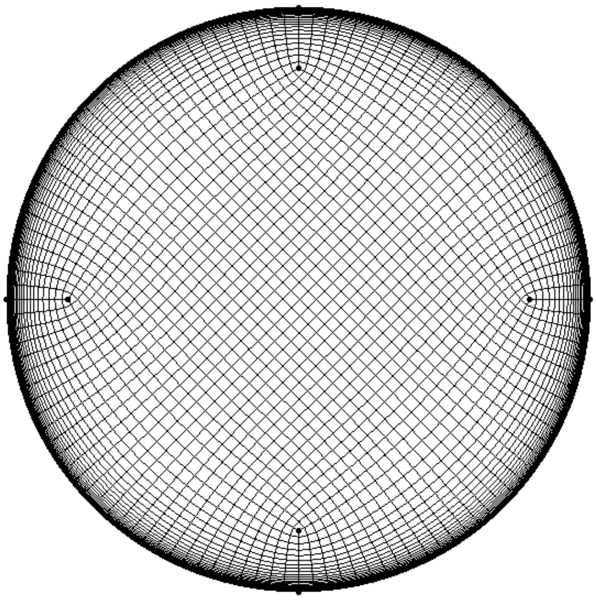

Figure 4.4: Constant z-plane of a structured OH-grid. The mesh consists of five domains. Total number of cells: $5 \cdot 30 \cdot 30 = 4500$ in the constant z-plane.

the values of the variables are stored at the centroids of the control volumes. The finite volume method, and its application to the Navier-Stokes equations is described in-depth in a large number of publications, see, for example, Moukalled et al. [72] for a discussion oriented to OpenFOAM.

In this thesis, we study gas flow in a pipe of diameter $D = 0.2\,\mathrm{m}$, and length $L = 1\,\mathrm{m}$. The mesh of the pipe geometry is created with the tool Pointwise. As is common for pipe flow simulations, we use a so-called structured OH-grid, see Figure 4.4. The mesh has five domains: a square in the center, and four domains at the wall of the pipe. In general, a higher mesh resolution gives a more detailed solution of the flow. We study simulations with four different meshes: approximately 0.3 million cells, 1.1 million cells, 2.5 million cells, and 4.9 million cells. Figures 4.5 and 4.6 show contours of instantaneous velocity u_z over a constant z-plane and θ-plane, respectively. One can observe that the simulations with a larger number of cells N exhibit much more fine-grain structures.

In general, discretization error δ_{discr} can be minimized by a fine resolution of the mesh. However, a finer mesh increases the computational cost of a simulation significantly. In general, a trade-off between accuracy and computational cost has to be made. We estimate discretization error δ_{discr} by applying the Least Squares version of the GCI method in Section 4.3. Table 4.2 gives an overview of the levels of mesh refinement used for estimation of discretization uncertainty $\mathbb{u}_{\mathrm{discr}}$.

To capture the generation of turbulence at the walls of the pipe, LES simulations require a non-

Table 4.2: Resolution and time step of meshes used to estimate discretization error δ_{discr}.

Label	Number of cells			Mesh resolution			Time step
	constant z-plane	z-direction	total	Δr^+	$(R\Delta\theta)^+$	Δz^+	Δt [s]
4	$5 \cdot 30 \cdot 30$	70	315000	< 1	≈ 26	≈ 164	$5 \cdot 10^{-4}$
3	$5 \cdot 45 \cdot 45$	105	1063125	< 1	≈ 17	≈ 110	$2 \cdot 10^{-4}$
2	$5 \cdot 60 \cdot 60$	140	2520000	< 1	≈ 13	≈ 82	$2 \cdot 10^{-4}$
1	$5 \cdot 75 \cdot 75$	175	4921875	< 1	≈ 10	≈ 66	$1 \cdot 10^{-4}$

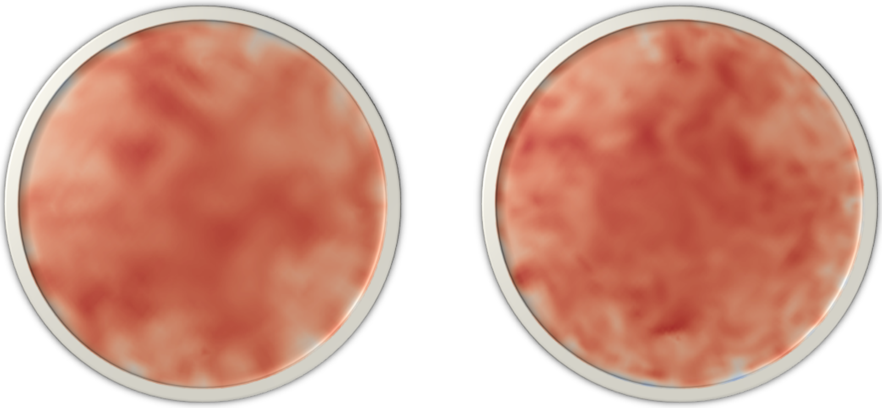

(a) $N \approx 0.3$ million

(b) $N \approx 1.1$ million

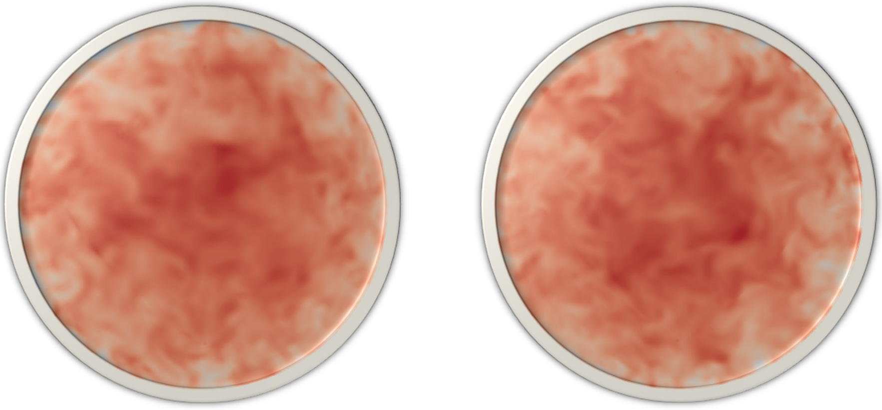

(c) $N \approx 2.5$ million

(d) $N \approx 4.9$ million

Figure 4.5: Visualization of turbulent pipe flow over a constant z-plane using contours of instantaneous u_z. Dark (red) represents higher values of u_z.

dimensional wall distance of

$$\Delta r^+ = \frac{\Delta r \, u_\tau}{\nu} < 1, \tag{4.40}$$

where Δr is the distance of the first cell-center from the wall of the pipe. We use a wall normal grid spacing of $\Delta r = 5 \cdot 10^{-5}\,\mathrm{m}$ to ensure that $r^+ < 1$ for all four grids. Likewise (4.40), grid spacing in other coordinate directions is characterized by $\Delta(R\theta)^+$ and Δz^+.

A number of recommendations for mesh resolution of LES simulations can be found in literature, each proposing approximately similar values. Kravchenko et al. [61] recommend a minimal grid spacing of $\Delta(R\theta)^+ \simeq 25$ and $\Delta z^+ \simeq 120$ for wall-bounded flows. According to Davidson [16], the required grid resolution is $\Delta(R\theta)^+ \simeq 30$ and $\Delta z^+ \simeq 100$. Piomelli and Chasnov [76] recommend a grid resolution for LES of $\Delta(R\theta)^+ \simeq 15 - 40$ and $\Delta z^+ \simeq 50 - 150$. An approximation of the mesh resolution of the grids used in this thesis is given in Table 4.2.

4.2.4 Time discretization

For the advance of a simulation in time, it is favourable that a fluid particle does not move more than one cell per time step Δt. This requirement is called the Courant-Friedrichs-Lewy (CFL) condition

$$\mathrm{CFL} = \Delta t \left(\frac{u_r}{\Delta r} + \frac{u_\theta}{r \Delta \theta} + \frac{u_z}{\Delta z} \right) \leq 1. \tag{4.41}$$

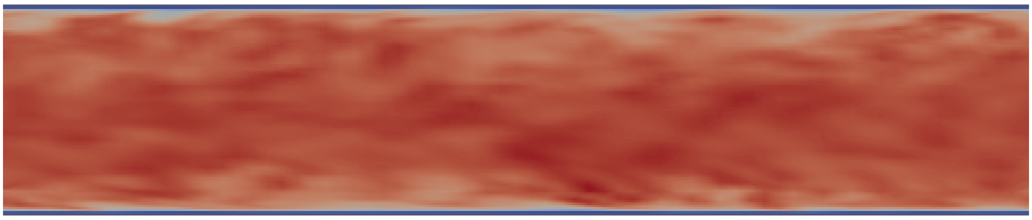

(a) $N \approx 0.3$ million

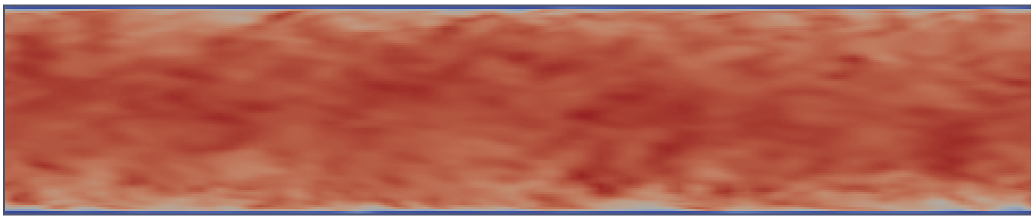

(b) $N \approx 1.1$ million

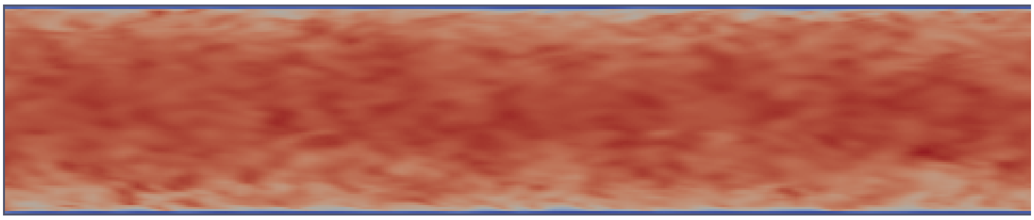

(c) $N \approx 2.5$ million

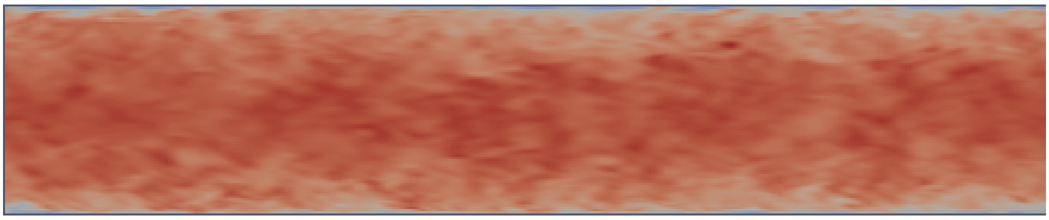

(d) $N \approx 4.9$ million

Figure 4.6: Visualization of turbulent pipe flow over a constant θ-plane using contours of instantaneous u_z. Dark (red) represents higher values of u_z.

The Courant number CFL varies for each cell at each time step in the simulation. Time step $\Delta\ t$ of the simulations in this thesis is shown in the last column of Table 4.2. The values are chosen such that $\text{CFL}_{\text{max}} < 0.8$.

4.2.5 Boundary conditions

Periodic boundary conditions are frequently used in studies of turbulent pipe flow to reduce computational cost. This is justifiable if the computational domain is sufficiently long so that large eddies are fully represented and the velocity fluctuations are uncorrelated at half the domain period [58]. Guala et al. [46] report that very large-scale motions in the outer region reach wavelengths of $8R$ to $16R$ long and large-scale motions with wavelengths of $2R$ to $3R$ occur throughout the layer.

Eggels et al. [28] performed DNS of turbulent pipe flow. The researchers used streamwise periodicity with a computational pipe length of $10R$, and reported correlations being nonzero at streamwise separation of half the pipe length, with values of approximately 0.08 near the wall. This suggests that their pipe length may have been insufficient. Wu and Moin [104] performed DNS of fully turbulent pipe flow and used a pipe length of $15R$. They reported correlations of 0.05 for the streamwise velocity components near the wall at the domain half period. To limit computational cost, we simulate flow in a pipe of length $10R$.

4.2.6 Inlet conditions

The treatment of turbulent inlet conditions for LES is a complex problem since the inlet flow must include a stochastically-varying component as well as satisfy the Navier-Stokes equations. Introducing a white noise random component to the expected velocity profile is not effective. The white noise does not have the spatial and temporal coherence characteristics of turbulent flow and dissipates quickly. Tabor and Baba-Ahmadi [88] classify the existing methods to create turbulent inlet conditions into two categories: synthetic inlets and precursor simulation methods.

Synthetic techniques attempt to construct a random field at the inlet with suitable turbulence-like properties. A common method is the use of Fourier techniques whereby the turbulent fluctuations are represented by a linear sum of sine and cosine functions, with coefficients representing the energy contained in each mode, see for example Lee et al. [64], Kondo et al. [60], and Smirnov et al. [84]. Another synthesis approach is principal orthogonal decomposition whereby (experimental) data of instantaneous realizations are decomposed into spatial and temporal eigenvectors. See for a more complete overview of different methods Tabor and Baba-Ahmadi [88].

Synthesis methods make it easy to specify parameters of turbulence, such as length scales and energy levels. Furthermore, they are easy to modify if conditions change. However, synthetic inlet conditions cannot be expected to be accurate and do no more than provide a trigger for the development of true turbulence within an inlet section. Fairly long development lengths are necessary before realistic turbulence is established.

Precursor simulation methods perform an explicit simulation of turbulence whose results are then utilized at the inlet to the main domain. They generate true turbulence and are inherently more accurate than synthetic methods. However, precursor methods are cumbersome to modify to the required state of turbulence, and the storage of long time series is impractical.

In this thesis, we use synthetic techniques, as well as precursor techniques. First, we use synthetic techniques to trigger turbulence and generate fully developed turbulent pipe flow. A combination of sine and cosine function is used to represent turbulent fluctuations at the pipe inlet. Turbulent pipe flow is initiated on a course mesh of approximately 0.3 million cells. When convergence is reached, the results are interpolated to a finer mesh, on which the computations are continued. These results are again interpolated to a finer mesh. Finally, the results are interpolated to the final mesh. Once fully developed turbulence is reached, the flow characteristics are no longer dependent on the inlet conditions.

The first simulations are a precursor to a another simulation setup. The resulting fully developed flow profile is used as inlet condition to a second simulation. In this simulation, we model flow in a pipe with an inserted S-type pitot tube. In this chapter, we discuss the simulation results of undisturbed fully developed pipe flow. In Chapter 5, we present the simulations results of pipe flow disturbed by an S-type pitot tube.

4.3 Numerical uncertainty of LES

Numerical uncertainty $\mathbb{u}_{\mathrm{num}}$ of our LES model is estimated by the procedure outlined in Section 2.3.1. All calculations in OpenFOAM are performed with double-precision, therefore $\delta_{\mathrm{round-off}} \approx 0$. Furthermore, iterative error δ_{iter} is reduced to a negligible level in comparison to discretization error δ_{discr}. For every time step, the residuals of the velocity components are reduced to order of magnitude 10^{-6}, and the residuals of the pressure are reduced to order of magnitude 10^{-7}. As a result, the expression

Table 4.3: Representative cell size h of meshes used to estimate discretization error δ_{discr}.

Label	Number of cells N	Volume of mesh V [m^3]	Representative cell size h [m]
1	4921875	0.0314136	0.0019
2	2520000	0.0314123	0.0023
3	1063125	0.0314096	0.0031
4	315000	0.0314016	0.0046

for estimated numerical uncertainty is equal to

$$\mathbb{u}_{\text{num}} \approx \mathbb{u}_{\text{discr}}. \tag{4.42}$$

The Least Squares version of the GCI method developed by Eça and Hoekstra [23] is used to determine discretization uncertainty $\mathbb{u}_{\text{discr}}$. Its procedure is described in detail in Appendix A.

Four grid refinement levels of approximately 0.3 million cells, 1.1 million cells, 2.5 million cells, and 4.9 million cells are selected to estimate discretization error δ_{discr}, see Section 4.2.3. Table 4.3 gives an overview of representative cell size h of the selected grids, where

$$h = \left(\frac{V}{N}\right)^{1/3}, \tag{4.43}$$

V is the volume of the grid, and N is the total number of cells in the grid. The size of the finest mesh is denoted by h_1, and the size of the coarsest mesh by h_4. Discretization error δ_{discr} is estimated for simulations with subgrid-scale models Smagorinksy and WALE. In this section, we determine numerical uncertainty $\mathbb{u}_{\text{num}}$ of the friction factor of the flow, and of the mean velocity profile. Friction factor f is an integral quantity of the flow, therefore it is often used in grid refinement studies. Additionally, we determine numerical uncertainty of the mean velocity profile since this variable is of key importance to our study on the uncertainty of flow velocity measurements.

Friction factor

We consider friction factor f of the pipe flow as key variable φ. Friction factor f is determined by rewriting the Darcy-Weisbach equation, such that

$$f = \frac{\Delta \overline{p}}{L} \frac{2}{\rho} \frac{D}{\overline{u}_{\text{bulk}}^2}. \tag{4.44}$$

Furthermore, the friction factor can be determined from the Blasius correlation (4.18). This gives us the opportunity to compare the estimated exact value of f by the Least Squares version of the GCI method, to the expected value of f from the Blasius correlation. The expected friction factor f is

$$f = 0.3164\, \text{Re}_\text{D}^{-1/4} = 0.0218. \tag{4.45}$$

Friction factor f as function of number of cells N is shown in Figure 4.7. Overall, the friction factor increases with grid refinement. Figure 4.7 shows mesh convergence, however, complete mesh independence is not reached with the selected levels of grid refinement. The WALE model predicts a lower friction factor than the Smagorinsky model for similar grid densities. The expected value of the friction factor from the Blasius correlation (4.45) is higher than the simulation results. As expected, the choice of subgrid-scale model becomes less important with grid refinement since a smaller fraction of the turbulent kinetic energy of the flow is modeled.

Discretization error δ_{discr} is estimated with a (truncated) power series expansions. As previously introduced in Section 2.3.1, the basic equation to estimate discretization error δ_{discr} is

$$\delta_{\text{discr}} \simeq \delta_{\text{RE}} = \varphi_i - \varphi_0 = \alpha h_i^p, \tag{4.46}$$

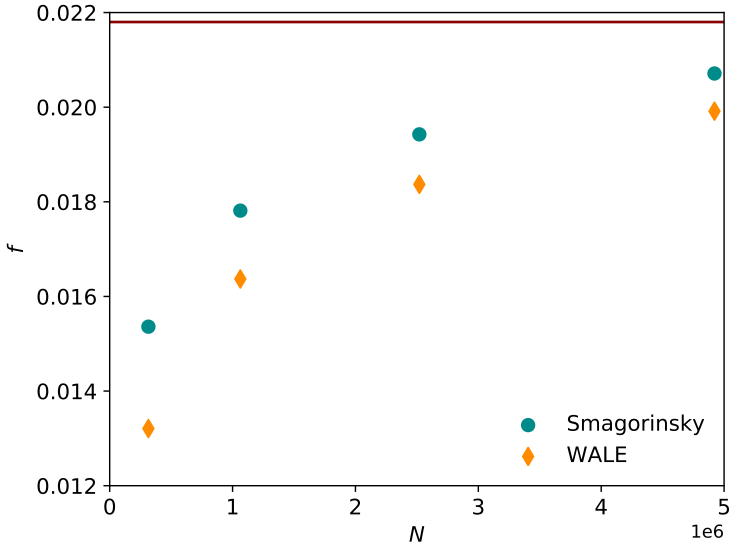

Figure 4.7: Friction factor f as function of number of cells N. Circle: Smagorinsky model; diamond: WALE model; solid line: Blasius correlation (4.45).

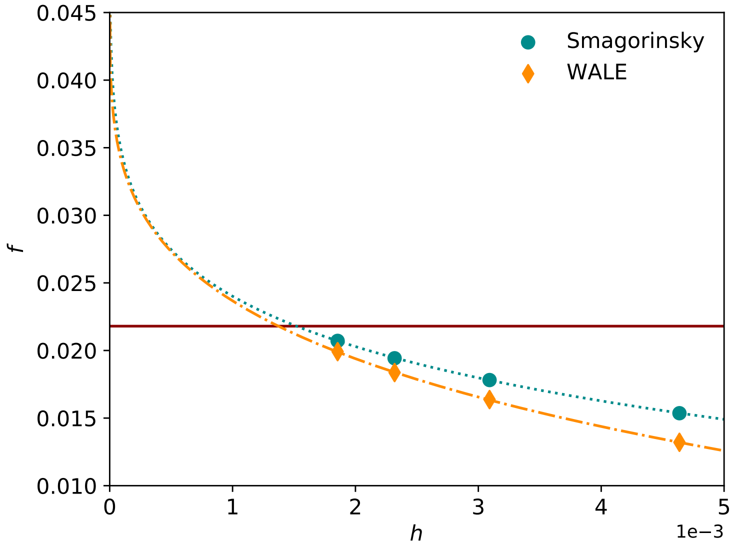

Figure 4.8: Friction factor f as function of representative cell size h. Circle: Smagorinsky model; diamond: WALE model; solid line: Blasius correlation (4.45); dotted line: fit (δ_{RE}) with observed order of convergence p for the Smagorinksy model; dash-dotted line: fit (δ_{RE}) with observed order of convergence p for the WALE model.

where φ_0 is the estimate of the exact solution, α is a constant, and p is the observed order of grid convergence. Table 4.4 presents estimated exact solution φ_0, standard deviation σ of the fit, and observed order of grid convergence p. Superscript$^{\mathrm{w}}$ denotes the weighted version of the power series expansion. Figure 4.8 shows friction factor f as function of representative cell size h. Furthermore, the graph shows the fit of the weighted solution of (4.46). The estimated exact solution φ_0 is the value of the fit at $h = 0$. We observe that the estimated exact solution is approximately twice to three times as high as expected from the Blasius correlation.

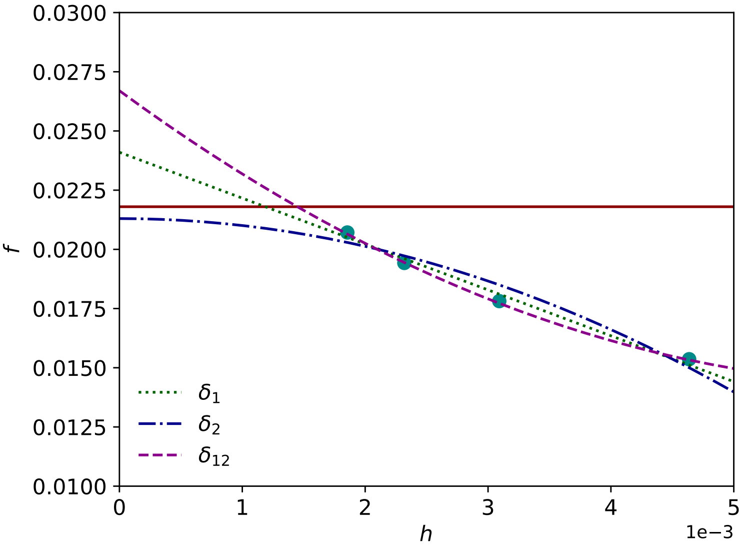

(a) Smagorinsky subgrid-scale model

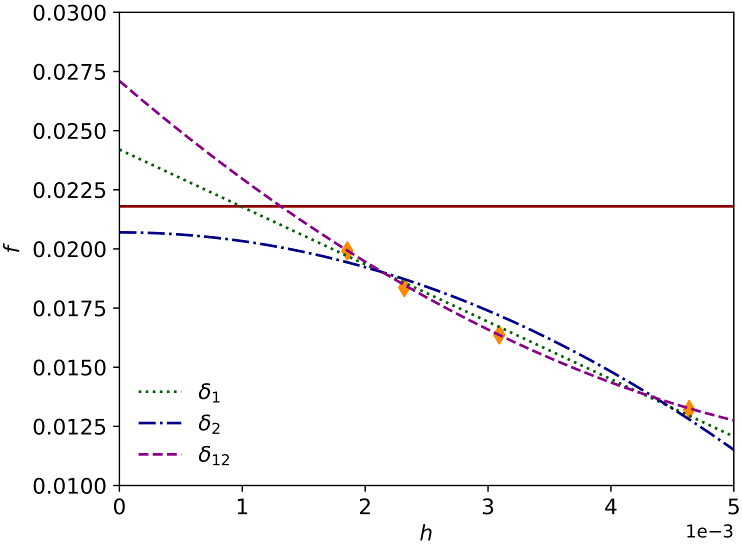

(b) WALE subgrid-scale model

Figure 4.9: Friction factor f as function of representative cell size h. Circle: Smagorinsky model; diamond: WALE model; solid line: Blasius correlation (4.45); dotted line: weighted single term expansion with first-order term (δ_1); dash-dotted line: weighted single term expansion with second-order term (δ_2); dashed line: weighted two-term expansion with first and second-order terms (δ_{12}).

The observed order of convergence is $p > 0$, and therefore friction factor f is considered to be monotonically converging with grid refinement. For a second-order method, Eça and Hoekstra [23] define an acceptable range of $0.5 \leq p \leq 2$. On one hand, a value of p greater than the formal order of grid convergence ($p > 2$) is likely to cause too small error estimates. On the other hand, if the value of p becomes too small ($p < 0.5$), δ_{RE} produces too conservative error estimates (when $p \rightarrow 0$, δ_{RE} tends to infinity). The error estimates of the simulations are deemed unreliable because the observed order of grid convergence is $p < 0.5$, see Table 4.4.

Table 4.4: Estimated exact value φ_0, standard deviation σ, and observed order of convergence p for different fits: δ_{RE}, δ_1, δ_2, and δ_{12}. Superscript$^{\mathrm{w}}$ denotes the weighted version.

		δ_{RE}	$\delta_{\mathrm{RE}}^{\mathrm{w}}$	δ_1	δ_1^{w}	δ_2	δ_2^{w}	δ_{12}	δ_{12}^{w}
Smagorinksy	φ_0	0.0770	0.0707	0.0239	0.0241	0.0211	0.0213	0.0267	0.0267
	σ	3.4e−5	3.3e−5	3.2e−4	3.2e−4	6.4e−4	6.4e−4	1.9e−4	8.4e−5
	p	0.0988	0.1107						
WALE	φ_0	0.0502	0.0485	0.0240	0.0242	0.0204	0.0207	0.0270	0.0271
	σ	4.2e−5	4.1e−5	3.5e−4	3.5e−4	7.5e−4	7.5e−4	2.0e−4	9.2e−5
	p	0.2176	0.2294						

Since the observed order of convergence p does not fall within the acceptable range for reliable estimates of discretization error δ_{discr}, three other error estimators are computed with and without weights:

- $\delta_{\mathrm{discr}} \simeq \delta_1 = \varphi_i - \varphi_0 = \alpha h_i$,
- $\delta_{\mathrm{discr}} \simeq \delta_2 = \varphi_i - \varphi_0 = \alpha h_i^2$,
- $\delta_{\mathrm{discr}} \simeq \delta_{12} = \varphi_i - \varphi_0 = \alpha_1 h_i + \alpha_2 h_i^2$.

Estimate of exact solution φ_0, and standard deviation σ of the fit obtained by different power series expansions are included in Table 4.4. Figures 4.9a and 4.9b show the different weighted fits for the Smagorinsky model and WALE model, respectively. Standard deviation σ is used as a measure of the quality of the fit. The weighted two-term expansion with first and second-order terms δ_{12}^{w} has the lowest standard deviation σ for the Smagorinsky model, as well as for the WALE model, and is therefore selected for error estimation.

It is common to expand discretization error δ_{discr} by a safety factor F_{s} to obtain expanded discretization uncertainty $\mathbb{U}_{\mathrm{discr}}$ (2.38). If the error estimation is deemed reliable, a safety factor $F_{\mathrm{s}} = 1.25$ is chosen, else $F_{\mathrm{s}} = 3$. Eça and Hoekstra [23] introduce data range parameter

$$\Delta_{\mathrm{discr}} = \frac{(\varphi_i)_{\mathrm{max}} - (\varphi_i)_{\mathrm{min}}}{n-1}, \tag{4.47}$$

to assess the quality of the fit to obtain error estimate δ_{discr}. In case $0.5 \leq p < 2.1$ and $\sigma < \Delta_{\mathrm{discr}}$, a safety factor of $F_{\mathrm{s}} = 1.25$ is chosen, otherwise $F_{\mathrm{s}} = 3$. We obtained the following measures for the quality of the fit:

- Smagorinsky subgrid-scale model: $\Delta_{\mathrm{discr}} = 0.0018$,
- WALE subgrid-scale model: $\Delta_{\mathrm{discr}} = 0.0022$.

Table 4.5: Discretization uncertainty $\mathbb{U}_{\mathrm{discr}}$ of friction factor f.

	Mesh	f [−]	$\mathbb{U}_{\mathrm{discr}}$ [−] $F_s = 1.25$	$\mathbb{U}_{\mathrm{discr}}$ [−] $F_s = 3$
Smagorinsky	h_1	0.0207	±0.0076 (±37 %)	±0.0182 (±88 %)
	h_2	0.0194	±0.0093 (±48 %)	±0.0221 (±114 %)
	h_3	0.0178	±0.0113 (±63 %)	±0.0269 (±151 %)
	h_4	0.0153	±0.0143 (±93 %)	±0.0343 (±224 %)
WALE	h_1	0.0199	±0.0090 (±45 %)	±0.0215 (±108 %)
	h_2	0.0184	±0.0110 (±60 %)	±0.0262 (±142 %)
	h_3	0.0164	±0.0135 (±82 %)	±0.0322 (±196 %)
	h_4	0.0132	±0.0174 (±132 %)	±0.0417 (±316 %)

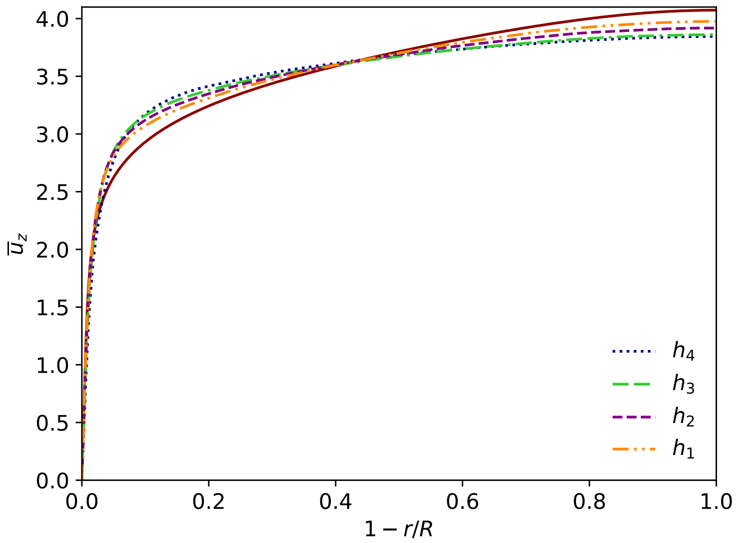

(a) Smagorinsky subgrid-scale model

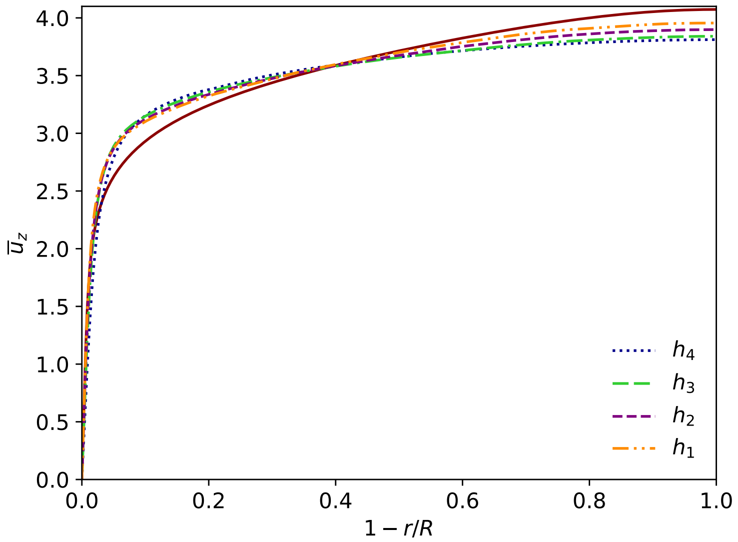

(b) WALE subgrid-scale model

Figure 4.10: Mean velocity $\overline{u}_z$ as function of $1 - r/R$. Solid line: Gersten and Herwig profile [44]; dotted line: h_4; dash-dotted line: h_3; dashed line: h_2; dash-dot-dotted line: h_1.

Following the guidelines by Eça and Hoekstra [23], our error estimation is unreliable, hence $F_\mathrm{s} = 3$. We note that the safety factor has a large influence on the resulting discretization uncertainty $\mathbb{U}_\mathrm{discr}$, therefore we compute discretization uncertainty with $F_\mathrm{s} = 1.25$, as well as $F_\mathrm{s} = 3$. For $\sigma < \Delta_\mathrm{discr}$:

$$\mathbb{U}_\mathrm{discr}(\varphi_i) = F_\mathrm{s} \, |\delta_\mathrm{discr}(\varphi_i)| + \sigma + |\varphi_i - \varphi_\mathrm{fit}|. \tag{4.48}$$

The estimated discretization uncertainty $\mathbb{U}_\mathrm{discr}$ has three components:

- Absolute value of the estimated discretization error times a safety factor,
- Standard deviation of the fit,

- Difference between the real data point and the value obtained from the fit for the same grid density.

Discretization uncertainty $\mathbb{U}_{\text{discr}}$ of friction factor f is shown in Table 4.5. We observe that the discretization uncertainty computed with safety factor $F_s = 3$ is extremely high. For example, for the simulation with the WALE subgrid-scale model and finest mesh h_1, the discretization uncertainty is $> 100\,\%$. Even the discretization uncertainty computed with safety factor $F_s = 1.25$ seems over-conservative. For comparison, we assume the Blasius correlation to give the true value of friction factor f, and we compute the discretization error. For the simulation with the Smagorinksy model and mesh h_1: $\delta_{\text{discr}} = 0.0207 - 0.0218 = -0.0011$. Expanding the absolute discretization error with a safety factor $F_s = 1.25$ gives a discretization uncertainty of ± 0.0013 or $\pm 6.6\,\%$. This value is much lower than the estimated discretization uncertainty by the Least Squares version of the GCI method: ± 0.0076 or $\pm 36.7\,\%$ (Table 4.5).

Mean velocity

We study mesh convergence of the mean axial velocity of the pipe flow. Figures 4.10a and 4.10b show the mean velocity profile for simulations with the Smagorinsky subgrid-scale model and WALE subgrid-scale model, respectively. As reference, the Gersten and Herwig profile [44] is included in the graphs. We observe that the simulated mean velocity profile improves with grid refinement. However, mesh independence is not reached with the selected grid resolutions.

We determine the discretization uncertainty of the mean axial velocity at locations $1 - r/R = 0.1$ and $1 - r/R = 1.0$ with the Least Squares version of the GCI method. The results are shown in Table 4.6. At location $1 - r/R = 0.1$, the observed order of convergence is $p = 0$ for the Smagorinsky subgrid-scale model and $p = 1.7$ for the WALE subgrid-scale model. Consequently, the discretization error is approximated by $\delta^{\text{w}}_{\text{RE}}$ and $F_{\text{s}} = 1.25$ for the WALE model. The discretization error for the Smagorinsky model is approximated by δ^{w}_{12} and $F_{\text{s}} = 3$. For comparison, the expected mean velocity by the Gersten and Herwig profile [44] is $\overline{u}_z = 2.93\,\text{m/s}$. This value is just inside interval 3.10 ± 0.17 of the Smagorinsky model and the finest grid, but outside interval 3.09 ± 0.04 of the WALE model

Table 4.6: Discretization uncertainty $\mathbb{U}_{\text{discr}}$ of mean velocity $\overline{u}_z$ at $1 - r/R = 0.1$ (top) and $1 - r/R = 1.0$ (bottom).

	Mesh	$\overline{u}_z$ [m/s]	$\mathbb{U}_{\text{discr}}$ [m/s] $F_s = 1.25$	$\mathbb{U}_{\text{discr}}$ [m/s] $F_s = 3$
Smagorinsky	h_1	3.10	±0.17 (±5 %)	±0.41 (±13 %)
	h_2	3.12	±0.20 (±6 %)	±0.47 (±15 %)
	h_3	3.15	±0.23 (±7 %)	±0.56 (±18 %)
	h_4	3.17	±0.28 (±9 %)	±0.62 (±20 %)
WALE	h_1	3.09	±0.04 (±1 %)	
	h_2	3.12	±0.08 (±3 %)	
	h_3	3.13	±0.09 (±3 %)	
	h_4	3.20	±0.18 (±6 %)	
Smagorinsky	h_1	3.98	±0.45 (±11 %)	±1.06 (±27 %)
	h_2	3.92	±0.52 (±13 %)	±1.24 (±31 %)
	h_3	3.86	±0.59 (±15 %)	±1.41 (±37 %)
	h_4	3.84	±0.61 (±16 %)	±1.46 (±38 %)
WALE	h_1	3.96	±0.43 (±11 %)	±1.02 (±26 %)
	h_2	3.90	±0.51 (±13 %)	±1.20 (±31 %)
	h_3	3.84	±0.57 (±15 %)	±1.36 (±35 %)
	h_4	3.81	±0.60 (±16 %)	±1.44 (±38 %)

and the finest grid. An error outside the uncertainty range can indicate modeling errors. Further grid refinement will most likely not result in a mean velocity of $\overline{u}_z = 2.93\,\mathrm{m/s}$.

We determine the discretization uncertainty of the mean velocity at the pipe center ($1 - r/R = 1.0$). The results are shown in Table 4.6. The discretization error of the Smagorinsky model, as well as the WALE model, is approximated by δ^{w}_{12} and $F_\mathrm{s} = 3$. Again, safety factor $F_\mathrm{s} = 3$ seems over-conservative, hence safety factor $F = 1.25$ is included in Table 4.6 as well. Following the Gersten and Herwig profile [44], the mean velocity is $\overline{u}_z = 4.08\,\mathrm{m/s}$ at the pipe center. This value is inside the uncertainty range of both the Smagorinsky model and WALE model. This suggest that further grid refinement may result in a mean velocity approaching $\overline{u}_z = 4.08\,\mathrm{m/s}$.

In this section, we determined the numerical uncertainty of the LES flow with the key variables: friction factor and mean axial velocity. Application of the Least Squares version of the GCI method shows that determining discretization uncertainty is not straightforward, and reliability of the result is debatable. Overall, the results show that our LES is under-resolved. Nonetheless, majority of our results suggest that further grid refinement will approach expected values of friction factor and mean velocity by Blasius correlation and the Gersten and Herwig profile [44], respectively. The required mesh resolution is however well beyond engineering possibilities. In the following section, we will discuss characteristics of the LES flow on the finest mesh (h_1).

4.4 LES results

In this section, we discuss the most important findings of our simulation results of fully developed turbulent pipe flow at $\mathrm{Re_D} = 44,000$. Where possible, we validate the results with experimental data from den Toonder and Nieuwstadt [17] for turbulent pipe flow at $\mathrm{Re_D} = 24,580$. Furthermore, we compare the present LES results to DNS data from Wu and Moin [104] for turbulent pipe flow at $\mathrm{Re_D} = 44,000$. The presented results are obtained by a simulation with a mesh of approximately 5 million cells (h_1), see Sections 4.2 and 4.3.

Flow statistics are collected for a period of $T = 20\,\mathrm{s}$. The sampling time is equivalent to $666.6R/\overline{u}_{\mathrm{bulk}}$, enough to allow a particle to travel 66 times through the pipe at bulk velocity. In addition to averaging in time, the statistical sample is enhanced by averaging in the two homogeneous directions (z, θ). A total of 108 profiles in r-direction are collected from the time-averaged flow field. Figure 4.11 shows the locations of the sampled profiles. The flow statistics are converted from the Cartesian coordinate system to the cylindrical coordinate system.

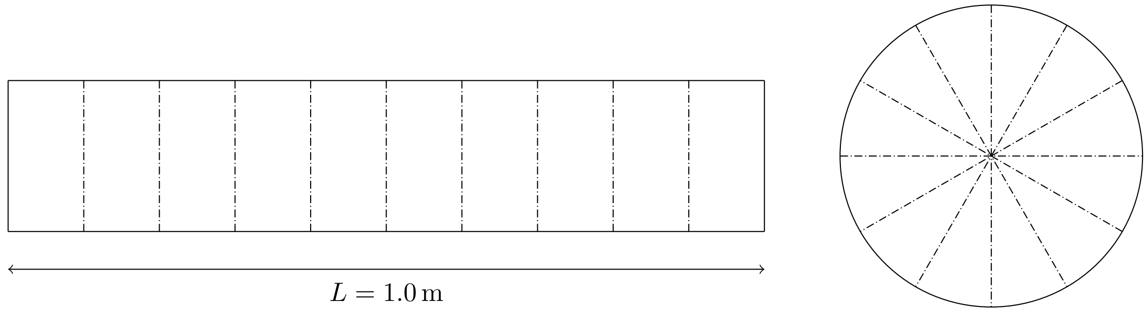

Figure 4.11: Sampling of flow statistics: 12 profiles of time-averaged flow statistics are sampled in r-direction across the constant z-plane (right). This is done at 9 locations in z-direction (left), adding up to a total of 108 sampled profiles.

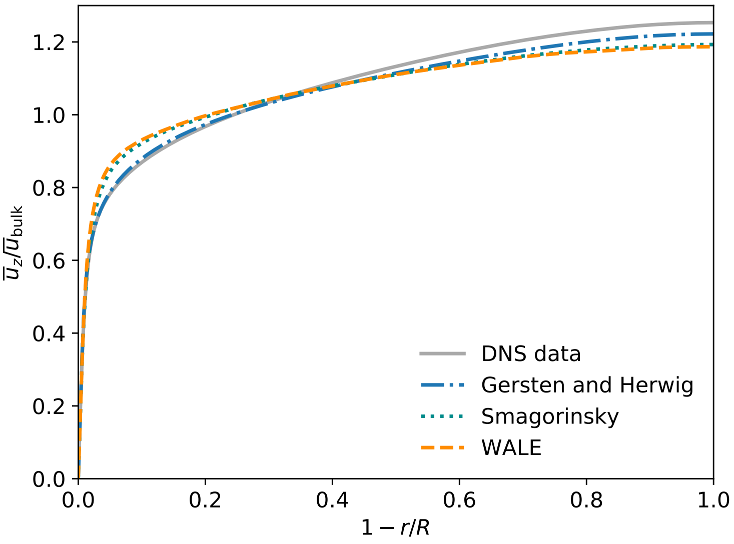

Figure 4.12: Mean velocity $\overline{u}_z/\overline{u}_{\mathrm{bulk}}$ as function of $1-r/R$. Solid line: DNS data by Wu and Moin [104]; dash-dotted line: Gersten and Herwig profile [44]; dotted line: present LES with Smagorinsky subgrid-scale model; dashed line: present LES with WALE subgrid-scale model.

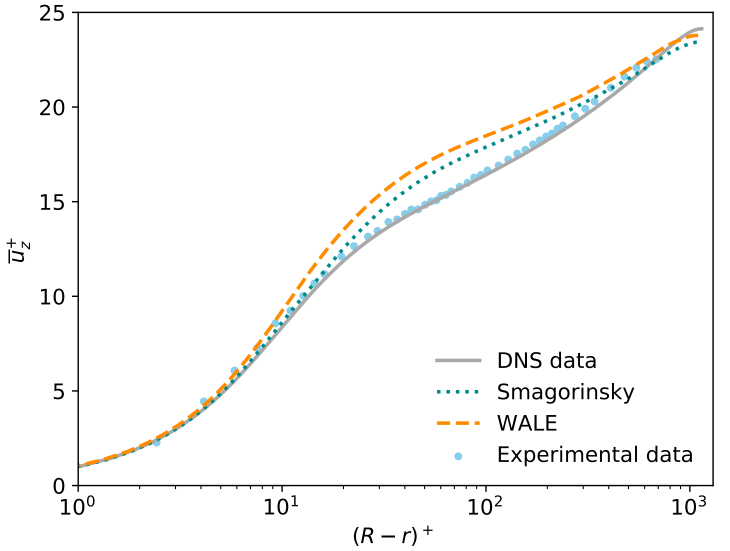

Figure 4.13: Mean velocity $\overline{u}_z^+$ as function of $(R-r)^+$. Solid line: DNS data by Wu and Moin [104]; dotted line: present LES with Smagorinsky subgrid-scale model; dashed line: present LES with WALE subgrid-scale model; circle: experimental data by den Toonder and Nieuwstadt [17].

4.4.1 Mean velocity profile

The mean velocity profile is shown in Figure 4.12. The present LES simulations predict a more uniform velocity profile than the DNS results [104] and reference Gersten and Herwig profile [44]. The LES flow over-predicts the axial mean velocity in the near wall region, but under-predicts the axial mean velocity at the pipe center. The regions cancel, leading to a correct bulk velocity. We observe that the DNS flow over-predicts the bulk velocity by approximately 1 %. The LES simulations with the Smagorinsky model and WALE model give comparable mean velocity profiles.

Figure 4.13 shows the mean velocity profile in wall units. The LES flow predicts the non-dimensional velocity $\overline{u}^+$ reasonably well in the viscous sublayer, but over-estimates $\overline{u}^+$ in the wall region. The simulation with the Smagorinsky model performs slightly better than the simulation with the WALE model. The present profiles seem typical of under-resolved LES flow, see, for example, studies by Gnambode et al. [45], Chatzikyriakou et al. [14], and Lund [67] for similar mean velocity profiles. The required mesh resolution for a perfect match with experimental data and DNS results is however beyond engineering possibilities.

4.4.2 Wall friction velocity

The wall friction velocity of pipe flow can be computed from either the velocity gradient at the wall, or the pressure gradient. We compare the results of both methods. Considering (4.8) and (4.9), the wall friction velocity is computed by the gradient of the velocity at the pipe wall, such that

$$u_{\tau,\mathrm{a}} = \sqrt{\nu \frac{\partial \overline{u}_z}{\partial (R-r)}\Big|_{r=R}}. \tag{4.49}$$

Considering (4.15), the wall friction velocity can also be computed by the pressure gradient, such that

$$u_{\tau,\mathrm{b}} = \sqrt{-\frac{1}{\rho}\frac{\mathrm{d}\overline{p}}{\mathrm{d}z}\frac{D}{4}}. \tag{4.50}$$

The results of both computations are shown in Table 4.7. We observe that the wall friction velocity computed from the velocity gradient $u_{\tau,\mathrm{a}}$ is approximately similar for simulations with the Smagorinsky model and WALE model. Furthermore, we notice that the differences between results computed from the velocity gradient $u_{\tau,\mathrm{a}}$, and from the pressure gradient $u_{\tau,\mathrm{b}}$, are less than 1.5 %. This indicates that our LES model, apart from the flow being under-resolved, is working well. The velocity gradient at the wall is obtained by interpolation. We assume the pressure gradient to be a more reliable parameter than the velocity gradient at the wall, hence we use values $u_{\tau,\mathrm{b}}$ in this chapter.

4.4.3 Turbulent and viscous shear stresses

Turbulent shear stress and viscous shear stress profiles are shown in Figures 4.14 and 4.15. The presented turbulent stress $\overline{u'_z u'_r}$ is the sum of the resolved stress and the subgrid-scale stress. The non-dimensional turbulent stress is computed by

$$\overline{u'_z u'_r}^+ = \overline{u'_z u'_r}/u_\tau^2, \tag{4.51}$$

and the non-dimensional viscous stress is computed by

$$\left[-\nu\frac{\mathrm{d}\overline{u}_z}{\mathrm{d}r}\right]^+ = -\nu\frac{\mathrm{d}\overline{u}_z}{\mathrm{d}r}/u_\tau^2. \tag{4.52}$$

Table 4.7: Wall friction velocity computed from the velocity gradient $u_{\tau,\mathrm{a}}$ (4.49) and the pressure gradient $u_{\tau,\mathrm{b}}$ (4.50).

	$u_{\tau,\mathrm{a}}$ [m/s]	$u_{\tau,\mathrm{b}}$ [m/s]
Smagorinsky	0.1682	0.1696
WALE	0.1684	0.1663

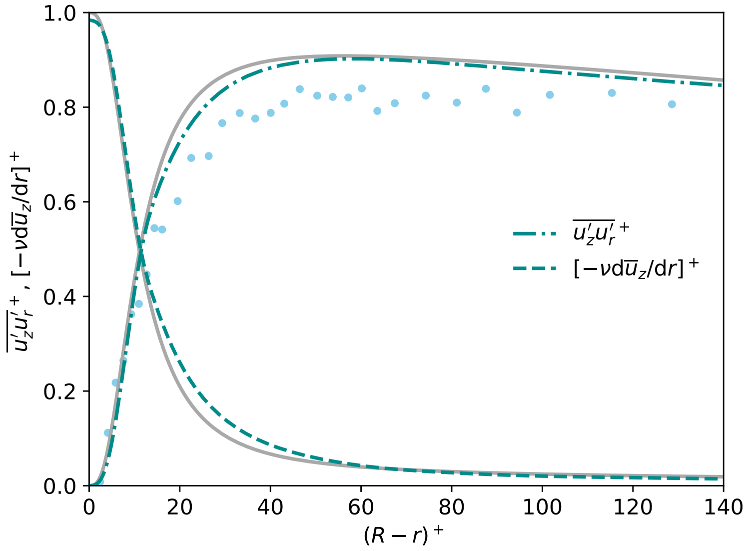

(a) Smagorinsky subgrid-scale model

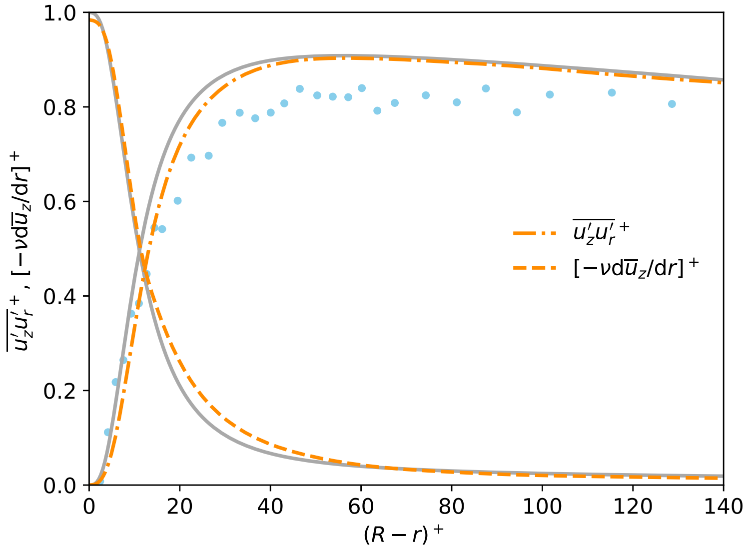

(b) WALE subgrid-scale model

Figure 4.14: Turbulent and viscous shear stresses as function of $(R-r)^+$. Dash-dotted line: $\overline{u_z'u_r'}^+$; dashed line: $[-\nu d\overline{u}_z/dr]^+$; solid line: DNS data by Wu and Moin [104]; circle: experimental data by den Toonder and Nieuwstadt [17].

Figure 4.14 shows the non-dimensional stresses as function of the non-dimensional wall distance. The viscous shear stress is dominant in the viscous sublayer, and the turbulent shear stress is negligible. Further away from the pipe wall, in the buffer layer, both viscous shear stress and turbulent shear stress are important. In the wall layer, the turbulent shear stress dominates over the viscous shear stress. We observe that the present simulation corresponds well with the DNS data by Wu and Moin [104].

Figure 4.15 shows the turbulent shear stress, as well as the total stress, as function of wall distance.

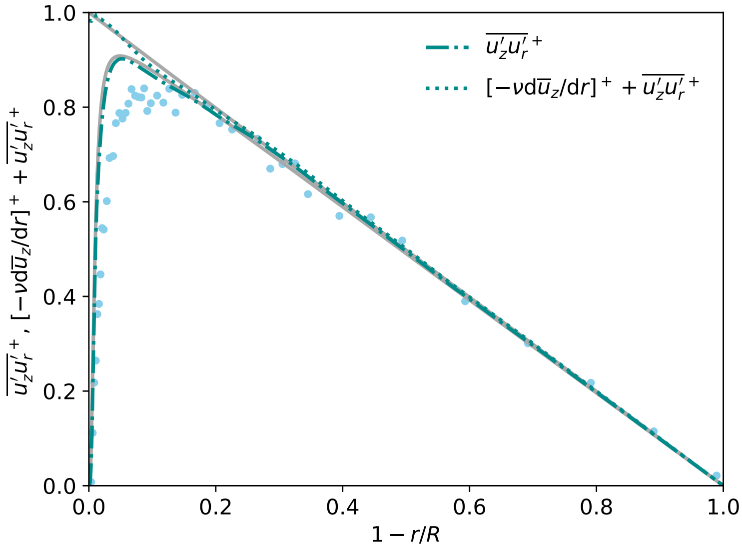

(a) Smagorinsky subgrid-scale model

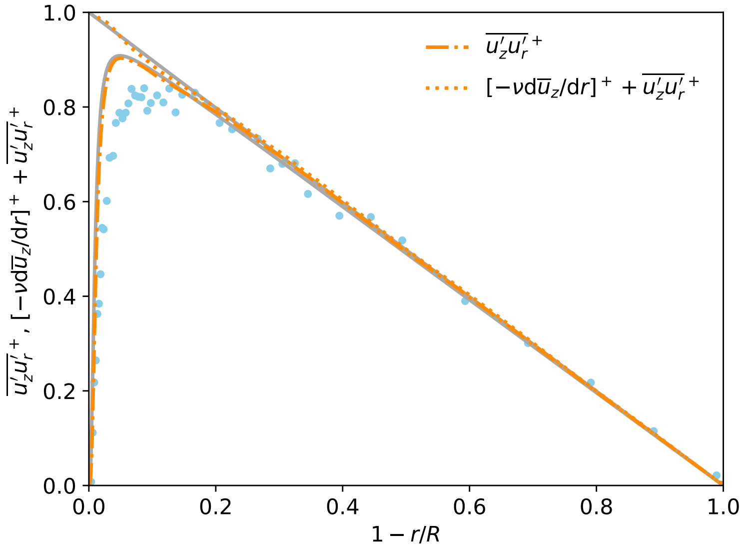

(b) WALE subgrid-scale model

Figure 4.15: Turbulent and total shear stresses as function of $1 - r/R$. Dash-dotted line: $\overline{u_z'u_r'}^+$; dotted line: $[-\nu \mathrm{d}\overline{u}_z/\mathrm{d}r]^+ + \overline{u_z'u_r'}^+$; solid line: DNS data by Wu and Moin [104]; circle: experimental data by den Toonder and Nieuwstadt [17].

We observe clear linear behaviour of the total stress close to the centerline. In the core region, viscous effects can be neglected, and turbulent shear stress $\overline{u_z'u_r'}$ is linear. We observe a clear peak in the turbulent shear stress in region near the wall. The peak values of the turbulent shear stress are $\overline{u_z'u_r'}^+ = 0.902$ for the Smagorinsky subgrid-scale model, and $\overline{u_z'u_r'}^+ = 0.903$ for the WALE subgrid-scale model. We compare these values to the relation given by Sreenivasan and Sahay [86]:

$$\left(\overline{u_z'u_r'}^+\right)_{\max} = 1 - \left(\frac{3.1 \pm 0.1}{\sqrt{\mathrm{Re}_\tau}} + \frac{0.93}{\sqrt{\mathrm{Re}_\tau}} \frac{\ln\left(\ln(\mathrm{Re}_\tau)\right)}{\ln(\mathrm{Re}_\tau)}\right), \tag{4.53}$$

where friction Reynolds number Re_τ is defined as

$$\mathrm{Re}_\tau = \frac{u_\tau R}{\nu}. \tag{4.54}$$

The friction Reynolds number for the simulation with the Smagorinsky model is $\mathrm{Re}_\tau = 1,119$, and for the simulation with the WALE model is $\mathrm{Re}_\tau = 1,098$. Applying (4.53) gives:

- $\left(\overline{u_z' u_r'}^+\right)_{\max} \in [0.900 \pm 0.003]$ for the Smagorinsky subgrid-scale model,
- $\left(\overline{u_z' u_r'}^+\right)_{\max} \in [0.899 \pm 0.003]$ for the WALE subgrid-scale model.

We observe excellent agreement between correlation (4.53) and the simulation value for the Smagorinsky model. The simulation value for the WALE model is just outside the range of correlation (4.53).

The LES flow does not match the experimental data of den Toonder and Nieuwstadt [17] in Figures 4.14 and 4.15. The Reynolds number of the experimental data is $\mathrm{Re}_\mathrm{D} = 24,580$, whereas the Reynolds number of the DNS data [104] and present LES is $\mathrm{Re}_\mathrm{D} = 44,000$. Previous studies, see for example Gnombode et al. [45], show that the distribution of the turbulent shear stress $\overline{u_z' u_r'}^+$ shifts towards the wall and has an enhanced peak with increasing Reynolds number Re_D due to more intense turbulent fluctuations. Therefore, a match between the present LES and experimental data is not expected nor desired.

4.4.4 Turbulent intensities

The root mean square profiles of the radial, circumferential, and axial turbulent velocity are presented in Figure 4.16. The non-dimensional turbulent intensities are computed by

$$u'^+_{r,\mathrm{r.m.s.}} = \sqrt{\overline{u_r' u_r'}}/u_\tau, \tag{4.55}$$

$$u'^+_{\theta,\mathrm{r.m.s.}} = \sqrt{\overline{u_\theta' u_\theta'}}/u_\tau, \tag{4.56}$$

$$u'^+_{z,\mathrm{r.m.s.}} = \sqrt{\overline{u_z' u_z'}}/u_\tau. \tag{4.57}$$

The total intensities (resolved + subgrid-scale) are presented in the left graphs, whereas the resolved intensities only are presented in the right graphs.

The top graphs of Figure 4.16 show the turbulent intensity in radial direction $u'^+_{r,\mathrm{r.m.s.}}$. We observe that the turbulent intensity is perfectly predicted by the resolved part of the present simulation. Consequently, the turbulent intensity is over-estimated when the subgrid-scale part is added to the resolved part of the simulation results. It is remarkable that the present simulations over-estimate the turbulent intensity. Previous studies [67, 106, 14] report under-estimation of the turbulent radial intensity by under-resolved LES. Close to the wall, we observe an unexpected peak in the simulation with the Smagorinsky subgrid-scale model. We cannot explain this behaviour, perhaps it is caused by the Van Driest damping function.

The middle graphs of Figure 4.16 show the turbulent intensity in circumferential direction $u'^+_{\theta,\mathrm{r.m.s.}}$. The turbulent intensity is under-estimated by the resolved part of the present simulation only, but over-estimated by the total simulation result. In previous studies [67, 106, 14], the turbulence circumferential intensity is under-estimated by under-resolved LES. We observe that the simulation with the WALE subgrid-scale model predicts the turbulent circumferential intensity reasonable well close to the wall of the pipe. Again, we observe a peak near the wall for the simulation with the Smagorinsky subgrid-scale model.

The bottom graphs of Figure 4.16 show the turbulent intensity in axial direction $u'^+_{z,\mathrm{r.m.s.}}$. We observe that the resolved part of the simulation over-estimates the turbulence close to the wall, but under-estimates the turbulence in core region. The total turbulence matches the DNS data by Wu and

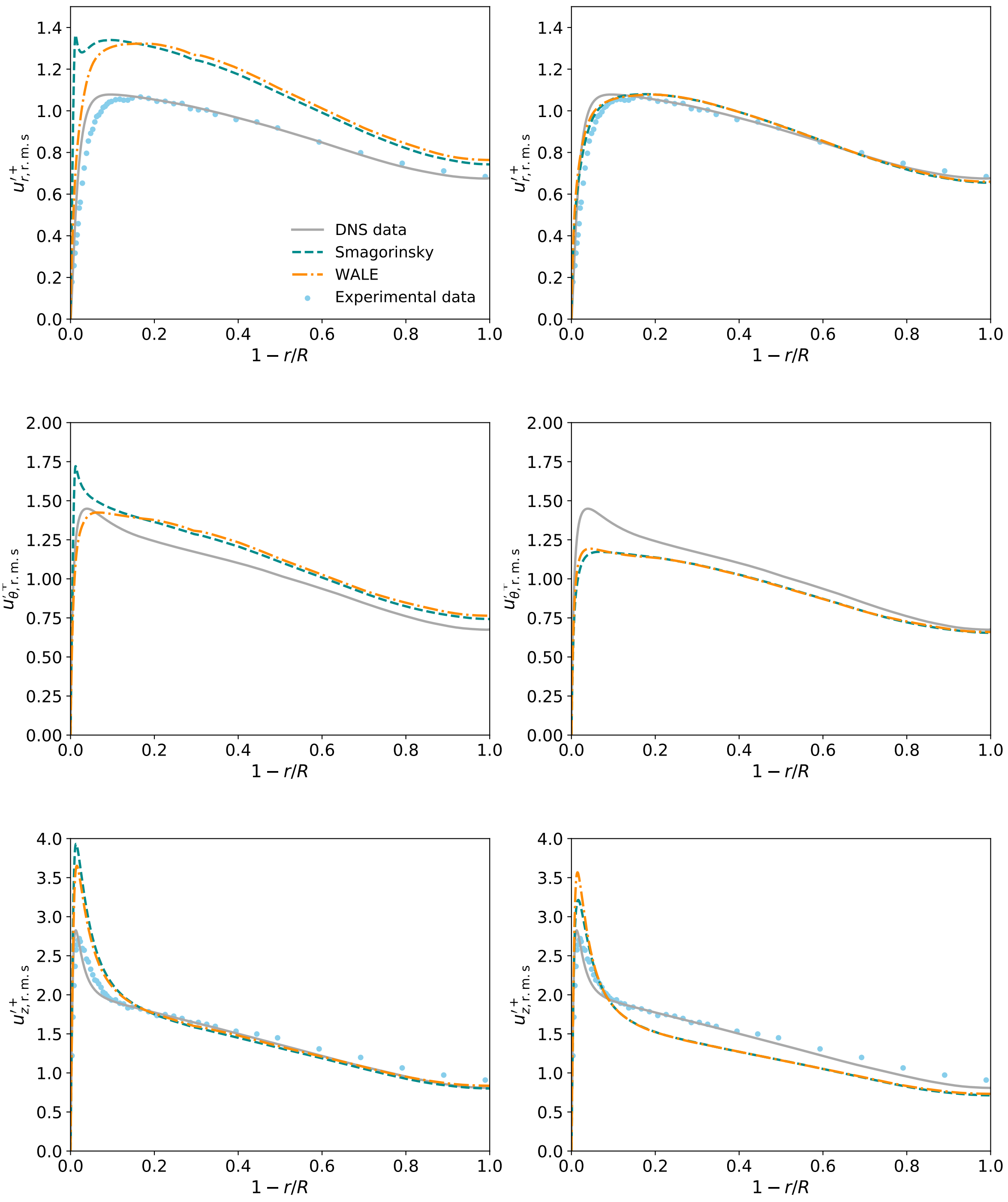

(a) Resolved + subgrid-scale turbulence

(b) Resolved turbulence

Figure 4.16: Turbulent intensities as function of $1-r/R$. Dashed line: present LES with Smagorinsky subgrid-scale model; dash-dotted line: present LES with WALE subgrid-scale model; solid line: DNS data by Wu and Moin [104]; circle: experimental data by den Toonder and Nieuwstadt [17]. Left: total (resolved + subgrid-scale) turbulence; right: resolved turbulence.

Moin [104] perfectly in the core region. In the wall region, we observe a peak in the total turbulence that is much higher than the DNS data or experimental data. Previous studies [67, 106, 14] report similar high peaks close to the wall in under-resolved LES.

The peak values of the non-dimensional axial turbulent intensity are $u'^{+}_{z,\mathrm{r.m.s.}} = 3.93$ for the Smagorinsky subgrid-scale model, and $u'^{+}_{z,\mathrm{r.m.s.}} = 3.65$ for the WALE subgrid-scale model. We compare these values to the relation by Bauer et al. [6] for pipe flow at $\mathrm{Re}_\tau > 360$:

$$\left(u'^{+}_{z,\mathrm{r.m.s.}}\right)_{\max} = \sqrt{0.67\ln(\mathrm{Re}_\tau) + 3.324}. \tag{4.58}$$

Correlation (4.58) gives:

- $\left(u'^{+}_{z,\mathrm{r.m.s.}}\right)_{\max} = 2.83$ for the Smagorinsky subgrid-scale model,
- $\left(u'^{+}_{z,\mathrm{r.m.s.}}\right)_{\max} = 2.83$ for the WALE subgrid-scale model.

The present simulation with Smagorinksy model and WALE model over-estimate the peak value with more than 25 %.

4.5 Final remarks

In this chapter, we discussed numerical simulations of gas flow in narrow stacks. Characterization of the flow field in stacks is vital to accurate measurement of mass emissions from combustion plants. By gaining insight in the mean velocity profile, suitable measurement locations can be selected for determining bulk velocity in narrow stacks. We performed LES of fully developed turbulent pipe flow with the open-source solver OpenFOAM. We investigated the influence of mesh refinement, and tested two subgrid-scale models: the Smagorinsky model and the WALE model. In the next chapter, the flow field around a pitot tube in a narrow stack is simulated to study blockage and wall effects. The simulation results of fully developed pipe flow discussed in this chapter are thereby used as inlet conditions.

We determined numerical uncertainty of the friction factor and mean velocity by applying the Least Squares version of the GCI method. The study shows mesh convergence, however, mesh independence is not reached with the selected grids. Applying a safety factor of $F_\mathrm{s} = 1.25$ gives an uncertainty in the friction factor of 37 % for the Smagorinsky model and 45 % for the WALE model. We note that the uncertainties are high and further grid refinement is required to obtain more accurate results. However, this is beyond the possibilities of this thesis due to high computational cost. Simulating two seconds of pipe flow on the finest mesh (h_1) takes approximately two days when running the simulation in parallel on 20 processors.

Overall, the mesh convergence study, as well as the simulation results, show that our LES model is working well but that the flow in under-resolved. We compare our LES results to DNS data from Wu and Moin [104] and experimental data from den Toonder and Nieuwstadt [17]. To summarize, the mean velocity profile is estimated reasonably well, the prediction of the shear stresses is excellent, and the general trend of the turbulent intensities is captured by the LES. Majority of the simulation results are typical for under-resolved LES. We do observe some inexplicable behaviour of the Smagorinsky model close to the pipe wall which we suspect is caused by the Van Driest damping function.

Numerical simulations are commonly a trade-off between accuracy and computational cost. The type of simulation (RANS, LES, DNS), with or without wall modeling, and level of grid refinement, all play a role. The high computational cost of the present LES, and accuracy of the simulation results, do raise the question whether RANS simulations may be more suitable to study mean velocity profiles in narrow stacks. Figure 4.17 shows the mean velocity profile obtained by a RANS simulation on a similar grid as the present LES. We observe that the mean axial velocity is over-estimated in the core region and under-estimated in the near wall region. The regions do not cancel, and the bulk velocity is over-predicted by approximately 2 %. In addition, we obtain a friction factor of the RANS flow of $f = 0.0394$. In Section 4.3, we discussed that the Blasius correlation predicts a friction factor of

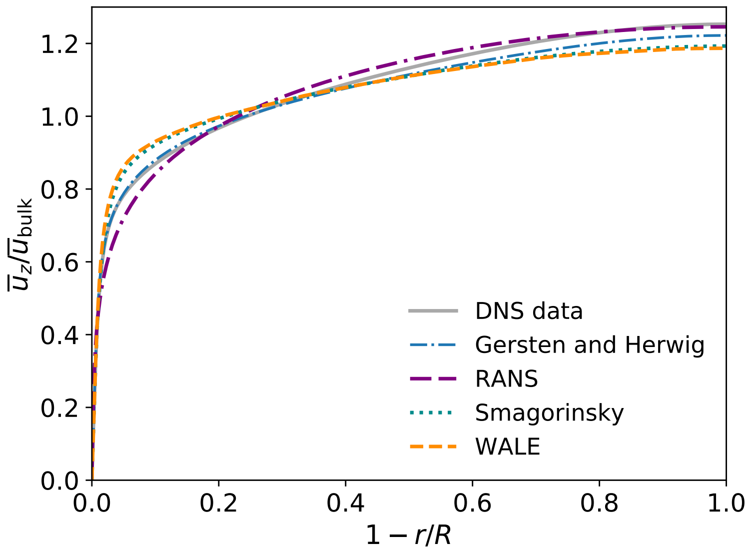

Figure 4.17: Mean velocity $\overline{u}_z/\overline{u}_{\mathrm{bulk}}$ as function of $1 - r/R$. Solid line: DNS data by Wu and Moin [104]; dash-dotted line: Gersten and Herwig profile [44]; dash-dash-dotted line: present RANS; dotted line: present LES with Smagorinsky subgrid-scale model; dashed line: present LES with WALE subgrid-scale model.

$f = 0.0218$, and the present LES with Smagorinsky model and WALE model give $f = 0.0207$ and $f = 0.0199$, respectively. The value from the RANS simulation is almost twice as large as the Blasius correlation. The results illustrate that RANS simulations are generally less accurate than LES. We require accurate results to provide a reliable estimate of measurement uncertainty, hence we prefer LES over RANS.

Chapter 5

Flow Characterization in the Near Wall Region

In this chapter, we study characteristics of the flow field around an S-type pitot tube in close proximity to the wall of a narrow exhaust stack. This numerical study gives insight in flow mechanisms in the near wall region, such as shear and wall proximity effects, see Section 3.2.1. Likewise the simulations in Chapter 4, we study gas flow in a pipe of diameter $D = 0.2\,\mathrm{m}$ and bulk velocity $\overline{\mathrm{u}}_{\mathrm{bulk}} = 3.333\,\mathrm{m/s}$. We aim to simulate the flow field for a measurement by an S-type pitot tube at wall-distance $y = 10\,\mathrm{mm}$, see Figure 5.1. The left image shows the dimensions of the S-type pitot tube used for measurements in Chapter 6. For the simulation, the geometry of the S-type pitot tube is simplified to a cylinder with a diameter of 6.6 mm and height of 14 mm, as is shown in the right image. We explain the simulation setup in Section 5.1, and discuss the simulation results in Section 5.2.

5.1 Simulation setup

A mesh of the simulation setup is created in Pointwise. The mesh of the pipe region obstructed by the cylinder is shown in Figure 5.2. The mesh upstream and downstream from the cylinder is a structured OH-grid similar to mesh h_1 in Chapter 4. A structured mesh is used to create a boundary layer around the cylinder (Figure 5.2a). The mesh around the boundary layer is divided into eight structured regions (Figure 5.2b). A part of the mesh is unstructured (Figure 5.2c) to match the grid

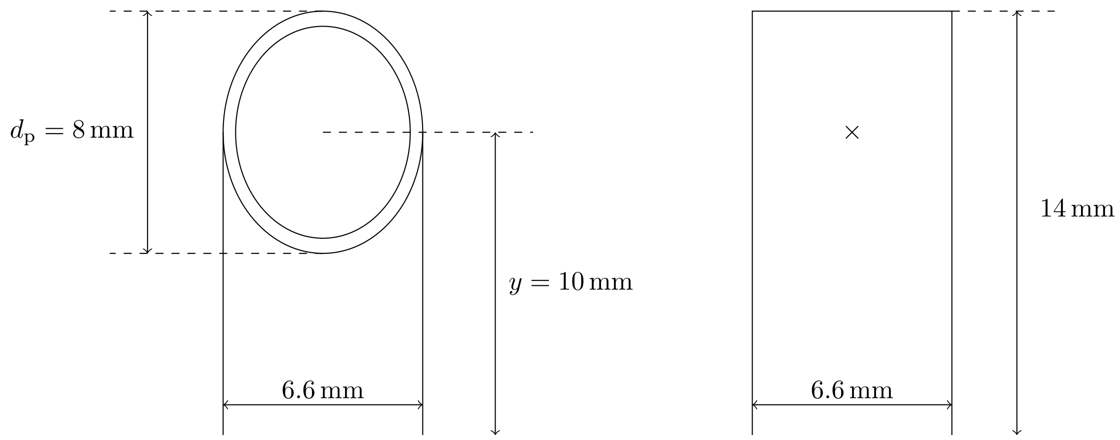

Figure 5.1: Sketch of the measurement setup (left) and simplified simulation setup (right).

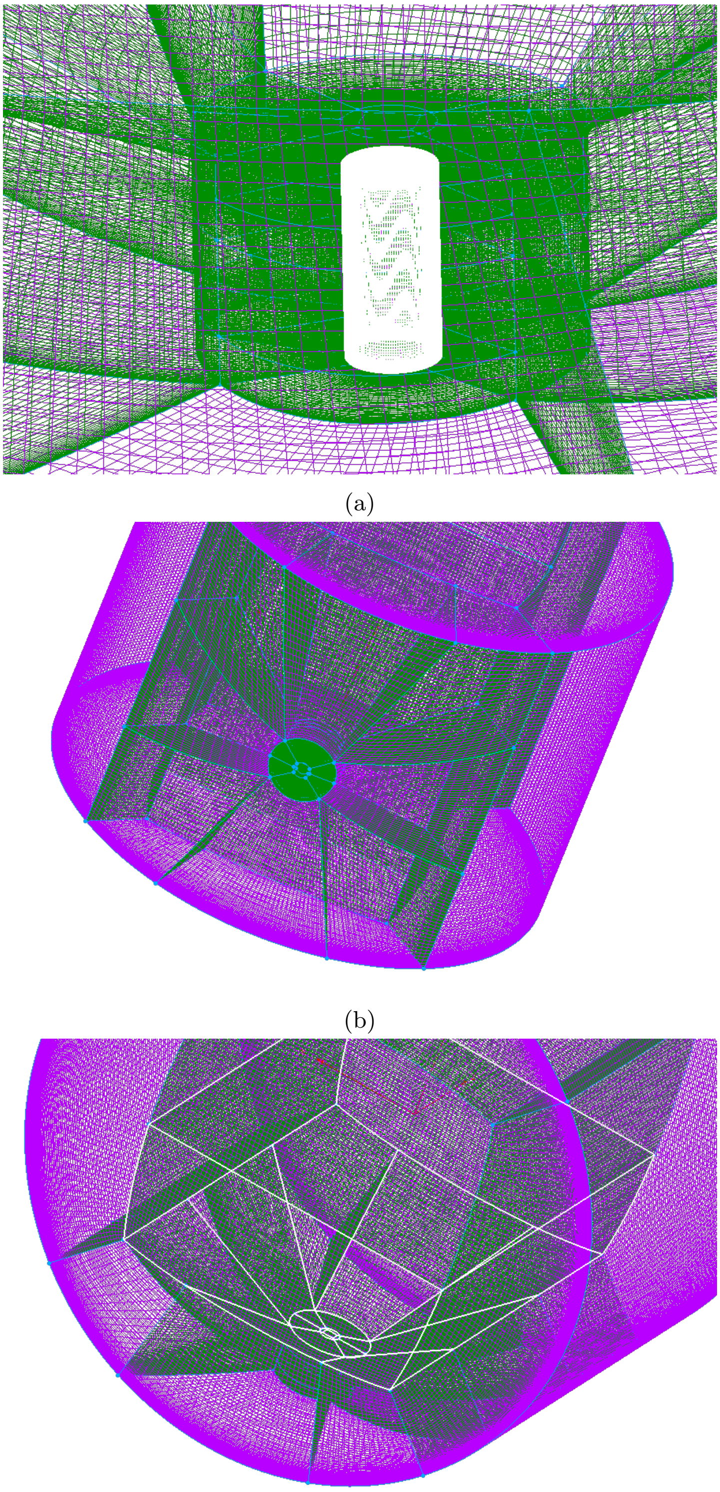

(a)

(b)

(c)

Figure 5.2: Mesh of the region of the pipe obstructed by the cylinder: (a) boundary layer around the cylinder (white); (b) the area around the cylinder is divided into eight structured regions; (c) unstructured region of the mesh.

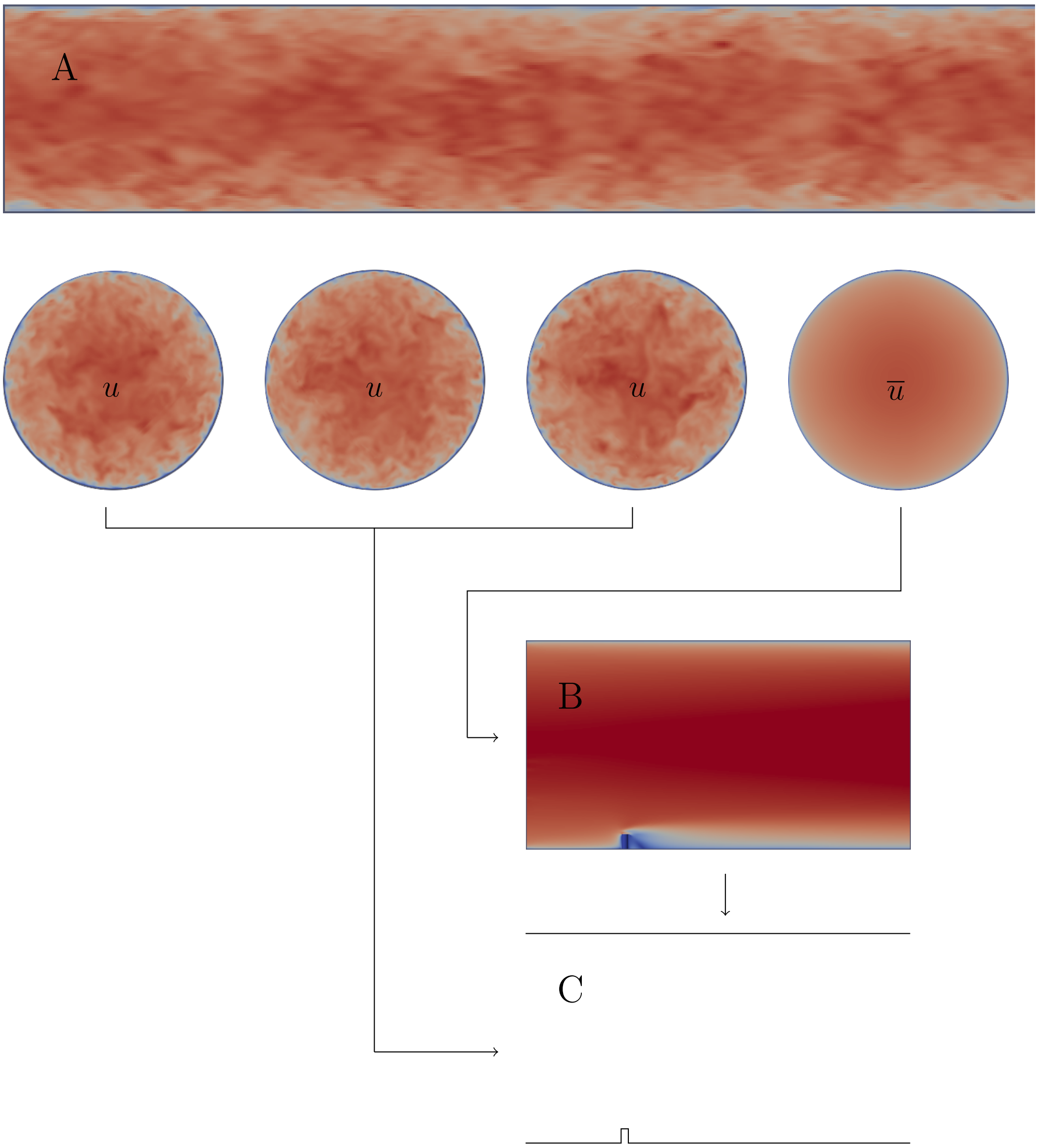

Figure 5.3: Schematic overview of the simulation setup for pipe flow obstructed by a cylinder.

refinement around the cylinder to the structured remainder of the mesh. Generally, LES is sensitive to mesh quality. Though the geometry of the S-type pitot tube is simplified to a cylinder, it is a challenge to create a mesh with a high cell orthogonality and low cell skewness.

Figure 5.3 gives an overview of three simulations:

(A) LES of fully developed turbulent pipe flow with periodic boundary conditions, see Chapter 4,

(B) RANS of pipe flow obstructed by a cylinder,

(C) LES of pipe flow obstructed by a cylinder.

Simulation (C) is of interest to this study, however, we require simulations (A) and (B) to generate inlet and initial conditions to simulation (C). In practice, S-type pitot tube measurements are performed in a section of the exhaust stack where fully developed flow conditions are expected. The fully developed inlet conditions to simulation (C) are obtained from simulation (A). Instantaneous velocity u is sampled over a constant z-plane at every time step Δt for a period T. The sampled profiles from simulation (A) are used as inlet boundary condition for every time step Δt of simulation (C). Note that simulation (C) is run for a similar period T as simulation (A). Simulation (C) is started from an initial flow field. The converged solution of RANS simulation (B) is used as initial flow field of simulation (C). The inlet boundary condition to simulation (B) is obtained by sampling mean velocity $\overline{u}$ over a constant z-plane of simulation (A).

Simulation (C) crashes before $t = 0.0001\,\mathrm{s}$ with either Smagorinsky subgrid-scale model, or WALE subgrid-scale model. We tried several adjustments to the original simulation:

- Addition of non-orthogonal correctors,
- Adjustment to the geometry of the cylinder to a round top,
- Different time steps,
- Different surface normal gradient schemes.

However, none of the adjustments provided the solution. Despite our effects, mesh quality may be insufficient for LES. The mesh was improved several times and does not exceed limits, such as maximum cell non-orthogonality, of the mesh quality check of OpenFOAM. In the next section, we discuss the flow field around the cylinder as predicted by RANS simulation (B).

5.2 Simulation results

We compare our RANS flow to the flow topology for a finite cylinder with ground plate from Frederich et al. [42]. Features of the flow field are shown in Figure 5.4. Frederich et al. [42] use LES to study flow with $\mathrm{Re_D} = 200,000$ around a cylinder with an aspect ratio (i.e. height divided by diameter) of 2. In comparison, we study RANS flow with $\mathrm{Re_D} = 44,000$ around a cylinder with an aspect ratio of ≈ 2.1. We use streamlines and isosurfaces of the $\mathcal{Q}$-criterion to visualize the flow field. The $\mathcal{Q}$-criterion defines vortices as the positive second invariant of the velocity gradient tensor [59]. $\mathcal{Q} > 0$ identifies regions where the vorticity magnitude prevails over the strain-rate magnitude. The pressure in the vortex region is required to be lower than the ambient pressure.

Figure 5.5 shows the axial velocity $\overline{u}_z$ for a constant y-plane at wall-distance $y = 10\,\mathrm{mm}$, and streamlines around the cylinder. We observe that the flow separates from the cylinder, and we notice a region of recirculation. The streamline at the side of the cylinder ($z = 0$) is shed into the recirculation zone. Figure 5.6 shows the isosurface of $\mathcal{Q} = 40,000$ and contours of velocity magnitude. Close to the pipe wall, we recognize a horse shoe vortex. Furthermore, we observe two vertical vortices downstream from the cylinder, however, they do not form an arch as is shown in Figure 5.4. Moreover, we observe a vortex downstream from the top of the cylinder. The flow does not distinguish two clear side vortices. Overall, the RANS flow displays some of the flow characteristics observed by Frederich et al. [42], however, not all of the characterisics are clearly observed. This could be caused by RANS modeling errors.

5.2.1 Numerical ‘calibration’

A close-up of the pressure field around the cylinder is shown in Figure 5.7. We observe a region of high pressure upstream from the cylinder due to the stagnation of incoming flow. Negative pressure is observed downstream from the cylinder since the flow is separated from the cylinder in this region. We sample the pressure upstream and downstream from the cylinder at $y = 10\,\mathrm{mm}$, see the locations marked × in Figures 5.1 and 5.7. Given mean axial velocity $\overline{u}_z$ at $y = 10\,\mathrm{mm}$ from the wall of the pipe, we can ‘calibrate’ the cylinder as if it were an S-type pitot tube. By rewriting (3.10), the calibration coefficient of the cylinder, denoted by K_c, is computed by

$$K_\mathrm{cyl} = \overline{u}_z \sqrt{\frac{\rho}{2\Delta p_\mathrm{cyl}}}, \tag{5.1}$$

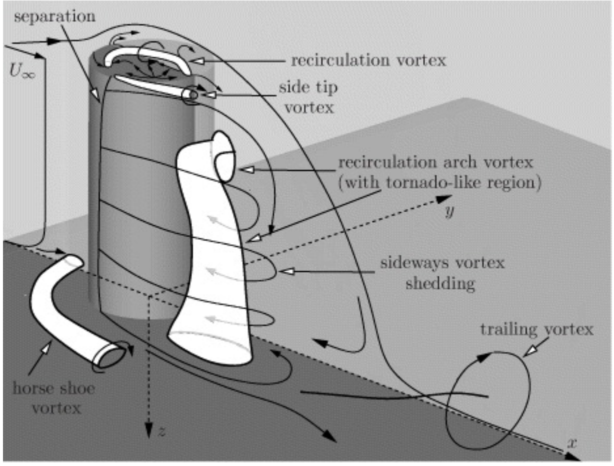

Figure 5.4: Flow topology for a finite cylinder with ground plate from Frederich et al. [42].

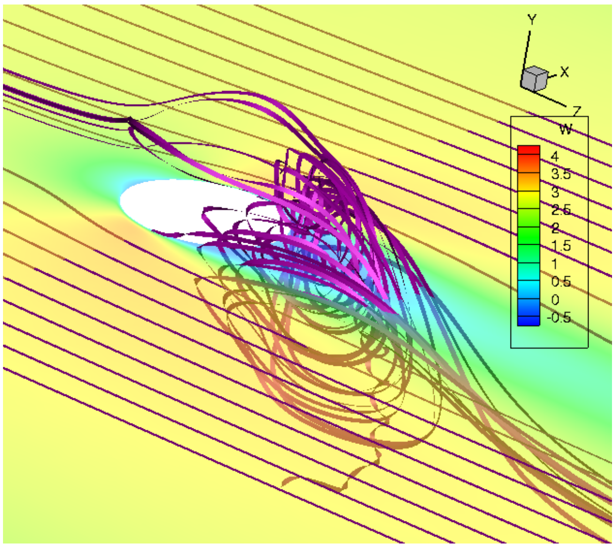

Figure 5.5: Axial flow velocity $\overline{u}_z$ at $y = 10\,\mathrm{mm}$ including streamlines.

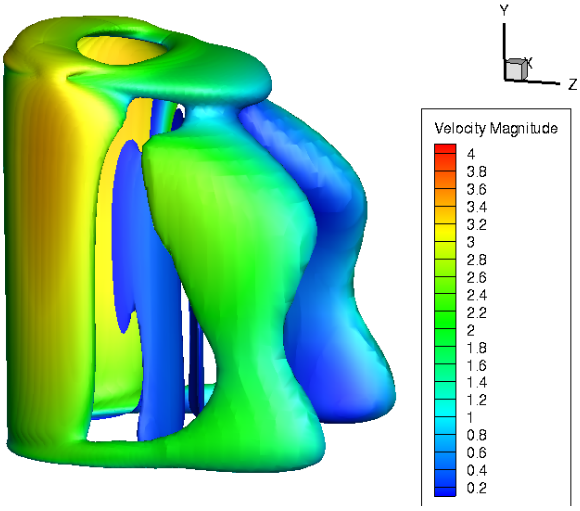

Figure 5.6: Isosurface of $\mathcal{Q} = 40,000$ and contours of the velocity magnitude.

Table 5.1: Estimation of calibration coefficient K_{cyl} from simulation.

	$\overline{u}_z$ [m/s]	K_{cyl} [−]
Smagorinsky model	3.10 ± 0.17	0.87 ± 0.05
WALE model	3.09 ± 0.04	0.87 ± 0.01

where the differential pressure across the cylinder at $y = 10\,\text{mm}$ is $\Delta p_{\text{cyl}} = 7.56\,\text{Pa}$, and $\rho = 1.205\,\text{kg/m}^3$. The cylinder is 'calibrated' against mean velocity $\overline{u}_z$ of the incoming fully developed turbulent flow field. Table 5.1 presents the mean axial velocity $\overline{u}_z$ of LES flow at $y = 10\,\text{mm}$ as predicted by simulations with the Smagorinsky subgrid-scale model and the WALE subgrid-scale model. Estimation of the numerical uncertainty of $\overline{u}_z$ is discussed in Section 4.3. By applying (5.1), calibration coefficient K_{cyl} is computed and presented in Table 5.1. Note that the uncertainty of calibration coefficient K_{cyl} is determined from uncertainty propagation of mean velocity $\overline{u}_z$ through (5.1), and does not include uncertainty associated with differential pressure Δp_{cyl}.

Notwithstanding the difference in geometry between a cylinder and S-type pitot tube, we observe that calibration coefficient K_{cyl} falls within the range of typical values for the calibration coefficient of S-type pitot tubes: 0.85 ± 0.05 [65]. Based on this simulation only, a cylinder seems to be a reasonable simplification of the geometry of an S-type pitot tube. This demonstrates the potential to use this and similar simulation setups for computational uncertainty quantification studies. For example, blockage is controlled by the relative size of the pitot tube to the sampling area. By considering pipe diameter or pitot tube width as uncertain input parameter, Monte Carlo methods or polynomial chaos methods can be used to estimate the uncertainty of S-type pitot tube measurements. We note that the numerical 'calibration' may be influenced by shear and wall proximity effects. A simulation of a cylinder in the pipe center, or of external flow around a cylinder, gives a more reliable indication of the error due to geometry approximation.

In Section 3.2.1, we discussed the impact of shear and wall proximity effects on pitot tube measurements. In short, previous research showed that pitot tube measurements in the boundary layer need to be corrected. Due to shear, streamlines are displaced towards a region of lower velocity, whereas wall proximity causes streamlines to be displaced away from the wall. Figure 5.8 shows the axial velocity field and streamlines around the cylinder. The streamlines suggest that the wall proximity effect is larger than the shear effect at $y = 10\,\text{mm}$. As a consequence, we measure a lower velocity at $y = 10\,\text{mm}$ than expected from the incoming fully developed turbulent flow field. The displacement of the streamline is estimated to be $\Delta y \approx 1\,\text{mm}$ from the fully developed inlet flow to the location of the impact orifice at $y = 10\,\text{mm}$. Assuming a displacement of $\Delta y = 1\,\text{mm}$, we measure $\overline{u}_z = 3.06\,\text{m/s}$ for the Smagorinsky model and $\overline{u}_z = 3.05\,\text{m/s}$ for the WALE model instead of the values in Table 5.1. This results in measurement errors of approximately $-1.2\,\%$ and $-1.3\,\%$ for the Smagorinsky model

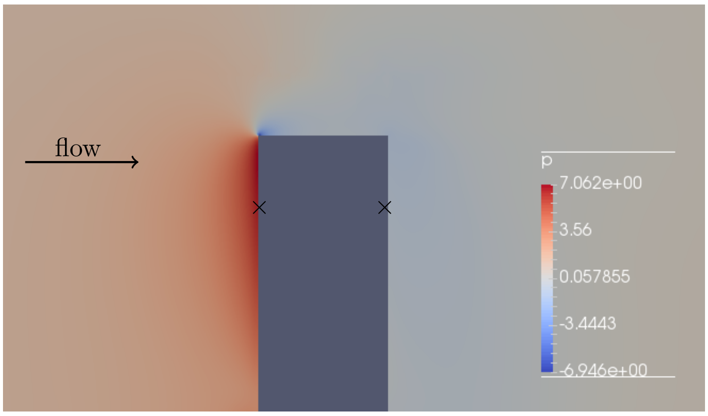

Figure 5.7: Pressure field around the cylinder.

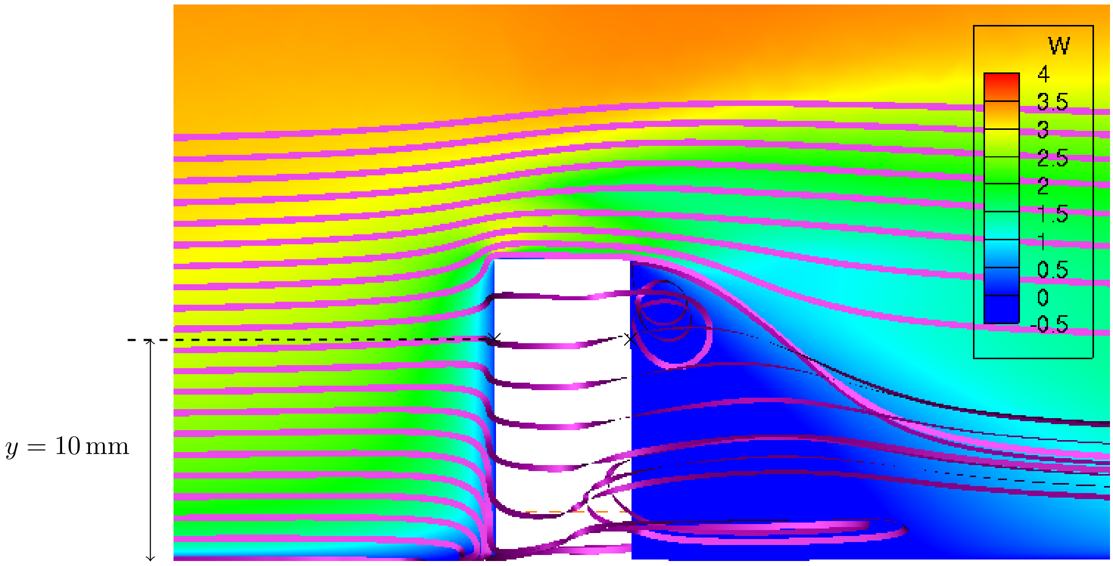

Figure 5.8: Axial velocity field and streamlines around the cylinder.

and WALE model, respectively. Computing (5.1) with mean axial velocity $\overline{u}_z$ at $y = 9\,\mathrm{mm}$ gives a calibration coefficient of $K_{\mathrm{cyl}} = 0.86$ for both the Smagorinsky model and WALE model.

5.3 Final remarks

In this chapter, we discussed numerical simulations of stack flow around an S-type pitot tube at $y = 10\,\mathrm{mm}$ from the wall. The results suggest that flow velocity is under-estimated by the S-type pitot tube in the near wall region. On one hand, we have confidence in our simulation results because the simulated calibration coefficient is within the range of typical values. On the other hand, the error due to geometry approximation of the S-type pitot tube may dominate over shear and wall proximity effects. In Chapter 6, we perform S-type pitot tube measurements at several wall-distances to study contributions of blockage, shear, and wall proximity effects to measurement uncertainty.

In previous studies, numerical simulations have proven to be valuable in determining experimental uncertainty of pipe flow measurements. Polynomial chaos methods have been applied in a number of studies, for example to determine the influence of uncertain inflow conditions on ultrasonic flow meter measurements [80, 100], or to study the reproducibility of swirling inflow conditions [95]. Similarly, uncertainty propagation methods can be used to study the uncertainty of S-type pitot tube measurements. Previous studies on the experimental uncertainty of pipe flow measurements have been performed with RANS. Uncertainty quantification methods such as Monte Carlo, and to a lesser extent polynomial chaos, require a large number of model evaluations. The high computational cost of LES limits the suitability of its application for uncertainty propagation methods. However, one can argue if the accuracy of RANS simulations is sufficient to determine a reliable estimate of measurement uncertainty.

Furthermore, previous studies have investigated measurement uncertainty of ultrasonic flow meters. Ultrasonic flow meters are non-intrusive to the pipe flow, whereas pitot tubes are intrusive. Using numerical methods in uncertainty propagation requires simulating the flow around the pitot tube. This study illustrates that creating a suitable mesh for LES is challenging. Geometry approximations, such as used in this chapter, affect the confidence that can be put into the simulation result. For future uncertainty propagation studies, we recommend to use RANS simulations and test the possibility to simulate the flow field around the exact geometry of an S-type pitot tube.

Chapter 6

S-Type Pitot Tube Measurements

We conduct S-type pitot tube measurements in the flow laboratory of VSL to study sources of uncertainty in emission measurements. In this chapter, we discuss calibration of an S-type pitot tube, and estimate measurement uncertainty by using sensitivity methods. We focus on several sources of measurement uncertainty such as misalignment, air leakage, blockage, shear and wall proximity. By performing measurements at several distances from the wall, we analyze the spatial variation of measurement uncertainty of local flow velocity. Based on the results, we recommend sampling locations for determining the volume flow rate in narrow stacks of medium-size combustion plants.

6.1 Experiment description

For the experiments, we use an S-type pitot tube with orifices of outer diameter $d_{\mathrm{p}} = 8\,\mathrm{mm}$ (Figure 6.1). Air velocity is measured in a pipe with a diameter $D = 0.2\,\mathrm{m}$. The pitot tube is traversed throughout the radius of the pipe with measurement positions spaced approximately logarithmically from the wall: at 4 mm, 6 mm, 10 mm, 16 mm, 25 mm, 40 mm, and 100 mm. Note that the traverse is initiated with the pitot tube in contact with the wall, and the final measurement is approximately at the pipe center. The measurement positions are determined using a laser and measuring tape. The head of the pitot tube is oriented with the stem marked '+' facing upstream. Figure 6.2b shows positioning of the pitot tube using the laser at 100 mm from the wall of the pipe.

The pitot tube measurements are conducted for steady state conditions of the air velocity. At each

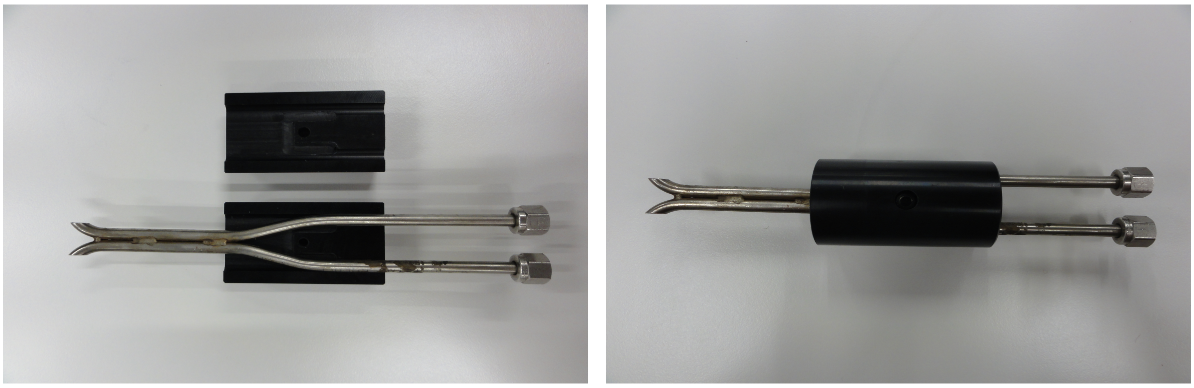

(a) (b)

Figure 6.1: S-type pitot tube used in the experiment.

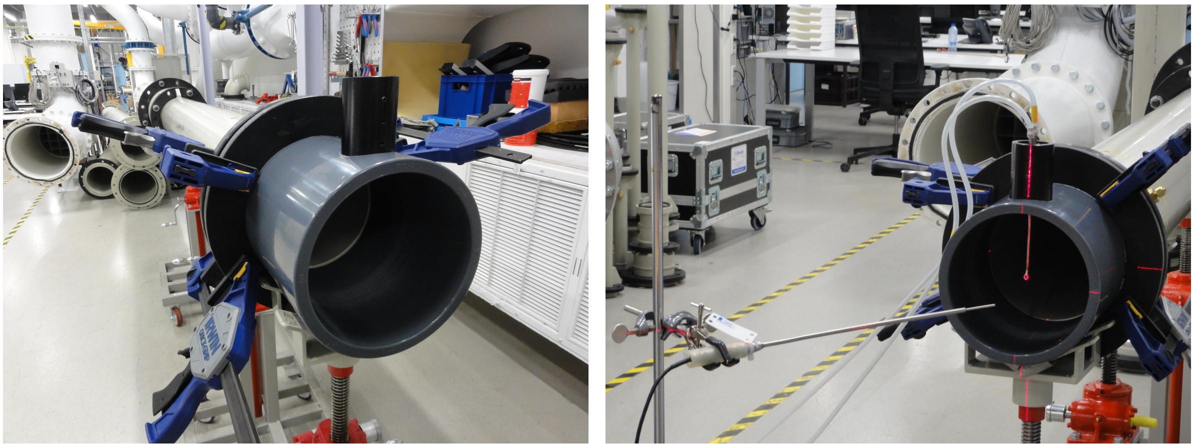

(a) (b)

Figure 6.2: Impression of the experimental setup.

position, the differential pressure across the pitot tube is measured for bulk velocities: 3.14 m/s, 4.83 m/s, 7.56 m/s, and 9.66 m/s. The bulk velocity follows from

$$\overline{u}_{\text{bulk}} = \frac{4Q}{\pi D^2}, \tag{6.1}$$

where volume flow rate Q is regulated by a blower. The differential pressure is derived from the average of three measurement series. Each measurement series consists of ten readings over a one-minute period. Overall, the experimental data is the average of 30 readings. Additionally, the air flow temperature and atmospheric pressure are monitored during the experiment. Figure 6.2b shows the temperature sensor downstream from the pipe exit.

As shown in Figure 6.2, the measurements are conducted in an extension to the pipes normally used in the flow laboratory. The PVC pipe extension is attached to the flange of the laboratory pipe with clamps. A packing of rubber is used between the flange and the pipe extension to prevent air leakage. The pipe extension has a diameter of $D = 201.5$ mm, whereas the diameter of the laboratory pipe is approximately $D = 199.5$ mm. This inconsistency is visible in Figure 6.4. A graphic representation of the measurement setup is shown in Figure 6.3. The pipe extension has a length of 232 mm, and the pitot tube is mounted 68 mm from the pipe exit. The laboratory pipe upstream from the extension has a length of 2.40 m. This pipe is proceeded by a pipe of diameter $D = 310$ mm. The flow is assumed

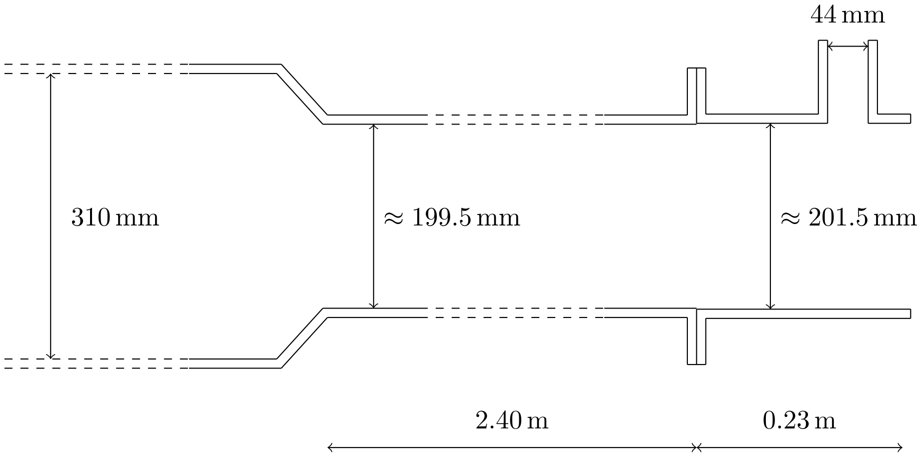

Figure 6.3: Sketch of the experimental setup.

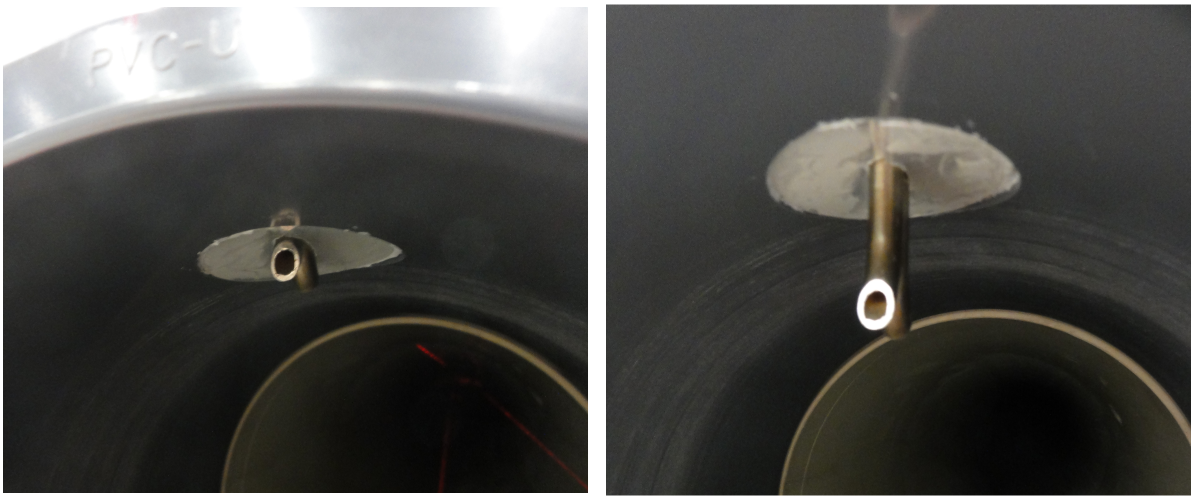

(a) $y = 4\,\mathrm{mm}$

(b) $y = 25\,\mathrm{mm}$

Figure 6.4: Positioning of the S-type pitot tube at two measurement points. The measurement port is closed off with putty and a plastic transparent cap.

to be fully developed at the location of the pitot tube. However, disturbances in the flow profile may be caused by differences in pipe diameter.

For the experiment, the pitot tube is locked in a cover as shown in Figure 6.1. The measurement position of the pitot tube from the wall of the pipe is adjusted by moving the cover up and down the sampling port. The sampling port ensures that the pitot tube has no pitch angle misalignment. The pitot tube is visually aligned perpendicular to the flow direction with an estimated uncertainty of $\pm 5^\circ$, and yaw angle misalignment may influence the measurements. The sampling port has a diameter $D = 44\,\mathrm{mm}$, and is closed off by the cover of the pitot tube. For the measurements at 100 mm, the cover closes off the measurement port at the wall of the pipe. For the measurements at other positions, the cover is located away from the wall. For these measurements, see Figure 6.4, the measurement port is closed off at the wall of the pipe with putty (Terostat-IV) and a plastic, transparent cap. This method may have caused flow disturbances at the wall, and perhaps air leakage.

6.2 Experimental uncertainty

This section concerns experimental uncertainty of the pipe flow measurements conducted in the flow laboratory. We apply sensitivity methods for the propagation of uncertainty of experimental observations. We discuss calibration of the S-type pitot tube, and determine the uncertainty of the calibration constant. Furthermore, we estimate the uncertainty of our experimental data. Standard EN ISO 16911-1 [49] sets a number of performance requirements for field measurements using differential pressure devices. We evaluate whether the uncertainty of our measurements meets the performance requirements.

6.2.1 Calibration of S-type pitot tube

The S-type pitot tube used in this experiment (Figure 6.1) has been calibrated by Young Calibration Limited in Shoreham-by-Sea, United Kingdom. During calibration, the pitot tube was mounted 140 mm from the end of a wind tunnel with the impact orifice perpendicular to the flow direction. The stem marked ‘+’ was oriented facing upstream. The instrument was calibrated by comparison

Table 6.1: Calibration data of S-type pitot tube measurements by Young Calibration Limited[a].

Actual $\overline{u}_z$ [m/s]	Standard $\overline{u}_z^*$ [m/s]	Actual Δp [Pa]	Standard Δp^* [Pa]	Actual ρ [kg/m^3]	Actual T [K]	K [−]
3.045	3.008	8.266	8.351	1.191	293.66	0.808
8.097	8.000	56.670	57.261	1.191	293.61	0.821
16.190	16.000	222.569	224.890	1.191	293.55	0.828

---

[a] Actual measurement data obtained by correspondence with Dr. Mark Hindle of Young Calibration Limited.

to a Laser Doppler Anemometer. The measurements were performed at steady state conditions of air velocity, and the differential pressure results were derived from the average of at least ten readings.

The issued calibration certificate states the value of calibration constant K under standard laboratory conditions of atmospheric pressure $p_{\text{atm}} = 101325\,\text{Pa}$, and temperature $T = 293.15\,\text{K}$. At these conditions, the air density is $\rho = 1.205\,\text{kg/m}^3$ as noted on the certificate. A copy of the calibration certificate is included in Appendix B. To determine calibration coefficient K, actual air velocity $\overline{u}_z$ and actual differential pressure Δp were referenced to standard laboratory conditions.

In the following derivation of the equation for calibration coefficient K, the parameters under standard laboratory conditions are denoted by superscript*. By rewriting (3.10), calibration coefficient K is computed by

$$K = \overline{u}_z^* \sqrt{\frac{\rho^*}{2\Delta p^*}}. \tag{6.2}$$

By applying conservation of mass flux over a constant area

$$\rho^* \overline{u}_z^* = \rho \overline{u}_z, \tag{6.3}$$

and the ideal gas law

$$\frac{\Delta p^*}{T^* \rho^*} = \frac{\Delta p}{T \rho}, \tag{6.4}$$

we can write (6.2) as

$$K = \overline{u}_z \frac{\rho}{\rho^*} \sqrt{\frac{T}{T^*}} \sqrt{\frac{\rho}{2\Delta p}}, \tag{6.5}$$

where $\rho^* = 1.205\,\text{kg/m}^3$ and $T^* = 293.15\,\text{K}$. The actual measurement results and the experimental data referenced to standard laboratory conditions are presented in Table 6.1.

The uncertainty of calibration coefficient K is not included on the calibration certificate, therefore an estimate of its uncertainty is determined using sensitivity methods outlined in Section 2.3.3. Mathematical model $\mathcal{F}$ is defined by (6.5), such that

$$K = \mathcal{F}\left(\overline{u}_z, \Delta p, \rho, T\right). \tag{6.6}$$

Table 6.2: Expanded uncertainty of measurement parameters for calibration of the pitot tube at Young Calibration Limited.

Parameter X_i	Notation	Expanded uncertainty $\mathbb{U}(X_i)$
Velocity	$\overline{u}_z$	$\pm 1.0\,\% + 0.1\,\text{m/s}$
Differential pressure	Δp	$\pm 0.2\,\% + 0.2\,\text{Pa} + (\Delta p$ Uncertainty$)$[a]
Density	ρ	$\pm 0.17\,\%$
Temperature[b]	T	$\pm 0.39\,\text{K}$

---

[a] See the calibration certificate for values of (Δp Uncertainty).

[b] Uncertainty of temperature obtained by correspondence with Dr. Mark Hindle of Young Calibration Limited.

Table 6.3: Uncertainty budget for calibration coefficient $K = 0.808$ at $\Delta p^* = 8.351\,\mathrm{Pa}$.

Parameter	Value	Relative expanded uncertainty	Coverage factor	Relative standard uncertainty	Sensitivity coefficient	Relative standard uncertainty
X_i	x_i	$\mathbb{U}(x_i)/x_i$	k	$\mathbb{u}(x_i)/x_i$	c_i	$\mathbb{u}_\mathbb{i}(y)/y$
$\overline{u}_z\,[\mathrm{m/s}]$	3.045	±4.28 %	2	±2.14 %	1	±2.14 %
$\Delta p\,[\mathrm{Pa}]$	8.266	±5.24 %	2	±2.62 %	-0.5	±1.31 %
$\rho\,[\mathrm{kg/m^3}]$	1.191	±0.17 %	2	±0.09 %	1.5	±0.13 %
$T\,[\mathrm{K}]$	293.66	±0.13 %	2	±0.07 %	0.5	±0.03 %
$K\,[-]$	0.808				$\mathbb{u}_\mathrm{c}(y)/y$ $\mathbb{U}_\mathrm{c}(y)/y$	±2.51 % ±5.03 %

The uncertainties of input parameters $\overline{u}_z$, Δp, ρ, and T to mathematical model $\mathcal{F}$ are used to determine the uncertainty of calibration coefficient K. Expanded uncertainties of the input parameters are presented in Table 6.2. The reported expanded uncertainties $\mathbb{U}(X_i)$ provide a coverage probability of approximately 95 %.

Mathematical model $\mathcal{F}$ is of the form

$$Y = aX_1^{q_1} X_2^{q_2} \dots X_i^{q_i} \dots X_n^{q_n}, \tag{6.7}$$

where a denotes a coefficient, and exponents q_i are known positive or negative numbers having negligible uncertainty. Following the GUM [50], relative standard uncertainty of the estimated measurement result $\mathbb{u}(y)/y$ can be evaluated by combining relative standard uncertainties of each input parameter $\mathbb{u}(x_i)/x_i$ and exponents q_i. The relative variance of estimated output y is then expressed by

$$\left[\frac{\mathbb{u}_\mathrm{c}(y)}{y}\right]^2 = \sum_{i=1}^{n} \left[q_i \frac{\mathbb{u}(x_i)}{x_i}\right]^2. \tag{6.8}$$

Note that (6.8) has the same form as (2.7).

Uncertainty of calibration coefficient K is determined with the aid of an uncertainty budget. The uncertainty analysis for estimated $K = 0.808$ at $\Delta p^* = 8.351\,\mathrm{Pa}$ (top row of Table 6.1) is presented by Table 6.3. The last column of the uncertainty budget shows that the uncertainty of mean velocity $\overline{u}_z$ is the largest contribution to the combined uncertainty of calibration coefficient K. In contrast, the uncertainty of temperature T is negligible to the resulting combined uncertainty.

The final result is rounded off following the rules for rounding in calibration of document EA/4-02 [30] of the European Cooperation for Accreditation:

- One significant value in the uncertainty (except 1, 2 or 3),
- Do not round down more than 5 %,
- Round off the measurement result to the same number of decimals as the uncertainty.

Table 6.4: Estimation and expanded uncertainty of calibration coefficient K.

Standard Δp^*	K	$\mathbb{U}(K)$
8.351 Pa	0.81	±0.04
57.261 Pa	0.82	±0.02
224.890 Pa	0.83	±0.01

This leads to expression of the final result by

$$K \in [0.81 \pm 0.04] .$$

An overview of the estimation and expanded uncertainty of calibration coefficient K is given in Table 6.4.

6.2.2 Uncertainty of S-type pitot tube measurements

Mean velocity $\overline{u}_z$ is determined from the differential pressure measured by the S-type pitot tube following (3.10). Furthermore, bulk velocity $\overline{u}_{\text{bulk}}$ of the pipe flow is computed by (6.1). The pitot tube is calibrated for standard laboratory conditions, see Section 6.2.1, therefore non-dimensional velocity $\overline{u}_z^*/\overline{u}_{\text{bulk}}^*$ is expressed by

$$\frac{\overline{u}_z^*}{\overline{u}_{\text{bulk}}^*} = K\sqrt{\frac{2\Delta p^*}{\rho^*}\frac{\pi D^2}{4Q^*}}, \tag{6.9}$$

where superscript* denotes a parameter under standard laboratory conditions. During experiments, the parameters listed in Table 6.5 were measured.

The measurement results for differential pressure Δp are referenced to standard laboratory conditions by applying the ideal gas law

$$\left.\begin{array}{l} \frac{\Delta p^*}{T^*\rho^*} = \frac{\Delta p}{T\rho} \\ \frac{p_{\text{atm}}^*}{T^*\rho^*} = \frac{p_{\text{atm}}}{T\rho} \end{array}\right\} \quad \frac{\Delta p^*}{\Delta p} = \frac{p_{\text{atm}}^*}{p_{\text{atm}}}, \tag{6.10}$$

where p_{atm} denotes the actual atmospheric pressure, and $p_{\text{atm}}^* = 101325\,\text{Pa}$ is the atmospheric pressure under standard laboratory conditions.

Volume flow rate Q is referenced to standard conditions by applying the continuity equation

$$\rho^* Q^* = \rho Q, \tag{6.11}$$

and the ideal gas law so that

$$\frac{Q}{Q^*} = \frac{\rho^*}{\rho} = \frac{p_{\text{atm}}^*}{p_{\text{atm}}}\frac{T}{T^*}, \tag{6.12}$$

where T denotes the temperature, and $T^* = 293.15\,\text{K}$ is the temperature under standard laboratory conditions.

Inserting (6.10) and (6.12) into (6.9), gives the following expression for velocity under standard laboratory conditions

$$\frac{\overline{u}_z^*}{\overline{u}_{\text{bulk}}^*} = K\frac{T}{T^*}\frac{p_{\text{atm}}^*}{p_{\text{atm}}}\sqrt{\frac{p_{\text{atm}}^*}{p_{\text{atm}}}}\sqrt{\frac{2\Delta p}{\rho^*}\frac{\pi D^2}{4Q}}. \tag{6.13}$$

Table 6.5: Expanded uncertainty of measurement input parameters for determining non-dimensional velocity $\overline{u}_z^*/\overline{u}_{\text{bulk}}^*$.

Parameter X_i	Notation	Uncertainty $\mathbb{U}(X_i)$
Volume flow rate	Q	$\pm 0.15\,\%$
Diameter pipe	D	$\pm 2\,\text{mm}$
Differential pressure	Δp	$\pm 1.2\,\text{Pa}$
Atmospheric pressure	p_{atm}	$\pm 3.4\,\text{Pa}$
Temperature	T	$\pm 0.08\,\text{K}$

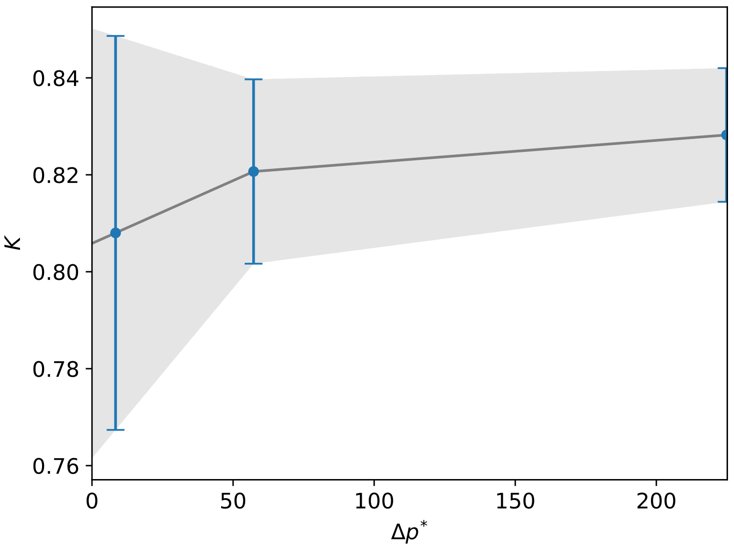

Figure 6.5: Calibration coefficient K as function of standard differential pressure Δp^* across the S-type pitot tube. Circle and error bar: calibration results and expanded uncertainty; solid line: linear interpolation of calibration results; shaded area: linear interpolation of expanded uncertainty of calibration results.

Mathematical model $\mathcal{F}$ is defined by (6.13) for estimation of the value and uncertainty of measurement output

$$\frac{\overline{u}_z^*}{\overline{u}_{\mathrm{bulk}}^*} = \mathcal{F}\left(K, T, p_{\mathrm{atm}}, \Delta p, D, Q\right). \tag{6.14}$$

The expanded uncertainties of actual measurement parameters are presented in Table 6.5. The expanded uncertainties are based on experience of the metrologists at VSL. The reported expanded uncertainties have a coverage probability of approximately 95 %.

By calibration, the value and uncertainty of calibration constant K is estimated at three standard differential pressures Δp^*, see Table 6.4. In this experiment, we determine the estimated value and uncertainty of calibration constant K by linear interpolation of the calibration results. Figure 6.5 shows a graph of calibration constant K as function of standard differential pressure Δp^*. Linear interpolation of the estimated value is indicated by the solid line, and expanded uncertainty of calibration coefficient K is shown by the shaded area.

The uncertainty of non-dimensional velocity $\overline{u}_z^*/\overline{u}_{\mathrm{bulk}}^*$ is determined with an uncertainty budget. Table 6.6 presents the uncertainty budget of a pitot tube measurement at $\overline{u}_{\mathrm{bulk}}^* = 3.14\,\mathrm{m/s}$ and $y = 40\,\mathrm{mm}$. We observe that the uncertainty of calibration coefficient K and differential pressure Δp are the largest contributions to the uncertainty of non-dimensional velocity $\overline{u}_z^*/\overline{u}_{\mathrm{bulk}}^*$. Following the rules for rounding, the final result is

$$\frac{\overline{u}_z^*}{\overline{u}_{\mathrm{bulk}}^*} \in [1.02 \pm 0.09]$$

An overview of all measurement results and expanded uncertainties are included in Appendix C.

In addition to the uncertainty of non-dimensional velocity $\overline{u}_z^*/\overline{u}_{\mathrm{bulk}}^*$, the experimental results also have uncertainty in distance y of the pitot tube from the wall of the pipe. The expanded uncertainty of the wall distance is estimated by ±3 mm.

Table 6.6: Uncertainty budget for non-dimensional velocity $\overline{u}_z^*/\overline{u}_{\mathrm{bulk}}^*$ at $\overline{u}_{\mathrm{bulk}}^* = 3.14\,\mathrm{m/s}$ and $y = 40\,\mathrm{mm}$.

Parameter	Value	Relative expanded uncertainty	Coverage factor	Relative standard uncertainty	Sensitivity coefficient	Relative standard uncertainty
X_i	x_i	$\mathbb{U}(x_i)/x_i$	k	$\mathbb{u}(x_i)/x_i$	c_i	$\mathbb{u}_\mathbb{i}(y)/y$
$K\,[-]$	0.808	±4.97 %	2	±2.48 %	1	±2.48 %
$\Delta p\,[\mathrm{Pa}]$	9.352	±12.83 %	2	±6.42 %	0.5	±3.21 %
$p_{\mathrm{atm}}\,[\mathrm{Pa}]$	100518	±0.003 %	2	±0.002 %	-1.5	±0.001 %
$Q\,[\mathrm{m}^3/\mathrm{s}]$	0.1010	±0.15 %	2	±0.08 %	-1	±0.08 %
$D\,[\mathrm{mm}]$	201.5	±0.99 %	2	±0.50 %	2	±0.99 %
$T\,[\mathrm{K}]$	292.94	±0.027 %	2	±0.014 %	1	±0.014 %
$\overline{u}_z^*/\overline{u}_{\mathrm{bulk}}^*\,[-]$	1.017				$\mathbb{u}_\mathrm{c}(y)/y$	±4.18 %
					$\mathbb{U}_\mathrm{c}(y)/y$	±8.36 %

6.2.3 Performance requirements during field measurements

Standard EN ISO 16911-1 [49] sets a number of performance requirements for field measurements using differential pressure devices. A summary of performance requirements relevant to our experimental study is given in Table 6.7. Note that the requirements concern standard uncertainty of the considered parameters. In this section, we discuss whether our experimental observations meet the performance requirements in standard EN ISO 16911-1 [49].

As previously discussed in Section 6.1, the pitch angle of the pitot tube is negligible, and we estimate an uncertainty of yaw angle of ±5°. Hence, positioning of the pitot tube relative to the flow direction fulfills the performance requirements. In addition, the experimental study meets the performance requirements for stack internal diameter. The standard uncertainty of diameter D is $\pm 0.5\,\%$, see Table 6.6. This is well within the permissible criterion of $< 2\,\%$.

In contrast, calibration of the S-type pitot tube does not meet the performance requirements for majority of the measurements. We observe that standard uncertainty of calibration coefficient K varies from $\pm 3\,\%$ for $\Delta p = 4\,\mathrm{Pa}$ to $\pm 1\,\%$ for $\Delta p = 114\,\mathrm{Pa}$, see Appendix C. Calibration of the S-type pitot tube is insufficiently accurate for this experimental study according to standard EN ISO 16911-1 [49]. From the uncertainty budget (Table 6.3), we observe that uncertainty of calibration constant K can be reduced through more accurately controlled calibration with reduced uncertainty in mean velocity $\overline{u}_z$ and differential pressure Δp.

Additionally, uncertainty of the differential pressure reading device does not meet the performance requirements. The standard uncertainty of differential pressure Δp is $\pm 0.6\,\mathrm{Pa}$ (Table 6.5). To meet the performance requirements in standard EN ISO 16911-1 [49], the differential pressure across the S-type pitot tube should be larger than $60\,\mathrm{Pa}$. This is true for only four of the measurements, see Appendix C.

Table 6.7: Performance requirements during field measurements from EN ISO 16911-1 [49].

Parameter	Criterion
Angle of pitot to flow (yaw)	$< 15°$
Angle of pitot to measurement plane (pitch)	$\leq 10°$
Stack internal diameter	$< 2\,\%$ of value
Uncertainty in pitot calibration	$\leq 1\,\%$ of value
Uncertainty in differential pressure reading device	$\leq 1\,\%$ of value

Measurement performance in narrow stacks is restricted by large uncertainty in the differential pressure reading device. In general, bulk velocities in narrow exhaust stacks vary between 2 m/s and 10 m/s. The differential pressure across an S-type pitot tube is small at these low flow velocities. Differential pressure reading devices have a high relative uncertainty for low measurement values. This effects not only the field measurements but also calibration. Its high uncertainty is propagated through the mathematical model of calibration and contributes to a high uncertainty of calibration coefficient K.

The present experimental study illustrates that the performance requirements in standard EN ISO 16911-1 [49] may not be achievable for field measurements in narrow stacks. We suggest a measurement campaign to assess the performance of S-type pitot tube measurements in narrow stacks. Further research will show if the performance requirements in standard EN ISO 16911-1 [49] are realistic for measurements in narrow stacks or have to be adjusted.

6.3 Experimental Results

In this section, the results of the S-type pitot tube measurements are presented. The experimental data is referenced to standard laboratory conditions as discussed in Section 6.2.2. Whereas parameters at standard laboratory conditions are denoted by superscript* in Section 6.2.2, the superscript notation is omitted in this section. The uncertainties of measured parameters (Table 6.5) and calibration are included in the uncertainty of the presented measurands. Reference LES data of undisturbed pipe flow is obtained with the Smagorinsky sub-grid scale model and a mesh of approximately 4.9 million cells (h_1), see Chapter 4 for further details.

Figure 6.6 shows the mean velocity measured with the S-type pitot tube at several distances from the wall of the pipe. Note that no correction for blockage is required since mean velocity $\overline{u}_z$, as well as bulk velocity $\overline{u}_{\text{bulk}}$, are affected by blockage. The vertical error bars show the uncertainty of the velocity measurements, and the horizontal error bars show the uncertainty of the positions of the pitot tube. The experimental data is compared to the reference Gersten and Herwig profile [44] and LES data of undisturbed pipe flow. At the pipe center, the measurement results are consistent with the reference profile and LES data. In contrast, the experimental observations in the near wall region are inconsistent with the reference profile and LES data. Mean velocity $\overline{u}_z$ is underestimated in the near wall region.

By considering the reference Gersten and Herwig profile [44] as true value of the mean velocity, the relative error of the pitot tube measurements is computed, and presented in Figure 6.7. The error bars are not included in this graph for clarity of the figure. The graph shows that the relative experimental error is approximately ±2 % in the pipe center and approximately −20 % close to the wall. Overall, the results suggest that the relative error is independent of bulk velocity $\overline{u}_{\text{bulk}}$.

Note that the absolute error of the measurements at $1-r/R = 0.04$ and $1-r/R = 0.06$ are significantly lower for $\overline{u}_{\text{bulk}} = 3.14\,\text{m/s}$ than for other bulk velocities. The differential pressure across the S-type pitot tube of these measurements is $\Delta p = 3.88\,\text{Pa}$ and $\Delta p = 4.44\,\text{Pa}$, respectively. These values are lower than the requirement $\Delta p > 5\,\text{Pa}$ in standard EN 15259 [39]. Surprisingly, this results in a lower absolute error than the errors of other experimental observations at these locations that do fulfill the requirement.

Prior to discussing blockage, shear, and wall proximity effects, other sources of measurement error are considered. One of the sources for measurement error may be misalignment of the pitot tube with flow direction. Including a correction for yaw angle β of the pitot tube in (3.10), following the practice of Bryant et al. [10], gives

$$\overline{u}_z = K\cos\left(\beta\right)\sqrt{\frac{2\Delta p}{\rho}}. \tag{6.15}$$

Note the similarity of correction factor $\cos(\beta)$ for yaw in (6.15), and the correction factor $\cos(\alpha)$ for swirl in (3.5). Both factors compensate for the orifices of the pitot tube not being aligned perpendicular to the direction of the flow. As mentioned in Section 6.1, we estimate an uncertainty of yaw angle β of

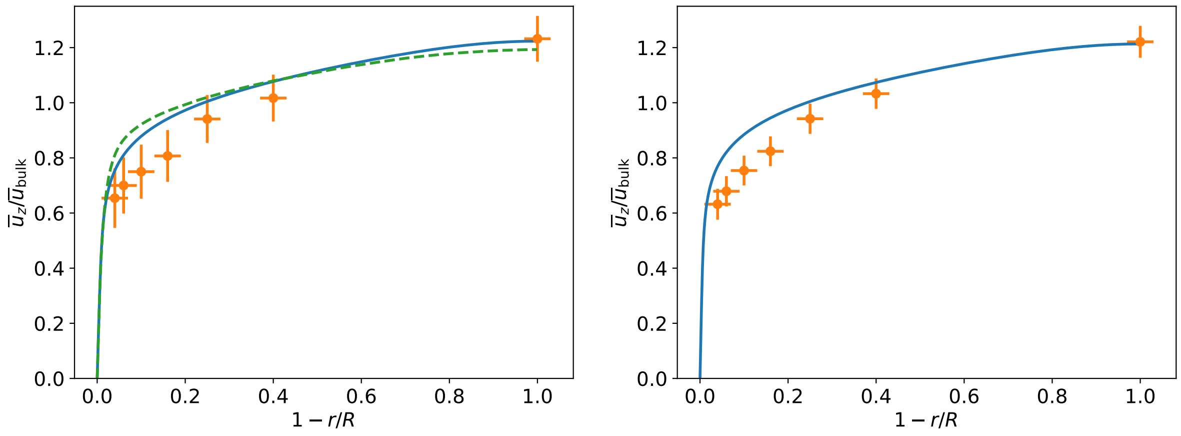

(a) $\overline{u}_{\text{bulk}} = 3.14\,\text{m/s}$

(b) $\overline{u}_{\text{bulk}} = 4.83\,\text{m/s}$

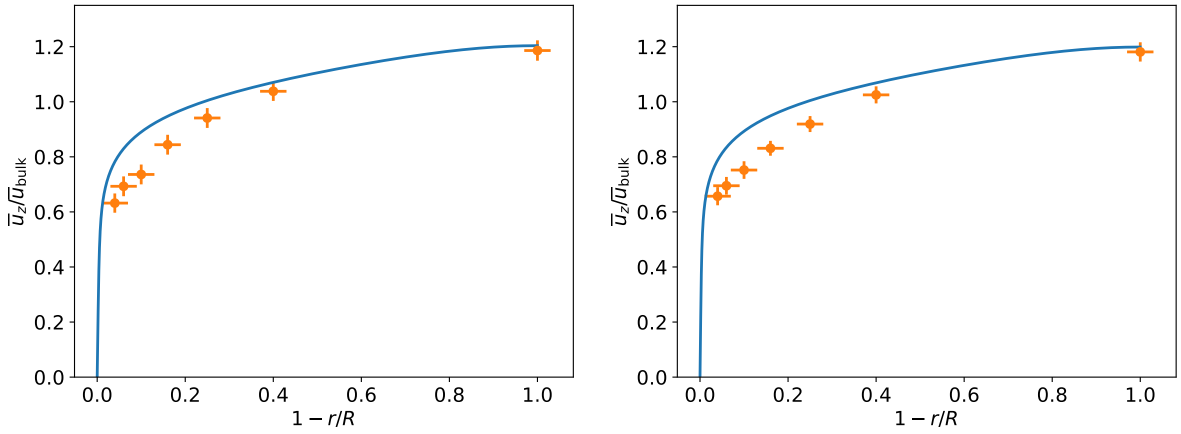

(c) $\overline{u}_{\text{bulk}} = 7.56\,\text{m/s}$

(d) $\overline{u}_{\text{bulk}} = 9.66\,\text{m/s}$

Figure 6.6: Mean velocity $\overline{u}_z/\overline{u}_{\text{bulk}}$ as function of $1 - r/R$. Circle: S-type pitot tube measurements; solid line: Gersten and Herwig reference profile [44]; dashed line: LES for $\overline{u}_{\text{bulk}} = 3.333\,\text{m/s}$.

±5°. Assuming estimated maximum yaw angle $\beta = 5°$, results in an estimated error of the measured velocity $\overline{u}_z$ of $-1\,\%$. Moreover, the pitot tube measurements may be affected by air leakage at the sampling port or further upstream in the pipe. We make a conservative estimate of a possible leak by assuming a hole with a radius of 1 cm in the pipe configuration. This results in an estimated loss of volume flow rate Q of $-1\,\%$.

Finally, increased wall roughness at the sampling port may have influenced the mean velocity profile, see Figure 3.3. We observe lower mean velocities at the pipe wall consistent with increased wall roughness, however, the mean velocity at the pipe center is not higher. This suggests that the mean velocity profile is not altered due to increased wall roughness. We conclude that the measurement errors shown in Figure 6.7 may partly be caused by misalignment of the pitot tube and air leakage in the pipe configuration. However, considering the large measurement error in the near wall region, shear and wall proximity effects are expected to dominate over other sources of measurement error. The influence of blockage, shear, and wall proximity effects are discussed in the subsequent sections.

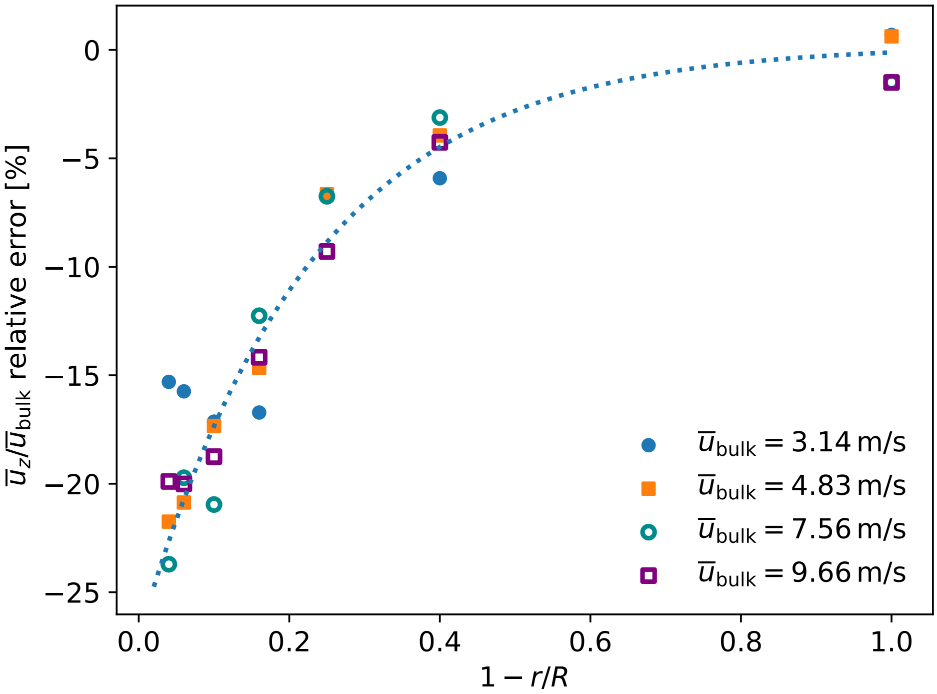

Figure 6.7: Relative error [%] of mean velocity $\overline{u}_z/\overline{u}_{\mathrm{bulk}}$ as function of $1 - r/R$. Full circle: $\overline{u}_{\mathrm{bulk}} = 3.14\,\mathrm{m/s}$; full square: $\overline{u}_{\mathrm{bulk}} = 4.83\,\mathrm{m/s}$; open circle: $\overline{u}_{\mathrm{bulk}} = 7.56\,\mathrm{m/s}$; open square: $\overline{u}_{\mathrm{bulk}} = 9.66\,\mathrm{m/s}$; dotted line: exponential fit.

6.3.1 Blockage

The impact of blockage on measurement uncertainty is studied by pitot tube measurements at the pipe center. At this location, no impact of shear or wall proximity effects are expected to influence the measurement result. As discussed in Section 3.1, the pitot tube should not obstruct more than 5 % of the measurement plane according to standard EN ISO 16911-1 [49]. The area of the pipe is $A = 0.0318\,\mathrm{m}^2$, and the frontal area of the pitot tube is $A_{\mathrm{pitot}} = 0.0006\,\mathrm{m}^2$ when positioned at the pipe center. This results in a blockage of approximately 2 % of the measurement plane by the pitot tube, which is well within the requirements in standard EN ISO 16911-1 [49].

Applying a correction for blockage (3.13) to the mean velocity measurements at the pipe center results in a reduction of −2 %. Table 6.8 shows the corrected (denoted by superscript′) and uncorrected results of mean velocity measurements at the pipe center, and the mean velocity of the reference Gersten and Herwig profile [44] denoted by $\overline{u}_{z,\mathrm{ref}}$. The effectiveness of blockage correction cannot

Table 6.8: Blockage correction of S-type pitot tube measurement at the pipe center.

Bulk velocity $\overline{u}_{\mathrm{bulk}}$ [m/s]	Gersten and Herwig [44] $\overline{u}_{z,\mathrm{ref}}$ [m/s]	Uncorrected velocity $\overline{u}_z$ [m/s]	Corrected velocity $\overline{u}'_z$ [m/s]
3.14	3.85	$3.87 \pm 6.4\,\%$	$3.80 \pm 7.6\,\%$
4.75	5.76	$5.80 \pm 4.3\,\%$	$5.69 \pm 5.8\,\%$
7.56	9.10	$8.97 \pm 2.4\,\%$	$8.80 \pm 4.7\,\%$
9.67	11.59	$11.42 \pm 2.2\,\%$	$11.20 \pm 4.5\,\%$

be evaluated with the present experiment since the absolute correction is smaller than the range of measurement uncertainty. The evaluation of blockage correction will require that the uncertainty of the measurements is reduced by more carefully controlled experiments.

6.3.2 Shear and wall proximity effects

It is known that certain corrections are needed to obtain accurate velocity measurements in the boundary layer using pitot tubes [69]. Only corrections for L-type pitot tubes have been developed to date, see Section 3.2.1. We apply the corrections for L-type pitot tubes developed by MacMillan [68] to the measurement results of the S-type pitot tube. Figure 6.8 shows the corrected measurement results for $\overline{u}_{\text{bulk}} = 4.83\,\text{m/s}$. The correction for shear displaces the measurement result towards the center of the pipe, whereas the correction for wall proximity increases the mean velocity result. We observe that the corrections are smaller than the estimated measurement error.

Though shear and wall proximity effects are expected to affect S-type pitot tube measurements in the boundary layer, the present experimental study shows that the corrections developed for L-type pitot tubes do not suffice for S-type pitot tube measurements. This suggests that S-type pitot tube measurements are more strongly influenced by shear and wall proximity effects than L-type pitot tube measurements. This may be expected since the L-type pitot tube is a finer instrument than the S-type pitot tube.

Figure 6.7 includes an exponential fit of the relative measurement error (excluding measurements of $\Delta p < 5\,\text{Pa}$) as function of distance from the wall. The relative error reduces from approximately $-25\,\%$ near the wall to $0\,\%$ in the pipe center. For further research, the measurement error may be investigated for different field measurements conditions in narrow exhaust stacks, such as stack diameters, bulk velocities, orifice sizes, among others. Comparison of resulting exponential fits of measurement error data may form the basis for development of corrections for shear and wall proximity effects for S-type pitot tube measurements.

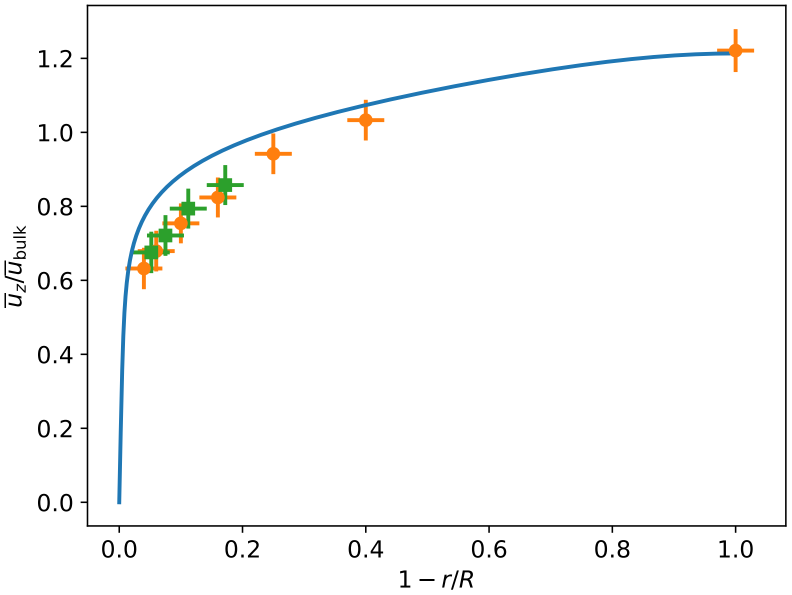

Figure 6.8: Mean velocity $\overline{u}_z/\overline{u}_{\text{bulk}}$ as function of $1 - r/R$ ($\overline{u}_{\text{bulk}} = 4.83\,\text{m/s}$). Circle: S-type pitot tube measurements; diamond: S-type pitot tube measurements corrected for shear and wall proximity following MacMillan [68]; solid line: Gersten and Herwig profile [44].

6.4 Final remarks

In this chapter, we discussed the experimental results of S-type pitot tube measurements at several distances from the wall of a narrow stack (i.e. pipe). The present experimental study does not meet the performance requirements in standard EN ISO 16911-1 [49]. The high uncertainty of differential pressure reading devices contribute to high measurement uncertainty in narrow stacks. Further research is needed to investigate if performance requirements in standard EN ISO 16911-1 [49] are achievable for measurements in narrow stacks with characteristic bulk velocities up to 10 m/s.

We observed high measurement errors close to the wall. The present study suggests that shear and wall proximity effects dominate over other sources of measurement error in the this region. Further research is needed to develop corrections for shear and wall proximity effects by S-type pitot tube measurements in the near wall region. In further research, different boundary conditions such as other S-type pitot tube dimensions, stack diameters, bulk velocities, among others, can be be investigated.

In the present experimental study, we observe the smallest measurement error and uncertainty in the center of the pipe. For field measurements, we recommend to measure the mean velocity at the center of narrow exhaust stacks, and apply a correction factor F to approximate bulk velocity $\overline{u}_{\text{bulk}}$, such that

$$\overline{u}_{\text{bulk}} \approx F\,\overline{u}_z|_{r=0}. \tag{6.16}$$

We expect this method to have the smallest possible measurement error and uncertainty. Furthermore, this method is less time-consuming than conducting multiple measurements across a sampling plane. Further research is required to determine a suitable value for correction factor F. Based on the reference Gersten and Herwig profile [44]: $F \approx 0.82$.

Fully developed flow conditions are required for the proposed measurement method (6.16). We note that the location of maximum mean velocity is shifted in swirling flows. Consequently, the proposed measurement method will under-estimate the volume flow rate in case of swirl. Furthermore, mean velocity $\overline{u}_z$ may need to be corrected for blockage. The uncertainty of the present experimental results in this chapter are, however, too high to evaluate the effectiveness of blockage correction.

Chapter 7

Conclusion and Recommendations

In support of recent EU regulations for emissions from medium-size combustion plants, we investigated the uncertainty of flow measurements by S-type pitot tubes in narrow exhaust stacks. Current Standard Reference Methods (SRM) for measurement of volume flow rates within exhaust stacks, EN ISO 16911 [49] and EN 15259 [39], have been developed and validated for measurements within exhaust stacks of large-size combustion plants. We use numerical simulations and experiments to characterize the flow field and investigate the impact of blockage and wall effects on measurement uncertainty. Accurate measurement of emissions is key to effective control and reduction of air pollution. The results of this thesis contribute to the development of standardized measurement methods for mass emissions from medium-size combustion plants.

S-type pitot tube measurements are conducted in a section of the exhaust stack where homogeneous flow conditions can be expected. We use Large Eddy Simulation (LES) to model fully developed turbulent flow at Reynolds number $\mathrm{Re_D} = 44,000$ in a pipe of diameter $D = 0.2\,\mathrm{m}$. We investigate two subgrid-scale models: the Smagorinsky model and the WALE model. Numerical uncertainty of the LES flow is determined with the Least Squares version of the GCI method. Our results show that uncertainty of the friction factor on the finest mesh is approximately $40\,\%$. Furthermore, the uncertainty of the mean velocity on the finest mesh reaches $11\,\%$. The LES flow is under-resolved, however, further grid refinement is beyond current engineering possibilities due to high computational cost.

We validate our LES results on the finest mesh with DNS data by Wu and Moin [104] and experimental data by den Toonder and Nieuwstadt [17] of fully developed turbulent pipe flow. In short, the mean velocity profile is estimated reasonably well, the prediction of the shear stresses is excellent, and the general trend of the turbulent intensities is captured by the LES. The majority of our results are typical for under-resolved LES flow. As expected, the impact of the choice of subgrid-scale model decreases with grid refinement, and the differences between the Smagorinsky model and WALE model are negligible on the finest mesh. We do observe inexplicable behaviour in the near wall region for the Smagorinsky subgrid-scale model, which we suspect is caused by Van Driest damping.

We use the results of fully developed turbulent flow as inlet condition to a pipe flow simulation obstructed by an S-type pitot tube. We simulate the flow field for a measurement at wall-distance $y = 10\,\mathrm{mm}$. Despite simplifying the geometry of an S-type pitot tube to a cylinder, the LES crashes. As alternative, we study a RANS simulation of fully developed turbulent pipe flow obstructed by a cylinder. We observe some characteristic flow structures downstream from the cylinder. The streamlines suggest that S-type pitot tube measurements under-estimate the flow velocity in the near wall region. We estimate an error of approximately $-1.2\,\%$ for flow velocity measurements at wall-distance $y = 10\,\mathrm{mm}$. We note that the error by geometry approximation may dominate the shear and wall proximity effects.

Numerical 'calibration' of the cylinder in our simulations gives typical values for the calibration coefficient of an S-type pitot tube. This suggests that our simulation setup is suitable for future uncertainty propagation studies. Monte Carlo methods and polynomial chaos methods may be used to study the impact of uncertainty sources such as swirl and blockage on S-type pitot tube measurements within narrow exhaust stacks. This study illustrates that current LES is computational expensive and sensitive to mesh quality. For the large number of model evaluations required for uncertainty propagation studies, we recommend to use RANS. We suggest to try simulating the flow around the exact geometry of an S-type pitot tube to reduce error by geometry approximation.

We conduct S-type pitot tube measurements at bulk velocities up to $\overline{u}_{\text{bulk}} = 10\,\text{m/s}$ in the flow laboratory of VSL. We measure the flow velocity at several distances from the wall of a pipe of diameter $D = 0.2\,\text{m}$. Calibration uncertainty and experimental uncertainty are determined with sensitivity methods. Uncertainty of the velocity measurements ranges from $\pm 3\,\%$ to $\pm 17\,\%$. The largest contributions to the uncertainty are calibration of the S-type pitot tube, and the differential pressure reading device. The latter has a high measurement uncertainty for low flow velocities typical in narrow exhaust stacks. The S-type pitot tube measurements do not meet all the performance criteria for field measurements in standard EN ISO 16911 [49]. We suggest a measurement campaign to investigate realistic performance requirements for differential pressure measurements in narrow exhaust stacks.

By considering the reference Gersten and Herwig profile [44] as true value of the mean velocity, we compute the error of the S-type pitot tube measurements. We observe that the relative measurement error decreases from approximately $-25\,\%$ near the wall to roughly $0\,\%$ in the center of the pipe, and is independent of bulk velocity. At wall-distance $y = 10\,\text{mm}$, the estimated error is approximately $-17\,\%$, which is much larger than the estimated error of $-1.2\,\%$ by the RANS simulation. We estimate that misalignment of the S-type pitot tube and air leakage may have contributed to the measurement error by roughly $-1\,\%$ each. Our results suggest that shear and wall proximity effects dominate over other sources of measurement error in the near wall region. Further experimental studies are required to investigate if the exponential fit through the measurement error data is also observed under different conditions, such other S-type pitot tubes, exhaust stack diameters, flow laboratories, among others. The uncertainty of the present experimental results is too large to evaluate the effectiveness of blockage correction.

For field measurements, we recommend to measure mean velocity $\overline{u}_z$ at the stack center, and apply a correction factor F to approximate bulk velocity u_{bulk}, such that volume flow rate Q is computed by

$$Q = \overline{u}_{\text{bulk}}\, A \approx F\, \overline{u}_z|_{r=0}\, A, \tag{7.1}$$

where A is the cross-sectional area of the narrow exhaust stack. Our results suggest that this method has the smallest possible measurement error and uncertainty. Moreover, this method is less time-consuming than conducting multiple measurements across a sampling plane. Further research is required to validate this method with field measurements, and to determine a suitable value for correction factor F.

Appendix A

Grid Convergence Index (GCI)

The Grid Convergence Index (GCI) is commonly used to estimate discretization uncertainty $\mathbb{u}_{\text{discr}}$. This Appendix gives a step-by-step guide for the classical approach based on research by Roache [78], and the Least Squares version of the GCI pioneered by Eça and Hoekstra. Note that this thesis follows the practice of Eça and Hoekstra in [23], earlier publications (for example [22]) advocate a slightly different way of estimating discretization uncertainty $\mathbb{u}_{\text{discr}}$.

A.1 Classical GCI

Step 1: Define a representative cell, mesh, or grid size h. For example, for a three-dimensional grid

$$h_i = \left(\frac{V}{N}\right)^{1/3}, \tag{A.1}$$

where V is the volume of the grid and N is the total number of cells in the grid.

Step 2: Select a set of three grids, $h_1 < h_2 < h_3$, with a grid refinement factor r so that

$$r_{21} = \frac{h_2}{h_1} > 1.3 \quad \text{and} \quad r_{32} = \frac{h_3}{h_2} > 1.3. \tag{A.2}$$

Determine the values of key variables φ important to the objective of the simulation study.

Step 3: Compute the differences $\epsilon_{32} = \varphi_3 - \varphi_2$ and $\epsilon_{21} = \varphi_2 - \varphi_1$. The observed order of convergence p is calculated by

$$p = \frac{1}{\ln(r_{21})}\left(\ln\left|\frac{\epsilon_{32}}{\epsilon_{21}}\right| + q(p)\right), \tag{A.3a}$$

$$q(p) = \ln\left(\frac{r_{21}^p - s}{r_{32}^p - s}\right), \tag{A.3b}$$

$$s = \operatorname{sgn}\left(\frac{\epsilon_{32}}{\epsilon_{21}}\right). \tag{A.3c}$$

This set of equations is solved using fixed point iteration with the initial guess equal to $q(p) = 0$.

Step 4: Calculate the extrapolated values of the key variables, corresponding to the hypothetical solution for $h = 0$

$$\varphi_0^{21} = \frac{r_{21}^p \varphi_1 - \varphi_2}{r_{21}^p - 1}. \tag{A.4}$$

Step 5: Calculate the relative error

$$e_{\mathrm{a}} = \left| \frac{\varphi_1 - \varphi_2}{\varphi_1} \right|, \tag{A.5}$$

and the estimated extrapolated relative error

$$e_0^{21} = \left| \frac{\varphi_0^{21} - \varphi_1}{\varphi_0^{21}} \right|. \tag{A.6}$$

The fine Grid Convergence Index is defined as

$$\mathrm{GCI}_{\mathrm{fine}}^{21} = \frac{F_s \cdot e_{\mathrm{a}}^{21}}{r_{21}^{p} - 1}, \tag{A.7}$$

where F_s denotes a safety factor. Roache [78] suggests that safety factor $F_s = 1.25$ results in a GCI with a 95 % confidence interval. The GCI corresponds to discretization expanded uncertainty $\mathbb{U}_{\mathrm{discr}}$. The GCI is divided by coverage factor k to obtain discretization standard uncertainty $\mathbb{u}_{\mathrm{discr}}$ by

$$\mathbb{u}_{\mathrm{discr}} = \frac{\mathbb{U}_{\mathrm{discr}}}{k} = \frac{\mathrm{GCI}}{k}. \tag{A.8}$$

Alternatively to the approach by Roache, Celik and Karatekin [12] add an additional absolute sign to (A.3)

$$p = \frac{1}{\ln(r_{21})} \left(\left| \ln \left| \frac{\epsilon_{32}}{\epsilon_{21}} \right| + q(p) \right| \right), \tag{A.9}$$

to avoid negative values of p and ensure extrapolation towards $h = 0$.

A.2 Least Squares version of GCI

This method is based on power series expansions that neglect higher-order terms and assume that key variable φ has at least second-order derivatives. It also assumes that the lowest-order schemes used in the discretization are first or second-order accurate.

Step 1: Define a representative cell, mesh, or grid size h likewise Step 1 of the classical GCI method and determine the key variables φ important to the objective of the simulations study.

Step 2: Solve

$$\delta_{\mathrm{RE}} = \alpha h_i^{p},$$

in the least-squares sense with and without weights to obtain δ_{RE}, p, and the standard deviation σ_{RE} of the two fits.

Step 3: Estimate discretization error δ_{discr}, and standard deviation σ, by following the method applicable to the observed order of grid convergence p:

- If any of fits exhibits $0.5 \leq p \leq 2$, then $\delta_{\mathrm{discr}} = \delta_{\mathrm{RE}}$. If both fits exhibit $0.5 \leq p \leq 2$, the value of δ_{RE} selected corresponds to the fit with the smallest standard deviation.
- If the observed order of grid convergence $p \geq 2$, solve

  $$\delta_1 = \alpha h_i,$$

  and

  $$\delta_2 = \alpha h_i^2,$$

  in the least-squares sense with and without weights, and standard deviations σ of the four fits. Discretization error δ_{discr} is obtained from the fit that exhibits the smallest standard deviation.

- If the observed order of grid convergence $p \geq 2$, solve

$$\delta_1 = \alpha h_i,$$

$$\delta_2 = \alpha h_i^2,$$

and

$$\delta_{12} = \alpha_1 h_i + \alpha_2 h_i^2,$$

in the least-squares sense with and without weights, and standard deviations σ of the six fits. Discretization error δ_{discr} is obtained from the fit that exhibits the smallest standard deviation.

Step 4: Determine a data range parameter

$$\Delta_{\mathrm{discr}} = \frac{(\varphi_i)_{\max} - (\varphi_i)_{\min}}{n-1},$$

to assess the quality of fit used to obtain error estimate δ_{discr}.

Step 5: Determine safety factor F_s:

- If $0.5 \leq p < 2.1$ and $\sigma < \Delta_{\mathrm{discr}}$: $F_s = 1.25$,
- Otherwise: $F_s = 3$.

The safety factor is chosen as $F_s = 1.25$ if the error estimate is deemed reliable, else $F_s = 3$.

Step 6: Obtain the uncertainty from error estimate δ_{discr}, and safety factor F_s using the values of σ and Δ_{discr} to distinguish between "good" and "bad" error estimation:

- For $\sigma < \Delta_{\mathrm{discr}}$ ("good" error estimation):

$$\mathbb{U}_{\mathrm{discr}}(\varphi_i) = F_s|\delta_{\mathrm{discr}}(\varphi_i)| + \sigma + |\varphi_i - \varphi_{\mathrm{fit}}|,$$

- For $\sigma \geq \Delta_{\mathrm{discr}}$ ("bad" error estimation):

$$\mathbb{U}_{\mathrm{discr}}(\varphi_i) = 3\frac{\sigma}{\Delta_{\mathrm{discr}}}\left(|\delta_{\mathrm{discr}}(\varphi_i)| + \sigma + |\varphi_i - \varphi_{\mathrm{fit}}|\right),$$

where φ_{fit} is the value obtained from the fit for the same grid density as the real data point.

Weights

The weighted approach gives more value to the finer than to the coarser grids. For the weighted approach determine

$$w_i = \frac{\frac{1}{h_i}}{\sum_{i=1}^{n}\frac{1}{h_i}}, \tag{A.10}$$

and for the non-weighted approach determine

$$w_i = \frac{1}{n}, \tag{A.11}$$

guaranteeing that $\sum_{i=1}^{n} w_i = 1$.

Single term expansion with unknown order of grid convergence

φ_0 and α are determined from the minimum of the function

$$S_{\mathrm{RE}}(\varphi_0, \alpha, p) = \sqrt{\sum_{i=1}^{n} w_i\left(\varphi_i - (\varphi_0 + \alpha h_i^p)\right)^2}, \tag{A.12}$$

that is obtained from

$$\frac{\partial S_{\mathrm{RE}}}{\partial \varphi_0} = 0, \qquad \frac{\partial S_{\mathrm{RE}}}{\partial \alpha} = 0, \qquad \frac{\partial S_{\mathrm{RE}}}{\partial p} = 0. \tag{A.13}$$

This leads to a system of non-linear equations

$$\varphi_0 = \sum_{i=1}^{n} w_i \varphi_i - \alpha \sum_{i=1}^{n} w_i h_i^p, \tag{A.14a}$$

$$\alpha = \frac{\sum_{i=1}^{n} w_i \varphi_i h_i^p - \left(\sum_{i=1}^{n} w_i \varphi_i\right)\left(\sum_{i=1}^{n} w_i h_i^p\right)}{\sum_{i=1}^{n} w_i h_i^{2p} - \left(\sum_{i=1}^{n} w_i h_i^p\right)\left(\sum_{i=1}^{n} w_i h_i^p\right)}, \tag{A.14b}$$

$$\sum_{i=1}^{n} w_i \varphi_i h_i^p \log(h_i) - \varphi_0 \sum_{i=1}^{n} w_i h_i^p \log(h_i) - \alpha \sum_{i=1}^{n} w_i h_i^{2p} \log(h_i) = 0, \tag{A.14c}$$

that is solved iteratively by a false position method for observed order of grid convergence p. Its standard deviation is given by

$$\sigma_{\mathrm{RE}} = \sqrt{\frac{\sum_{i=1}^{n} n w_i \left(\varphi_i - (\varphi_0 + \alpha h_i^p)\right)^2}{n-3}}. \tag{A.15}$$

Single term expansion with first-order term

φ_0 and α are determined from the minimum of the function

$$S_1(\varphi_0, \alpha) = \sqrt{\sum_{i=1}^{n} w_i \left(\varphi_i - (\varphi_0 + \alpha h_i)\right)^2}, \tag{A.16}$$

that is obtained from

$$\frac{\partial S_1}{\partial \varphi_0} = 0, \qquad \frac{\partial S_1}{\partial \alpha} = 0. \tag{A.17}$$

This leads to a system of linear equations

$$\begin{bmatrix} 1 & \sum_{i=1}^{n} w_i h_i \\ \sum_{i=1}^{n} w_i h_i & \sum_{i=1}^{n} w_i h_i^2 \end{bmatrix} \begin{bmatrix} \varphi_0 \\ \alpha \end{bmatrix} = \begin{bmatrix} \sum_{i=1}^{n} w_i \varphi_i \\ \sum_{i=1}^{n} w_i \varphi_i h_i \end{bmatrix} \tag{A.18}$$

that has standard deviation given by

$$\sigma_1 = \sqrt{\frac{\sum_{i=1}^{n} n w_i \left(\varphi_i - (\varphi_0 + \alpha h_i)\right)}{n-2}}. \tag{A.19}$$

Single term expansion with second-order term

φ_0 and α are determined from the minimum of the function

$$S_2(\varphi_0, \alpha) = \sqrt{\sum_{i=1}^{n} w_i \left(\varphi_i - (\varphi_0 + \alpha h_i^2)\right)^2}, \tag{A.20}$$

that is obtained from

$$\frac{\partial S_2}{\partial \varphi_0} = 0, \qquad \frac{\partial S_2}{\partial \alpha} = 0. \tag{A.21}$$

This leads to a system of linear equations

$$\begin{bmatrix} 1 & \sum_{i=1}^{n} w_i h_i^2 \\ \sum_{i=1}^{n} w_i h_i^2 & \sum_{i=1}^{n} w_i h_i^4 \end{bmatrix} \begin{bmatrix} \varphi_0 \\ \alpha \end{bmatrix} = \begin{bmatrix} \sum_{i=1}^{n} w_i \varphi_i \\ \sum_{i=1}^{n} w_i \varphi_i h_i^2 \end{bmatrix} \tag{A.22}$$

that has standard deviation given by

$$\sigma_2 = \sqrt{\frac{\sum_{i=1}^{n} n w_i \left(\varphi_i - (\varphi_0 + \alpha h_i^2)\right)}{n-2}}. \tag{A.23}$$

Two-term expansion with first and second-order terms

φ_0, α_1, and α_2 are determined from the minimum of the function

$$S_2(\varphi_0, \alpha_1, \alpha_2) = \sqrt{\sum_{i=1}^{n} w_i \left(\varphi_i - (\varphi_0 + \alpha_1 h_i + \alpha_2 h_i^2)\right)^2}, \tag{A.24}$$

that is obtained from

$$\frac{\partial S_{12}}{\partial \varphi_0} = 0, \qquad \frac{\partial S_{12}}{\partial \alpha_1} = 0, \qquad \frac{\partial S_{12}}{\partial \alpha_2} = 0. \tag{A.25}$$

This leads to a system of linear equations

$$\begin{bmatrix} 1 & \sum_{i=1}^{n} w_i h_i & \sum_{i=1}^{n} w_i h_i^2 \\ \sum_{i=1}^{n} w_i h_i & \sum_{i=1}^{n} w_i h_i^2 & \sum_{i=1}^{n} w_i h_i^3 \\ \sum_{i=1}^{n} w_i h_i^2 & \sum_{i=1}^{n} w_i h_i^3 & \sum_{i=1}^{n} w_i h_i^4 \end{bmatrix} \begin{bmatrix} \varphi_0 \\ \alpha_1 \\ \alpha_2 \end{bmatrix} = \begin{bmatrix} \sum_{i=1}^{n} w_i \varphi_i \\ \sum_{i=1}^{n} w_i \varphi_i h_i \\ \sum_{i=1}^{n} w_i \varphi_i h_i^2 \end{bmatrix} \tag{A.26}$$

that has standard deviation given by

$$\sigma_{12} = \sqrt{\frac{\sum_{i=1}^{n} n w_i \left(\varphi_i - (\varphi_0 + \alpha_1 h_i + \varphi_2 h_i^2)\right)}{n-3}}. \tag{A.27}$$

Appendix B

Calibration Certificate

AS0259

CERTIFICATE OF CALIBRATION

ISSUED BY YOUNG CALIBRATION LIMITED
DATE OF ISSUE: 04/04/16
CERTIFICATE NUMBER: C47624

UKAS CALIBRATION
0604

Young Calibration Ltd
5 Cecil Pashley Way
Shoreham Airport
Shoreham-by-Sea
West Sussex, BN43 5FF

+44 (0)1273 455572
enquiries@youngcalibration.co.uk
www.youngcalibration.co.uk

Document : YCF/024
Issue Number : 2.1
Page 1 of 1 Page
Approved Signatory

☐ A. Young ☐ M. Hindle
☐ N. Mardon ☒ C. Millard

Customer: NPL Management Ltd
Customer Address: National Physical Laboratory
Hampton Road
Teddington
Middlesex
TW11 0LW
Purchase Order Number: 439813
Date of Receipt: 22 March 2016
YCL Project Number: YC/34852
Calibration Date: 04 April 2016
Requested Due Date: n/a
Calibration Performed By: M. Parsons
Calibration Procedure: Procedure 53V

Manufacturer & Model: S Type
UUT Description: Pitot Tube
Customer ID Number: n/a
Serial Number: AS 0259
Equipment Condition: Used / As Received / Final
Nominal Calibration Range: 3 - 35 m/s
Calibration Fluid: Atmospheric Air
Calibration Fluid Temperature: 20.2 to 20.8 °C
Calibration Location: YCL Laboratory
Laboratory Temperature: 19.9 to 20.3 °C
Laboratory Barometric Pressure: 1002.6 to 1003.6 mbarA
Laboratory Relative Humidity: 46.5 to 48.8 %RH
Reference Equipment: YC/010/186,187,188

Calibration Method & Notes

The unit under test (UUT) was mounted 140 mm from the end of a wind tunnel with the head aligned perpendicular to the flow direction and was calibrated by comparison to a Laser Doppler Anemometer. The UUT was orientated with the stem marked '+' facing upstream. When stabilised conditions were observed, the measurement conditions were recorded. The air velocity was adjusted to the next condition, and once steady state conditions were achieved, the results were again recorded, this procedure being repeated until the calibration was complete. The UUT results are derived from the average of at least 10 readings.

The "Standard Velocity" and "UUT ΔP" readings are referenced to standard conditions of 1013mbarA and 20°C = 1.205kg/m^3
The pitot tube constant K has been derived from the formula; $V = (2 * \Delta P * K / \rho)\text{^}0.5$
The pitot tube constant γ has been derived from the formula; $V = \gamma (2 * \Delta P / \rho)\text{^}0.5$
Where Velocity (V) is in m/s, Pitot Differential Pressure (ΔP) is in Pa and air density (ρ) is in kg/m^3

Calibration Results

Standard Velocity (m/s)	UUT ΔP (Pa)	UUT ΔP Uncertainty (Pa)	Actual Air Density (kg/m^3)	Pitot γ Constant (-)	Pitot K Constant (-)
3.008	8.35	0.22	1.191	0.808	0.653
8.000	57.26	0.31	1.191	0.821	0.674
15.986	225.2	0.66	1.191	0.827	0.684
15.989	224.7	0.66	1.191	0.828	0.685
15.995	224.6	0.66	1.191	0.828	0.686
15.986	225.1	0.66	1.191	0.827	0.684
15.992	224.8	0.66	1.191	0.828	0.686
16.000	224.9	0.66	1.191	0.828	0.686
24.008	504.1	1.21	1.190	0.830	0.689
35.001	1069.9	2.34	1.187	0.831	0.690

Air Temperature during test : 20.4 - 20.7 °C
Atmospheric Pressure during test : 1003.1 - 1003.1 mbarA
Relative Humidity during test : 46.7 - 47.6 %RH

The uncertainty of the above velocity measurements under laboratory conditions is ± 1.0 % + 0.1 m/s
The uncertainty of the above air density measurements under laboratory conditions is ± 0.17 %
The uncertainty of the above pressure measurements under laboratory conditions is ± 0.2% + 0.2Pa + (UUT ΔP Uncertainty)

The uncertainties reported refer to the measured values only and not to the ability of the instrument to maintain its calibration.

The reported expanded uncertainty is based on a standard uncertainty multiplied by a coverage factor k=2, providing a coverage probability of approximately 95%. The uncertainty evaluation has been carried out in accordance with UKAS requirements. UKAS is one of the signatories to the Multilateral Agreement of the European co-operation for Accreditation (EA) for the mutual recognition of calibration certificates issued by accredited laboratories.

This certificate is issued in accordance with the laboratory accreditation requirements of the United Kingdom Accreditation Service. It provides traceability of measurement to the SI system of units and/or to units of measurement realised at the National Physical Laboratory or other recognised national metrology institutes.

The certificate may not be reproduced other than in full, except with the prior written approval of the issuing laboratory.

Appendix C

S-type Pitot Tube Measurement Results

Wall distance y [mm]	Volume flow rate Q [m^3/s]	Differential pressure Δp [Pa]	Atmospheric pressure P [Pa]	Temperature T [K]	Calibration coefficient K [–]	Uncertainty calibration coefficient $\mathbb{U}(K)$ [–]
4	0.1010	3.88	100531	292.92	0.807	±0.0426
6	0.1010	4.44	100514	292.92	0.807	±0.0424
10	0.1010	5.09	100475	292.91	0.807	±0.0421
16	0.1009	5.88	100445	292.94	0.807	±0.0417
25	0.1009	7.98	100408	292.95	0.808	±0.0408
40	0.1010	9.35	100518	292.94	0.808	±0.0402
100	0.1010	13.70	100527	292.91	0.809	±0.0382
4	0.1556	8.58	100529	292.92	0.808	±0.0405
6	0.1556	9.88	100509	292.91	0.808	±0.0399
10	0.1555	12.16	100472	292.91	0.809	±0.0389
16	0.1554	14.48	100445	292.94	0.810	±0.0379
25	0.1554	18.81	100408	292.95	0.811	±0.0359
40	0.1555	22.66	100515	292.94	0.812	±0.0342
100	0.1525	30.34	100526	292.93	0.814	±0.0308
4	0.2430	20.73	100526	292.96	0.811	±0.0351
6	0.2430	24.88	100502	292.96	0.812	±0.0332
10	0.2430	27.99	100469	292.98	0.813	±0.0319
16	0.2430	36.54	100430	292.98	0.815	±0.0280
25	0.2428	45.05	100407	293.02	0.818	±0.0242
40	0.2429	54.70	100517	293.01	0.820	±0.0200
100	0.2429	71.30	100542	293.00	0.821	±0.0186
4	0.3107	36.31	100526	292.99	0.815	±0.0345
6	0.3106	40.57	100499	292.98	0.815	±0.0322
10	0.3105	47.06	100465	292.99	0.818	±0.0285
16	0.3103	56.98	100420	293.01	0.820	±0.0190
25	0.3102	69.58	100405	293.01	0.821	±0.0186
40	0.3106	86.74	100515	293.00	0.822	±0.0181
100	0.3105	114.99	100536	293.00	0.823	±0.0172

Wall distance y [mm]	Bulk velocity $\overline{u}^*_{\text{bulk}}$ [m/s]	Mean velocity $\overline{u}^*_z$ [m/s]	Non-dimensional velocity $\frac{\overline{u}^*_z}{\overline{u}^*_{\text{bulk}}}$ [−]	Uncertainty non-dimensional velocity $\mathbb{U}\left(\frac{\overline{u}^*_z}{\overline{u}^*_{\text{bulk}}}\right)$ [−]
4	3.14	2.06	0.65	±0.11
6	3.14	2.20	0.70	±0.10
10	3.14	2.36	0.75	±0.10
16	3.14	2.53	0.81	±0.09
25	3.14	2.95	0.94	±0.09
40	3.14	3.20	1.02	±0.09
100	3.14	3.87	1.23	±0.08
4	4.84	3.06	0.63	±0.06
6	4.84	3.29	0.68	±0.05
10	4.84	3.65	0.75	±0.05
16	4.84	3.99	0.82	±0.05
25	4.83	4.55	0.94	±0.05
40	4.84	5.00	1.03	±0.06
100	4.75	5.80	1.22	±0.06
4	7.56	4.78	0.63	±0.04
6	7.56	5.24	0.69	±0.04
10	7.56	5.57	0.74	±0.04
16	7.56	6.38	0.84	±0.04
25	7.55	7.10	0.94	±0.04
40	7.56	7.85	1.04	±0.03
100	7.56	8.97	1.19	±0.04
4	9.67	6.35	0.66	±0.03
6	9.67	6.72	0.70	±0.03
10	9.66	7.26	0.75	±0.03
16	9.65	8.01	0.83	±0.03
25	9.64	8.87	0.92	±0.03
40	9.67	9.90	1.02	±0.03
100	9.67	11.42	1.18	±0.03

Bibliography

[1] AIAA-G-077-1998 (1998). Guide for the verification and validation of Computational Fluid Dynamics simulations.

[2] Anwer, M., So, R., and Lai, Y. (1989). Perturbation by and recovery from bend curvature of a fully developed turbulent pipe flow. *Physics of Fluids A: Fluid Dynamics*, 1:1387–1397.

[3] ASME PTC 19.1-2005 (2005). Test Uncertainty.

[4] ASME V&V 20-2009 (2009). Standard for verification and validation in Computational Fluid Dynamics and heat transfer.

[5] Bailey, S. C. C., Hultmark, M., Monty, J. P., Alfredsson, P. H., Chong, M. S., Duncan, R. D., Fransson, J. H. M., Hutchins, N., Marusic, I., McKeon, B. J., Nagib, H. M., Örlü, R., Segalini, A., Smits, A. J., and Vinuessa, R. (2013). Obtaining accurate mean velocity measurements in high Reynolds number turbulent boundary layers using Pitot tubes. *Journal of Fluid Mechanics*, 715:642–670.

[6] Bauer, C., Feldmann, D., and Wagner, C. (2017). On the convergence and scaling of high-order statistical moments in turbulent pipe flow using Direct Numerical Simulations. *Physics of Fluids*, 10:1043 – 1044.

[7] Berselli, L., Iliescu, T., and Layton, W. (2006). *Mathematics of Large Eddy Simulation of turbulent flows (Scientific Computation)*. Springer.

[8] Boetcher, S. and Sparrow, E. (2007). Limitations of the standard Bernoulli equation method for evaluating pitot/impact tube data. *International Journal of Heat and Mass transfer*, 50:782–788.

[9] Brunekreef, B. and Holgate, S. (2002). Air pollution and health. *Lancet*, 360(9341):1233–1242.

[10] Bryant, R., Sanni, O., Moore, E., Bundy, M., and Johnson, A. (2014). An uncertainty analysis of mean flow velocity measurements used to quantify emissions from stationary sources. *Journal of the Air & Waste Management Association*, 64(6):679–689.

[11] Çengel, Y. A. and Cimbala, J. M. (2014). *Fluid Mechanics - Fundamentals and Applications*. McGraw-Hill Education.

[12] Celik, I. and Karatekin, O. (1997). Numerical experiments on application of Richardson Extrapolation with nonuniform grids. *ASME Journal of Fluids Engineering*, 119(3):584 – 590.

[13] CEN/TC 264/WG 23 (2011). Cen/tc 264/wg 23 n256 rev1: Methods for determination of the velocity and the volumetric flow in stationary source emission - summary report of laboratory and field trials.

[14] Chatzikyriakou, D., Buongiorno, J., Caviezel, D., and Lakehal, D. (2015). DNS and LES of turbulent flow in a closed channel featuring a pattern of hemispherical roughness elements. *International Journal of Heat and Fluid Flow*, 53:29–43.

[15] Coleman, H. W. and Stern, F. (1997). Uncertainties in CFD code validation. *ASME Journal of Fluids Engineering*, 119:175 – 803.

[16] Davidson, L. (2009). Large Eddy Simulations: how to evaluate resolution. *International Journal of Heat and Fluid Flow*, 30:1016–1025.

[17] den Toonder, J. M. J. and Nieuwstadt, F. T. M. (1997). Reynolds number effect in a turbulent pipe flow for low to moderate Re. *Physics of Fluids*, 9(11):3398–3409.

[18] Dimopoulos, C. R., Robinson, R. A., and Coleman, M. D. (2017). Mass emissions and carbon trading: a critical review of available reference methods for industrial stack flow measurement. *Accreditation and Quality Assurance: Journal for Quality, Comparability and Reliability in Chemical Measurement*, 22(3):161–165.

[19] Eça, L. and Hoekstra, M. (2002). An evaluation of verification procedures for CFD applications. In *24th Symposium on Naval Hydrodynamics, Fukuoka, Japan, 8-13 July 2002*.

[20] Eça, L. and Hoekstra, M. (2006). Discretization uncertainty estimation based on a Least Squares version of the Grid Convergence Index. In *2nd Workshop on CFD Uncertainty Analysis, Lisbon, Portugal, 19-20 October 2006*.

[21] Eça, L. and Hoekstra, M. (2009a). Error estimation based on grid refinement studies: a challenge for grid generation. In *Conferência de Métodos Numéricos en Ingineria, Barcelona, Spain, 29 June - 2 July 2009*.

[22] Eça, L. and Hoekstra, M. (2009b). Evaluation of numerical error estimation based on grid refinement studies with the method of the manufactured solutions. *Computers & Fluids*, 38:1580–1591.

[23] Eça, L. and Hoekstra, M. (2014). A procedure for the estimation of the numerical uncertainty of CFD calculations based on grid refinement studies. *Journal of Computational Physics*, 262:104–130.

[24] Eça, L., Hoekstra, M., and Roache, P. J. (2005). Verification of calculations: an overview of the Lisbon workshop . In *AIAA Applied Aerodynamics Conference, Toronto, Canada, 6-9 June 2005*.

[25] Eça, L., Hoekstra, M., and Roache, P. J. (2007). Verification of calculations: an overview of the 2nd Lisbon workshop. In *AIAA Applied Aerodynamics Conference, Miami, USA, 25-28 June 2007*.

[26] Eça, L., Hoekstra, M., Roache, P. J., and Coleman, H. C. (2009). Code verification, solution verification and validation: an overview of the 3rd Lisbon workshop . In *AIAA Applied Aerodynamics Conference, San Antonio, USA, 22-25 June 2009*.

[27] Eggels, J. G. M. (1994). *Direct and Large Eddy Simulation of turbulent flow in a cylindrical pipe geometry*. PhD thesis, TU Delft.

[28] Eggels, J. G. M., Unger, F., Weiss, H. M., Westerweel, J., Adrian, R. J., Friedrich, R., and Nieuwstadt, F. T. M. (1994). Fully developed turbulent pipe flow: a comparison between Direct Numerical Simulation and experiment. *Journal of Fluid Mechanics*, 268:175–209.

[29] ERCOFTAC Special Interest Group on Quality and Trust in Industrial CFD (2000). Best practice guidelines.

[30] European Co-operation for Accreditation (2013). Evaluation of the Uncertainty of Measurement in Calibration (EA-4/02 M:2013).

[31] European Commission (2002). Decision No 1600/2002/EC of the European Parliament and the Council of 22 July 2002 laying down the Sixth Community Environment Action Programme. `http://eur-lex.europa.eu/legal-content/EN/TXT/PDF/?uri=CELEX:32002D1600&from=EN`. Accessed: 28-09-2017.

[32] European Commission (2003). EU Directive 2003/87/EC of the European Parliament and of the Council of 13 October 2003 establishing a scheme for greenhouse gas emission allowance trading within the community and amending Council Directive 96/61/EC. `http://eur-lex.europa.eu/legal-content/EN/TXT/PDF/?uri=CELEX:32003L0087&from=EN`. Accessed: 26-10-2017.

[33] European Commission (2009). EU Directive 2009/125/EC of the European Parliament and of the Council of 21 October 2009 establishing a framework for the setting of ecodesign requirements for energy-related products. `http://eur-lex.europa.eu/legal-content/EN/TXT/PDF/?uri=CELEX:32009L0125&from=EN`. Accessed: 16-10-2017.

[34] European Commission (2010). EU Directive 2010/75/EU of the European Parliament and of the Council of 24 November 2010 on industrial (integrated pollution prevention and control). `http://eur-lex.europa.eu/legal-content/EN/TXT/PDF/?uri=CELEX:32010L0075&from=EN`. Accessed: 06-10-2017.

[35] European Commission (2013a). Communication from the commission to the European Parliament, the Council, the European economic and social committee and the committee of the regions. A Clean Air Programme for Europe. `http://eur-lex.europa.eu/legal-content/EN/TXT/PDF/?uri=CELEX:52013DC0918&from=EN`. Accessed: 28-09-2017.

[36] European Commission (2013b). Impact Assessment: Proposal for a Directive of the European Parliament and of the Council on the limitation of emissions of certain pollutants into the air from Medium Combustion Plants. `http://ec.europa.eu/environment/archives/air/pdf/Impact_assessment_en.pdf`. Accessed: 16-10-2017.

[37] European Commission (2013c). MEMO/13/1169: questions and answers on the EU Clean Air Policy Package. `http://europa.eu/rapid/press-release_MEMO-13-1169_en.htm`. Accessed: 16-10-2017.

[38] European Commission (2015). EU Directive 2015/2193 of the European Parliament and of the Council of 25 November 2015 on the limitation of emissions of certain pollutants into the air from medium combustion plants. `http://eur-lex.europa.eu/legal-content/EN/TXT/PDF/?uri=OJ:L:2015:313:FULL&from=EN`. Accessed: 06-10-2017.

[39] European Committee for Standardization (2007). EN 15259:2007: Air quality - Measurement of stationary source emissions - Requirements for measurement sections and sites and for the measurement objective, plan and report.

[40] European Environment Agency (2017). Exposure of ecosystems to acidification, eutrophication and ozone (Indicator code: CSI005). `https://www.eea.europa.eu/data-and-maps/indicators/exposure-of-ecosystems-to-acidification-14`. Accessed: 26-10-2017.

[41] Fowler, D., Pilegaard, K., Sutton, M., Ambus, P., Raivonen, M., Duyzer, J., Simpson, D., Fagerli, H., Fuzzi, S., Schjoerring, J., Granier, C., Neftel, A., Isaksen, I., Laj, P., Maione, M., Monks, P., Burkhardt, J., Daemmgen, U., Neirynck, J., Personne, E., Wichink-Kruit, R., Butterbach-Bahl, K., Flechard, C., Tuovinen, J., Coyle, M., Gerosa, G., Loubet, B., Altimir, N., Gruenhage, L., Ammann, C., Cieslik, S., Paoletti, E., Mikkelsen, T., Ro-Poulsen, H., Cellier, P., Cape, J., Horváth, L., Loreto, F., Niinemets, U., Palmer, P., Rinne, J., Misztal, P., Nemitz, E., Nilsson, D., Pryor, S., Gallagher, M., Vesala, T., Skiba, U., Brüggemann, N., Zechmeister-Boltenstern, S., Williams, J., O'Dowd, C., Facchini, M., de Leeuw, G., Flossman, A., Chaumerliac, N., and Erisman, J. (2009). Atmospheric composition change: ecosystems-atmosphere interactions. *Atmospheric Environment*, 43(33):5193–5267.

[42] Frederich, O., Wassen, E., Thiele, F., Jensch, M., Brede, M., Hüttmann, F., and Leder, A. (2007). Numerical simulation of the flow around a finite cylinder with ground plate in comparison to experimental measurements. *Notes on Numerical Fluid Mechanics and Multidisciplinary Design*, 96:348–355.

[43] Geršl, J., Knotek, S., Belligoli, Z., and Dwight, R. (2016). Impact of swirl on flow measurement in stacks - CFD modelling. In *17th International Flow Measurement Conference 2016, FLOMEKO 2016*.

[44] Gersten, K. (2005). Fully developed turbulent pipe flow. In Merzkirch, W., editor, *Fluid Mechanics of Flow Metering*, pages 1–22. Springer.

[45] Gnambode, P. S., Orlandi, P., Ould-Rouiss, M., and Nicolas, X. (2015). Large-Eddy Simulation of turbulent pipe flow of power-law fluids. *International Journal of Heat and Fluid Flow*, 54:196–210.

[46] Guala, M., Hommema, S. E., and Adrian, R. J. (2006). Large-scale and very-large-scale motions in turbulent pipe flow. *Journal of Fluid Mechanics*, 554:521–542.

[47] Helton, J. C. and Davis, F. J. (2003). Latin Hypercube sampling and the propagation of uncertainty in analyses of complex systems. *Reliability Engineering and System Safety*, 81(1):23–69.

[48] International Organization for Standardization (1994). ISO 10780:1994: Stationary source emissions - Measurement of velocity and volume flowrate of gas streams in ducts.

[49] International Organization for Standardization (2013). ISO 16911-1:2013: Stationary source emissions - Manual and automatic determination of velocity and volume flow rate in ducts.

[50] International Organization of Standardization (2008). Evaluation of measurement data - Guide to the expression of uncertainty in measurement (JCGM 100:2008).

[51] International Towing Tank Conference. Quality Manual.

[52] Kabacinski, M. and Pospolita, J. (2008). Numerical and experimental research on new cross-sections of averaging pitot tubes. *Flow Measurement and Instrumentation*, 19:17–27.

[53] Kampa, M. and Castanas, E. (2008). Human health effects of air pollution. *Environmental Pollution*, 151(2):362–367.

[54] Kang, W., Trang, N., Shim, J., Jang, H., and Choi, Y. (2015). Experimental and numerical investigation of factors effect on the S-type pitot tube coefficients. *Flow Measurement and Instrumentation*, 44:11–18.

[55] Karniadakis, G. E., Su, C.-H., Xiu, D., Lucor, D., Schwab, C., and Todor, R. A. (2005). *Generalized polynomial chaos solution for differential equations with random inputs.* Eidgenössische Technische Hochschule (ETH) Zürich. Seminar für Angewandte Mathematik.

[56] Kateusz, P. (2015). Estimation of uncertainty of mean velocity of flue gas in a conduit as determined by the traverse method within the gravimetric measurement of particulate concentration. *Flow Measurement and Instrumentation*, 45:318–330.

[57] Kewlani, G., Crawford, J., and Iagnemma, K. (2012). A polynomial chaos approach to the analysis of vehicle dynamics under uncertainty. *Vehicle System Dynamics*, 50(5):749–774.

[58] Kim, J., Moin, P., and Moser, R. (1987). Turbulence statistics in fully developed channel flow at low Reynolds number. *Journal of Fluid Mechanics*, 177:133–166.

[59] Kolář, V. (2007). Vortex identification: New requirements and limitations. *International Journal of Heat and Fluid Flow*, 28(4):638–652.

[60] Kondo, K., Murakami, S., and Mochida, A. (1997). Generation of velocity fluctuations for inflow boundary conditions of LES. *Journal of Wind Engineering and Industrial Aerodynamics*, 67 & 68:51–64.

[61] Kravchenko, A. G., Moin, P., and Moser, R. (1996). Zonal embedded grids for numerical simulations of wall-bounded turbulent flows. *Journal of Computational Physics*, 127:412–423.

[62] Laufer, J. (1954). The structure of turbulence in fully developed pipe flow. Report 1174. Technical report, NACA.

[63] Le Maître, O. P. and Knio, O. M. (2010). *Spectral methods for uncertainty quantification: With applications to computational fluid dynamics.* Springer.

[64] Lee, S., Lele, S., and Moin, P. (1992). Simulation of spatially evolving turbulence and the applicability of Taylor's hypothesis in compressible flow. *Physics of Fluids*, 4:1521–1530.

[65] Leland, B., Hall, J., Joensen, A., and Carroll, J. (1977). Correction of S-type pitot-static tube coefficients when used for isokinetic sampling from stationary sources. *Environmental Science and Technology*, 11(7):694–670.

[66] Livesey, J. L. (1956). The behavior of transverse cylindrical and forward facing total pressure probes in transverse total pressure gradient. *Journal of the Aeronautical Sciences*, 23:949–955.

[67] Lund, T. S. (2003). The use of explicit filters in Large Eddy Simulation. *Computers & Mathematics with Applications*, 46(4):603–616.

[68] MacMillan, F. A. (1957). Experiments on pitot tubes in shear flow. Technical Report 3028, Ministry of Supply. Aeronautical Research Council.

[69] McKeon, B. J. (2007). Pressure-based velocity measurements. In *Springer Handbook of Experimental Fluid Mechanics*, pages 216–229. Springer.

[70] McKeon, B. J., Li, J., Jiang, W., Morrison, J. F., and Smits, A. J. (2004). Further observations on the mean velocity distribution in fully developed pipe flow. *Journal of Fluid Mechanics*, 501:135–147.

[71] McKeon, B. J., Li, J., Jiang, W., and Smits, A. J. (2003). Pitot probe corrections in fully developed turbulent pipe flow. *Measurement Science and Technology*, 14:1449–1458.

[72] Moukalled, F., Mangani, L., and Darwish, M. (2016). *The finite volume method in Computational Fluid Dynamics: An advanced introduction with OpenFOAM and Matlab*. Springer.

[73] Nicoud, F. and Ducros, F. (1999). Subgrid-scale stress modelling based on the square of the velocity gradient tensor. *Flow, Turbulence and Combustion*, 62(3):183–200.

[74] Nikuradse, J. (1932). *Gesetzm assigkeiten det turbulenten Str omung in glatten Rohren*. PhD thesis, Kaiser-Wilhelm Institute.

[75] Norfleet, S. K., Muzio, L. J., and Martz, T. D. (1998). An examination of bias in Method 2 Measurements under controlled non-axial flow conditions. `http://www.rmb-consulting.com/sknhrpap/hrpaper.htm`. Accessed: 11-06-2018.

[76] Piomelli, U. and Chasnov, J. R. (1996). Large Eddy Simulation: Theory and applications. In *Turbulence and Transition Modelling*, volume 2, pages 269–336. Springer.

[77] Pope, S. B. (2000). *Turbulent Flows*. Cambridge University Press.

[78] Roache, P. (1998). *Verification and validation in computational science and engineering*. Hermosa Publishers.

[79] Sagaut, P. (2006). *Large Eddy Simulation for incompressible flows*. Springer, third edition.

[80] Schmelter, S., Fiebach, A., Model, R., and Bär, M. (2015). Numerical prediction of the influence of uncertain inflow conditions in pipes by polynomial chaos. *International Journal of Computational Fluid Dynamics*, 29(6-8):411–422.

[81] Sensing Precision: Air Measurement Specialists. `https://sensing-precision.com/product/l-type-pitot-tubes/`. Accessed: 26-06-2018.

[82] Shinder, I. I., Khromchenko, V. B., and Moldover, M. R. (2015). NIST's new 3D airspeed calibration rig addresses turbulent flow measurement challenges.

[83] Smagorinsky, J. S. (1963). General circulation experiments with the primitive equations. *Monthly Weather Review*, 91:99–164.

[84] Smirnov, S., Shi, S., and Celik, I. (2001). Random flow generation technique for Large Eddy Simulations and particle-dynamics modelling. *Journal of Fluids Engineering*, 123:359–371.

[85] Smith, R. (2013). *Uncertainty Quantification: Theory, implementation, and applications.* Computational Science and Engineering. SIAM.

[86] Sreenivasan, K. R. and Sahay, A. (1997). The persistence of viscous effects in the overlap region, and the mean velocity in turbulent pipe and channel flows. In *Self-Sustaining Mechanisms of Wall Turbulence.* Computational Mechanics Publications.

[87] Stern, F., Wilson, R. V., Coleman, H., and Patterson, E. (2001). Comprehensive approach to verification and validation of CFD simulations - part 1: Methodology and procedures. *Journal of Fluids Engineering*, 123(4):793–802.

[88] Tabor, G. R. and Baba-Ahmadi, M. H. (2010). Inlet conditions for large eddy simulation: A review. *Computers & Fluids*, 39:553–567.

[89] Tavoularis, S. and Szymczak, M. (1989). Displacement effects of square-ended pitot tubes in shear flows. *Experiments in Fluids*, 7:33–37.

[90] Tørseth, K., Aas, W., Breivik, K., Fjæraa, A. M., Fiebig, M., Hjellbrekke, A. G., Lund Myhre, C., Solberg, S., and Yttri, K. E. (2012). Introduction to the European Monitoring and Evaluation Programme (EMEP) and observed atmospheric composition change during 1972-2009. *Atmospheric Chemistry and Physics*, 12:5447–5481.

[91] Trang, N. D., Kang, W., Shim, J. S., Park, S. M., and Choi, Y. M. (2012). Experimental study on the factors effect on the S type pitot tube coefficient. In *XX IMEKO World Congress, Busan, Korea, 9-14 September 2012.*

[92] Turnock, S. T., Spracklen, D. V., Carslaw, K. S., Mann, G. W., Woodhouse, M. T., Forster, P. M., Haywood, J., Johnson, C. E., Dalvi, M., Bellouin, N., and Sanchez-Lorenzo, A. (2015). Modelled and observed changes in aerosols and surface solar radiation over Europe between 1960 and 2009. *Atmospheric Chemistry and Physics*, 15:9477–9500.

[93] US EPA (1999a). EPA flow reference method testing and analysis: findings report. EPA/430-R-99-009a.

[94] US EPA (1999b). Method 2H - determination of stack gas velocity taking into account velocity decay near the stack wall.

[95] van Hove, A., Skov, L. N., and Hinz, D. F. (2018). Reproducibility of experiments with swirling flow: Numerical prediction with polynomial chaos. *Journal of Verification, Validation and Uncertainty Quantification*, 3(1):011002–1 – 011002–12.

[96] Vinod, V., Chandran, T., Padmakumar, G., and Rajan, K. (2012). Calibration of an averaging pitot tube by numerical simulation. *Flow Measurement and Instrumentation*, 24:26–28.

[97] Viola, I. M., Bot, P., and Riotte, M. (2013). On the uncertainty of CFD in sail aerodynamics. *International Journal for Numerical Methods in Fluids*, 72:1146–1164.

[98] Wang, S. S. Y., Roache, P. J., Schmalz, R. A., and Jia, Y. (2009). Verification and validation of 3D free-surface flow models.

[99] Wecel, D., Chmielniak, T., and Kotowicz, J. (2008). Experimental and numerical investigations of the averaging pitot tube and analysis of installation effects on the flow coefficient. *Flow Measurement and Instrumentation*, 19:301–306.

[100] Weissenbrunner, A., Fiebach, A., Schmelter, S., Bär, M., Thamsen, P. U., and Lederer, T. (2016). Simulation-based determination of systematic errors of flow meters due to uncertain inflow conditions. *Flow Measurement and Instrumentation*, 52(3-4):25–39.

[101] Westerweel, J., Boersma, B. B., and Nieuwstadt, F. T. M. (2016). *Turbulence: Introduction to theory and applications of turbulent flow.* Springer.

[102] Williams, J. and DeJarnette, F. (1977). A study on the accuracy of type-S pitot tube. Technical report, EPA.

[103] Wilson, R. V., Stern, F., Coleman, H. W., and Paterson, E. G. (2001). Comprehensive approach to verification and validation of CFD simulations - Part 2: Application of RANS simulation of a cargo/container Ship . *Journal of Fluids Engineering*, 123:803 – 810.

[104] Wu, X. and Moin, P. (2008). A Direct Numerical Simulation study on the mean velocity characteristics in turbulent pipe flow. *Journal of Fluid Mechanics*, 608:81–112.

[105] Xiu, D. and Karniadakis, G. E. (2002). The Wiener-Askey polynomial chaos for stochastic differential equations. *SIAM Journal on Scientific Computing*, 24(2):619–644.

[106] Xu, X., Lee, J., and Pletcher, R. (2005). A compressible finite volume formulation for Large Eddy Simulation of turbulent pipe flows at low Mach number in Cartesian coordinates. *Journal of Computational Physics*, 203(1):22–48.